Sarah Bergin

Pathlength calibration of integrating sphere based gas cells

Centre for Engineering Photonics

School of Aerospace, Transport and Manufacturing

PhD thesis

2012-2015

Supervisors: Dr. Jane Hodgkinson, Prof. Ralph Tatam

Submitted: 2016

This thesis is submitted in partial fulfilment of the requirements for the degree of Doctor of Philosophy

Abstract

Integrating sphere based multipass cells, unlike typical multipass cells, have an optically rough reflective surface, which produces multiple diffuse reflections of varying lengths. This has significant advantages, including negating scattering effects in turbid samples, removing periodicity of waves (often the cause of etalon fringes), and simple cell alignment. However, the achievable pathlength is heavily dependent on the sphere wall reflectivity. This presents a challenge for ongoing in-situ measurements as potential sphere wall contamination will cause a reduction in mean reflectivity and thus a deviation from the calibrated pathlength.

With this in mind, two techniques for pathlength calibration of an integrating sphere were investigated. In both techniques contamination was simulated by creating low reflectivity tabs e.g. ≈5x7mm, that could be introduced into the sphere (and removed) in a repeatable manner.

For the first technique, a four beam configuration, adapted from a turbidity method used in the water industry, was created using a 5cm diameter sphere with an effective pathlength of 1m. Detection of methane gas was carried out at 1650nm. A mathematical model was derived that corrected for pathlength change due to sphere wall contamination in situ, thus enabling gas measurements to continue to be made. For example, for a concentration of 1500ppm of methane where 1.2% of the sphere wall was contaminated with a low reflectivity material, the absorption measurement error was reduced from 41% to 2% when the model was used. However some scenarios introduced errors into the correction, including contamination of the cell windows which introduced errors of, for example, up to 70% if the particulate contamination size was on the order of millimetres.

The second technique used high frequency intensity modulation with phase detection to achieve pathlength calibration. Two types of modulation were tested i.e. sinusoidal modulation and pulsed modulation. The technique was implemented using an integrated circuit board which allowed for generation of modulation signals up to 150MHz with synchronous signal processing. Pathlength calibration was achieved by comparison of

the phase shift for a known length with the measured phase shift for the integrating sphere with unknown pathlength over a range of frequencies. The results for both modulation schemes showed that, over the range of frequencies detected, 3-48MHz, the resultant phase shift varied as an arctangent function for an integrating sphere. This differed from traditional single passes where frequency and phase have a linear relationship.

Acknowledgements

Thanks to Ralph for taking a chance on me, even after I spelled his name wrong in my first email! He was very helpful as both a supervisor and an educator, offering constructive recommendations for my experimental work but also striving to ensure that I learned the fundamentals along the way.

Thanks to Jane for being a brilliant first supervisor. She was always there to offer advice and encouragement, especially at serious head scratching stages, and to share the enthusiasm when things were working, even when it came in the form of late night "Eureka!" emails.

Thanks to Steve Staines for his ongoing help with my project build, for teaching me many things from how to solder wiring for my laser to how to care for bees! The numerous and varied chats were a very enjoyable part of my time at Cranfield.

Thanks to Thomas Kissinger for giving so much of his time to help me, especially when he was still finishing his own PhD. His depth of knowledge and never-ending supply of ideas are an inspiration…I'm hoping that learning by osmosis is possible!

Thanks to all of the members of the Engineering Photonics department, who were always helpful, friendly and created a lovely working environment.

Thanks to my brilliant friends in Ireland and the UK, in particular Lisa, who provided laughter and delicious food when I came to visit. Thanks to Phil for his support and for putting up with my PhD rants and ramblings.

And finally thanks to my family who love and encourage me always and, I decided, were the only people allowed to ask me how my thesis was going! They've supported me at all stages, including times I worked when at home instead of spending time with them, flying over to see me, and the many phone calls.

This thesis is dedicated to my grandmother Julia, a woman who has been educating me since my earliest days and who I continue to learn from no matter how old I get!

Contents

List of Figures

List of Tables

Notation

α	Absorption coefficient (m^{-1})
A	Absorbance (unitless) = $\log_{10}(\varphi_i/\varphi_e)$
A’	Apparent absorbance (unitless)
A_d	Area of detector (m^2)
A_e	Area of exit port (m^2)
A_i	Area of input port (m^2)
A_F	Area of fibre optic output (m^2)
A_S	Area of sphere (m^2)
Abs_w	Proportionality constant relates to the fraction of absorptance of radiation by the wall and the fraction of radiation flux at each given unit area of the sphere wall
B_S	Radiance of sphere $W \cdot sr^{-1} \cdot m^{-2}$
c	Speed of light (m/s)
C	Concentration (ppm for example)
C_1	Proportionality constant (between radiance of inner and outer sphere)
D_S	Diameter of sphere (m)
ε	Specific absorptivity (ppm/m)
ΔE	Uncertainty in energy (J)
f	Port fraction
F	Fringe spacing (m^{-1})

F	Frequency (Hz)
Gα	Splitting fraction (i.e. due to particulates)
h	Plancks constant (J·s)
ħ	Reduced Planck's constant (h/2π) (J·s)
h(t)	Impulse response
H_0	Irradiance of empty sphere
H_α	Irradiance with absorbing species present
H_w	Irradiance within the integrating sphere wall
I	Radiant intensity $W \cdot sr^{-1}$
I_c	Current (A)
k_B	Boltzmann's constant
K	Detector sensitivity (V)
L	Pathlength (m)
L_{eff}	Effective pathlength (m)
L_{sp}	Average distance for a single pass (m)
M	Multiplier
n	Refractive index
ν	Velocity of atom (m/s)
N(t)	Number of photons overall
$dN_A(t)$	Number of photons absorbed by wall during time interval t
$dN_C(t)$	Number of photon collisions during a time interval t
ω_0	Angular frequency for an atom at rest (rad/s)

ω_c	Carrier frequency (Hz)
$\Delta\omega$	Bandwidth (Hz)
Ω	Solid angle (sr)
Ω	Doppler shifted frequency (rad/s)
Ω_0	Frequency of detection (Hz)
$\Delta\varphi$	Phase difference (rad)
Φ_d	Flux incident on detector (W)
$\Phi_e(0)$	Radiant flux transmitted through the cell (W) in the absence of an absorbing species
$\Phi_e(\alpha)$	Radiant flux transmitted through the cell (W) in the presence of an absorbing species
$\Phi_e(m)$	Radiant flux in presence of thin film matrix (W)
Φ_i	Radiant flux incident on cell (W)
$\Delta\Phi$	$\varphi_e(0)$-$\varphi_e(\alpha)$ (W)
q	Elementary charge of an electron (C)
ρ	Reflectance
P_S	Probability that a photon will not be absorbed
r	Radius of the sphere (m)
R	Resistance (Ω)
σ_i	Current (A)
τ	Decay constant
t	Time (s)
Δt	Uncertainty in time (s)

T	Absolute temperature (K)
T	Transmittance factor
T_{AB}	Ratio of irradiance of two non scattering absorbers
V	Voltage (V)
V_c	Volume of cavity (m^3)

1

Introduction

"Human influence on the climate system is clear, and recent anthropogenic emissions of greenhouse gases are the highest in history. Recent climate changes have had widespread impacts on human and natural systems" – IPCC 2014[1].

1.1 The challenge for gas sensing

The demand for gas sensors in the global gas market is being driven primarily by more stringent government regulations regarding safety in the workplace as well as emission control[2], [3]. Some of the specific areas where the demand for gas sensors has increased include the industrial, petrochemical and automotive sectors. Typical gases of concern in these sectors are listed in Table 1.1.

Some of the safety risks that regulations aim to mitigate include workers exposure to toxic gases, or potential explosive situations due to gas leaks. Regarding environmental aspects, the Intergovernmental Panel for Climate Change (IPCC) has reported that the total anthropogenic greenhouse gas (GHG) emissions were the highest in human history from 2000 to 2010 (49 (±4.5) $GtCO_2eq/yr$ in 2010 i.e. CO_2 equivalent in gigatonnes per year)[1]. Direct effects such as the growing industrialization in Asia, as well as indirect knock on effects such as wetland emissions in the Arctic and Tropics are just some of the factors that have contributed to this increase, according to the National Oceanic and Atmospheric Administration (NOAA)[4], [5].

Table 1.1: Typical gases of concern in various industries, adapted from[6]

Industry	Application	Typical gases
Gas supply	Leak detection (field)	CH_4
	Processing/distribution	CH_4, H_2S
Waste/wastewater	Safety	CH_4, other combustibles
	Health	CO, O_2 deficiency, Cl_2
Petrochemical	Environment	NO_x, SO_2, CO, CO_2, NH_3
	Health	CO, CO_2, HF, VOCs, HCN
	Process monitoring & control	O_2, H_2, NH_3, H_2S
Automotive	Emission control	NO_x, N_2O, CH_4,

The consequences of these increased emissions e.g. more extreme weather fluctuations and a record low sea-ice extent[7], are causing concerns globally amongst policymakers that irreversible damage to our ecosystems may result if these trends continue. This has prompted efforts to achieve global agreement on mitigation strategies, such as the recent United Nations Climate Change Conference held in Paris in December 2015. A major mandate for nations was to reduce carbon emissions so that global warming over this century would be maintained at less than 2 degrees Celsius (°C) compared to pre-industrial levels[8].

Figure 1.1: In Cumbria, many people were evacuated from their homes after flooding caused by Storm Desmond (taken from BBC news, Dec 2015)[9]***. This is an example of the kinds of consequences that result from more extreme weather fluctuations.***

With these environmental and safety considerations in mind, the types of gas measurements required by the end user can range from the long term monitoring of gas build up to short term localised emissions. Often these measurements require a gas sensor that can operate in challenging environments, such as making atmospheric measurements of methane while on board an aircraft[10] or measuring the toxic build-up of hydrogen sulphide on petrochemical works[11]. It is these kinds of applications that this body of research is targeting, e.g. challenging environments where mechanical vibrations, temperature fluctuations or contamination have the potential to degrade sensor performance. To test sensor performance, methane (CH_4) was chosen as the target gas for this research.

Methane, a hydrocarbon, occurs naturally in air (with a concentration of 1.7-1.9 parts per million (ppm))[12]. It is also the primary component of natural gas, an energy source that has been championed by policymakers as an interim substitute for higher carbon fuels[13], [14], as demonstrated by the extensive natural gas pipeline network in the US (Figure 1.2). However it is a powerful greenhouse gas, and although present in much lower concentrations than carbon dioxide, has a global warming potential (GWP) that is 23 times higher over a 100 year time period[15]. The effects of methane on climate and atmospheric chemistry as well as its explosive nature at concentrations between 5%-15%[16] make it an important gas of interest whether in terms of the environmental impact or for safety.

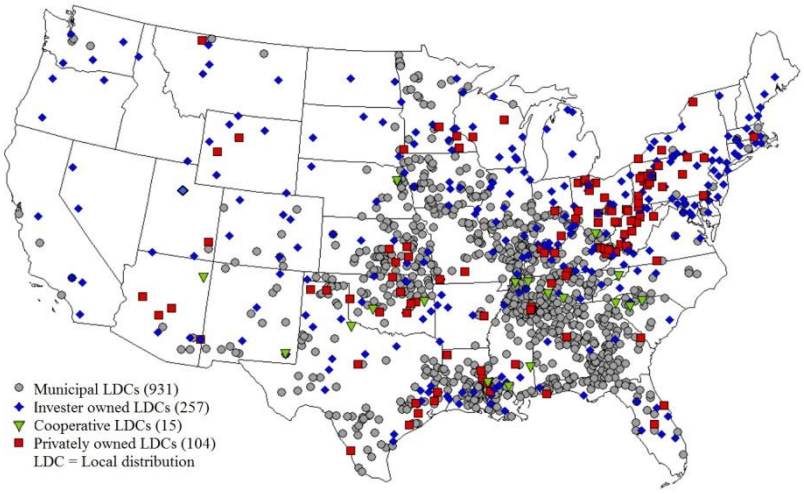

Figure 1.2: In the US natural gas pipeline network it is estimated that there is a system wide loss of 80 billion cubic feet of methane annually[17]***, equivalent to a financial loss of approximately $207 million***[18]***, taken from*** [19]

In the context of the applications mentioned above, e.g. for longer term baseline gas monitoring or short term leak detection, ideally the sensor:

- Is highly selective to the target gas i.e. does not suffer cross sensitivity to other gases.
- Provides accurate and repeatable measurement capability with a sufficient dynamic range e.g. from ppm to % lower explosive limit (LEL) depending on the intended application.
- Is capable of responding to the presence of the target gas within a timely fashion, e.g. provides sufficient warning to workers in the vicinity.
- Can maintain performance in its environment, i.e. is immune to (or can correct for) drift.
- Does not pose a risk by its presence (such as containing a potentially explosive element).
- Can be portable or fixed, is easy to operate and cost effective for the end-user.

There are many gas detection techniques that meet some of these criteria and a selection of these are discussed in more detail in Chapter 2. In general, non optical sensors such as flame ionisation detectors (FID) and electrochemical (EC) sensors dominate the gas market due to their low cost, however they can suffer from issues such as cross response

to other gases (FIDs cross respond to carbon containing gases) or temperature sensitivity (temperature changes can shorten the finite lifetime of EC sensors). Optical gas sensors, in particular those employing spectroscopic techniques, are an ideal choice where high selectivity and specificity is required[20], and their sensitivity is well suited to trace gas measurements. The approach of choice for this project is tunable diode laser spectroscopy (TDLS), a highly selective optical absorption method, suitable for measuring trace atmospheric components with a detection capability of sub ppm concentrations. This generic technique is in widespread use, especially for environmental measurements.

1.2 Gas sensors based on tunable diode laser spectroscopy

A number of gas sensing technologies[21], [22] based on tunable diode laser spectroscopy (TDLS), some of which are discussed in Chapter 2, have been successfully deployed in challenging environments such as on in-flight systems, facilitating high quality measurements of atmospheric gases such as methane and carbon dioxide. The typical TDLS setup, as seen in Figure 1.3, employs a tunable diode laser, with the output tuned to scan over the wavelength region where the gas of interest absorbs radiation (usually in the IR region) at very high resolution. The principle of operation is discussed in more detail in section 2.3.2.

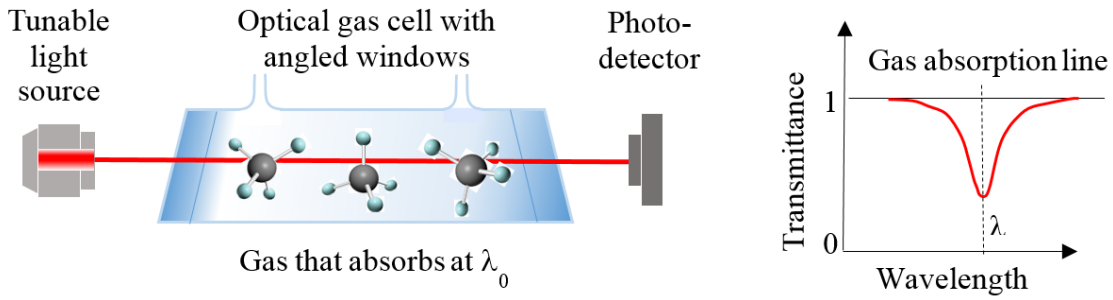

Figure 1.3: Typical TDLS setup-laser output is tuned to scan across the gas absorption line of interest

The high resolution is achievable because of the narrow linewidth of the laser used (typically tens of MHz), which is up to three orders of magnitude narrower than the gas absorption linewidth (typically several GHz at atmospheric pressure)[23]. To achieve high signal-to-noise ratios, TDLS systems often employ multipass optical cells, where

the beam is folded a number of times between reflective surfaces thus increasing the interaction of light with the sample of interest, i.e. giving a long pathlength, in a relatively small volume. However the optical alignment of these cells is complex with tight tolerances for misalignment. Additionally, due to the configuration of these reflective surfaces, there is the potential for optical interference fringes to be created that can obscure the desired signal. With these limitations in mind, this body of research investigated using an integrating sphere as a multipass gas cell, with the aim of providing a more robust alternative for use in challenging environments such as those described in the previous section.

1.3 Integrating spheres for gas sensing

Though originally used to measure the total emission flux of light sources, in the last 40 years the integrating sphere has been gaining attention in gas sensing research. A review of prior work, which is detailed in Chapter 4, has shown that integrating cavities as multipass cells can be a powerful tool for absorption measurements. An integrating sphere consists of an optically rough inner surface providing uniformly diffuse reflections, where multiple beams make multiple passes throughout the cavity wall, the result being an effectively long optical pathlength. The varying lengths and orientations of these beam passes, means that, unlike in typical multipass cells[24], the periodicity, and thus potential optical interference fringes between reflective surfaces is not present within the sphere.

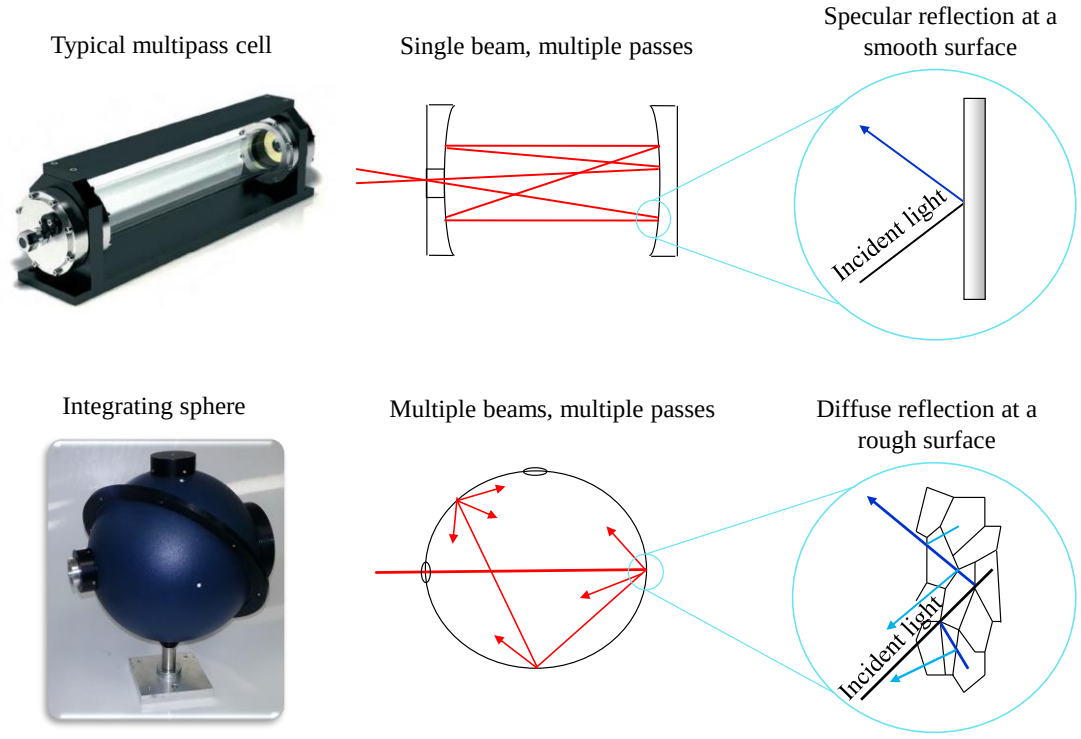

Figure 1.4: Typical multipass cell vs. integrating sphere; multipass cells reflect a single beam multiple times resulting in a specular output. Integrating spheres reflect multiple beams simultaneously resulting in diffusive reflections. (Multipass cell photograph from [25]**.**

The diffusive nature of the material eases alignment tolerances, as variations in the angle of incident light will not affect the observed radiance by the detector. Furthermore due to this scattering property of the cavity wall material, any further light scattering caused by particulates in the sample will have a minimal effect on the absorption measurement[26].

However the achievable effective optical pathlength is heavily dependent on the cavity wall reflectivity. This presents a challenge for ongoing in-situ measurements as potential cavity wall contamination will cause a reduction in mean reflectivity and thus deviation from the calibrated pathlength. This deviation, in the short term, results in erroneous gas absorption measurements, and in the long term, if the presence of contamination is not realised, can reduce the system's sensitivity to an unacceptable level. The focus of this research was to investigate the performance of the integrating sphere as a gas cell when these deviations occurred. The ultimate aim was to provide a method for maintaining a calibrated pathlength, so that the integrating sphere could

continue to provide accurate gas absorption measurements even in the presence of contamination. Overcoming this would move the integrating sphere based gas cell one step closer to becoming part of a gas sensor for field analysis and would provide confidence to users even in situations where contamination is minimised.

1.4 Thesis aims and objectives

The main aim of this research was to demonstrate the feasibility of an integrating sphere as a rugged tool for optical gas detection when in challenging environments, e.g. vibrations, gas samples with particulates.

It was intended to accomplish this through the following research objectives:

1, Devise a method for pathlength calibration of the sphere for use both at initial factory calibration but also when in-situ and in the event of contamination of the sphere.

2. Test the calibration in the presence of quantified known levels of contamination to understand how contamination affected the diffusion properties of the sphere as well as the achievable detection limit.

3. Perform gas measurements in the presence of both known concentrations of gas and contamination to test the pathlength calibration and also the efficacy of the setup for gas detection

1.5 Thesis novelty

The following points summarise the parts of this research that were considered to be novel.

- Though some preliminary academic based research has been carried out to demonstrate how an integrating sphere functions as a multipass cell, there has been no investigation into how the sphere would function if its performance worsened, e.g. if the sphere wall became contaminated. The work carried out in this thesis investigated different techniques for calibrating and maintaining the sphere pathlength in the event of contamination degrading the performance. This included creating a repeatable methodology for testing the effect of contamination.

- A new mathematical derivation combining the typical gas laws with integrating sphere relations was produced, which was able to correct for pathlength changes due to sphere wall contamination, based on a so-called four beam analysis.
- This setup, combined with the mathematical derivation, forms the basis of a patent application. The configuration was implemented and tested using the developed methodology.
- Two systems, based on phase detection methods in the time domain were implemented using an integrated circuit board. To the authors knowledge the use of this type of signal generation and processing has not been previously attempted for an integrating sphere based gas sensor.
- This combination of an easy-to-align integrating sphere gas cell with an integrated circuits approach allowed for implementation of a sensitive optical technique using lower cost components and a compact setup. At the time of writing, patents based on these systems are being considered.
- The phase detection approaches have contributed further understanding of integrating sphere systems in terms of how the phase differs with varying modulation frequencies, which hasn't been previously reported.

1.6 Thesis chapter outline

This first chapter, Chapter 1, has provided a background to this project; how integrating sphere based gas cells could benefit the gas sensing industry and in what way they are currently limited. The main aim of this research was to provide methods for pathlength calibration of an integrating sphere for gas detection. To focus attention, the chapter outlines the aspects of this research that were considered to be novel. Chapter 2 details some of the current gas detection technologies, both optical and non-optical, that are available commercially, emphasising the advantages and limitations of each. This aims to provide the industrial context in which an integrating sphere based sensor would sit. Chapter 3 introduces some of the considerations when designing an optical sensing instrument. This includes sensitivity limiting factors such as noise as well as sensitivity enhancing factors such as modulation techniques. Chapter 4 describes the theory of the integrating sphere, both in its original capacity as a tool for measuring lumen output and its adaptation as a gas cell. In particular, the chapter provides some insight into how the

properties of an integrating sphere are affected by introduction of gas or contaminants to the cavity.

The next two chapters form the experimental sections of this body of research. Two different approaches to pathlength calibration were taken, which were then applied to detection of methane gas. Chapter 5 details the first approach, an intensity measurement based technique relating changes in cavity wall reflectivity, e.g. due to contamination, to the original calibrated system, and adjusting the pathlength accordingly. This facilitates accurate gas absorption measurement even in the presence of contamination. The second approach, as detailed in Chapter 6, introduces a phase detection technique, where high frequency intensity modulation is employed allowing for a pathlength to be calculated from temporal phase shift measurements. The final chapter, Chapter 7, concludes by reviewing the extent to which the objectives set our were achieved, then the benefits and limitations of these two experimental approaches, as well as the outlook for taking these techniques forward.

2

Gas detection technologies

"The global gas detection equipment market, valued at US$ 2.2 billion in 2013, is expected to see a mean annual growth rate of 5.0% during the forecast period from 2014 to 2022. Gas detection equipment are majorly used as a part of safety system for detecting leakage and presence of gases in a given area" – Transparency market research[27]

In the gas detection industry there is no one technology that can achieve all of the criteria mentioned in Section 1.1. Sensors that give high selectivity, e.g. no cross response to other gases, and sensitivity, e.g. detection limits of low ppb or ppt, often come at a cost (for example due to the use of specialist components such as mid-IR lasers, highly reflective mirrors) that can be prohibitive for the end user. This chapter introduces some optical and non-optical technologies that are in current use, including those that are being deployed in the more challenging environments such as airborne platforms and petrochemical works. The advantages and limitations of each technology are discussed. Some additional information regarding the principles of optical absorption spectroscopy is included in this Chapter as these are the governing principles for this body of research.

2.1 Non-optical gas sensors

Non-optical detectors still dominate the market due to their, in general, ease of use and cost effectiveness[27]. This section discusses electrochemical, metal oxide and flame ionisation detection as these are employed across a wide range of industries and for methane detection.

2.1.1 Electrochemical sensors (EC)

Electrochemical sensors are commonly deployed for detection of toxic gases as they display excellent linearity and sensitivity to the gas down to part per million (ppm) levels, have very low power consumption and can be manufactured at low cost. The

typical configuration[28], as seen in Figure 2.1, includes a working (or sensing) electrode, a counter electrode and often a reference electrode (to keep the potential of the sensing electrode constant) all of which are in contact with a conducting electrolyte.

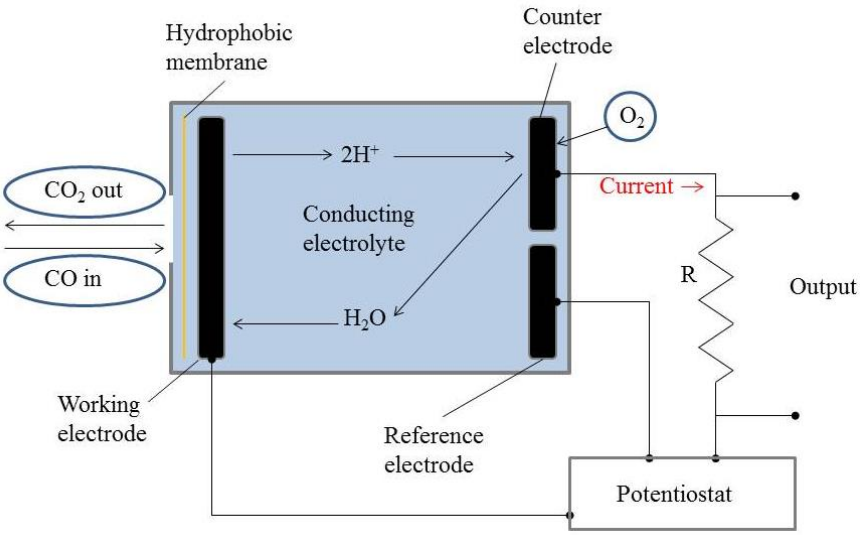

Figure 2.1: Example of a typical carbon monoxide (CO) electrochemical cell. The oxidation or reduction of the target species at the working electrode generates a current that is proportional to the concentration of the species. Adapted from [29]

The sample of interest is passed through a gas membrane to the sensing electrode, where it will either be reduced or oxidised, creating charged species. As these species pass from the sensing electrode to the counter electrode, a current is generated which is proportional to the concentration of gas present. Advantages of this technique include the ability to measure over a large concentration range, which is achieved by controlling the gas diffusion through the gas membrane. However, though sensitive to the target gas, these sensors can also exhibit cross-sensitivity to other gases. For example carbon monoxide sensors can suffer interference from hydrogen[30]. Furthermore EC sensors have a very limited temperature range over which they operate and in general have a short shelf life (≈6 months) and so may not be suitable for applications where long-term monitoring is required. A typical detection limit for methane using this technology tends to be in the 1000s of ppm[31] however this technology is not well suited for methane. Parts per billion (ppb) detection limits have been achieved for other gases, such as NOx[32].

2.1.2 Flame ionisation detector (FID)

Flame ionisation detection is a useful technique for measuring organic species, and has been employed to monitor fugitive emissions from hazardous waste [33], as well as being used in the automotive industry to measure emissions from engines[34]. The system works by applying an electric potential across a hydrogen-air flame jet and collector plate[35]. Combustion of the gas sample occurs in the flame jet causing ejection of electrons which are collected under the influence of the electrical field, as seen in Figure 2.2.

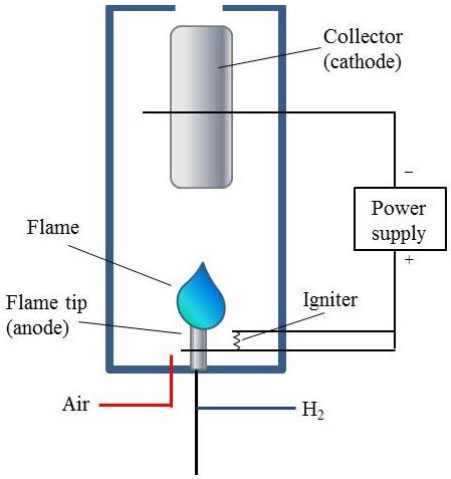

Figure 2.2: Typical setup of flame ionisation detector. The gas sample is combusted in a hydrogen flame causing ejection of electrons which are collected at a collector plate. This generates a current that is proportional to the concentration of ionised sample. Taken from [36]

The resultant current is proportional to the concentration of ionised sample. This technique is more suitable for hydrocarbons, tending to be more sensitive to long carbon chains with detector response decreasing in the presence of heteroatoms, such as oxygenated species. Some of the advantages of FIDs include the ability to measure over a large dynamic range (1-50,000ppm[37]), low maintenance once it is set up and robustness in the field; for example the FID is almost unaffected by ambient levels of CO, CO_2 or water vapour. However the presence of a hydrogen flame makes it an unsuitable technique for applications such as on-board aircraft or in flammable hazard zones in petrochemical works where equipment must be intrinsically safe. Furthermore as it is a destructive technique it is not ideal for applications where further analysis of the sample may be required.

2.1.3 Metal oxide semiconductor (MOS)

Metal oxide semiconductor sensors are low cost, rugged and can be configured to detect a wide range of gases, making them one of the most popular detection technologies worldwide. MOS sensors contain a metal oxide-based surface which is sensitive to specific gases (dependent on what metal oxide is used) when heated to high temperatures, usually 200–400°C. When exposed to the target gas, the electrical resistance across the surface changes as a consequence of adsorption/desorption of oxygen.

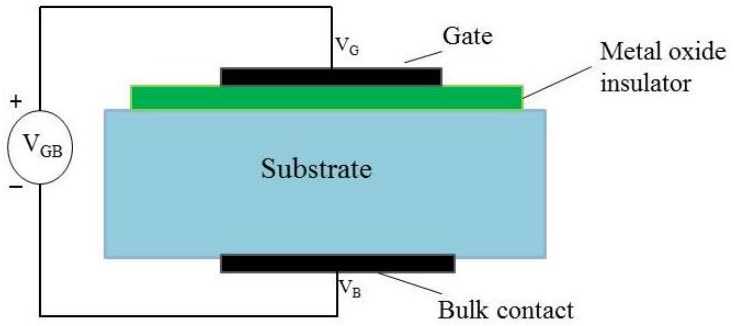

Figure 2.3: Typical setup of a metal oxide semiconductor. Oxygen is absorbed to the metal oxide layer. The oxygen reacts with the target species which allows for electron flow. This causes a change in conductivity that is proportional to the concentration of the target species.

For example n-type sensors (e.g., tin oxide or zinc oxide) react with reducing gases CO to release electrons while p-type sensors (e.g., nickel oxide or cobalt oxide) react with oxidizing gases like O_2, NO_2 or O_3 to consume electrons, producing holes (i.e., charge carriers)[38]. Both of these actions increase the conductivity of the oxide. However though being able to detect a variety of gases, MOS sensors do not have very good gas selectivity and can cross respond to other gases. Furthermore the sensitivity and selectivity is determined by the operating temperature and so can be affected by ambient temperature changes, as well as humidity effects. Detection limits in the ppm region have been reported for methane detection in laboratory settings[39]–[41].

To summarise, these non-optical techniques, despite limitations such as sensitivity to humidity or cross-interference from other gases, meet a demand for low cost detection options that offer sufficient sensitivity for the specific applications they are being used in. For example electrochemical sensors can be used for indoor air quality monitoring in

the workplace, where the sensor is in a stable fixed location and is accessible if calibration or replacement is needed. For more specialist applications, e.g. measuring atmospheric gas distributions in the presence of varying ambient conditions or for trace gas detection over a large area, such as identifying the location of fugitive emissions from natural gas networks, optical gas sensors have a number of advantages over their non-optical counterparts. Some of the technologies that are used to make these types of measurements are discussed in Section 2.3.

2.2 Optical absorption spectroscopy

2.2.1 Principle of optical absorption spectroscopy

The principle of operation of optical sensors is based on the interaction of electromagnetic radiation with matter; whether by emission, scattering or most commonly for gas detection, absorption of radiant energy. Optical absorption spectroscopy uses the fact that for each molecule, there are a number of frequencies at which molecular transitions occur. These transitions can be rotational, vibrational or electronic depending on the frequency and thus amount of energy that has been absorbed, as seen in Figure 2.4.

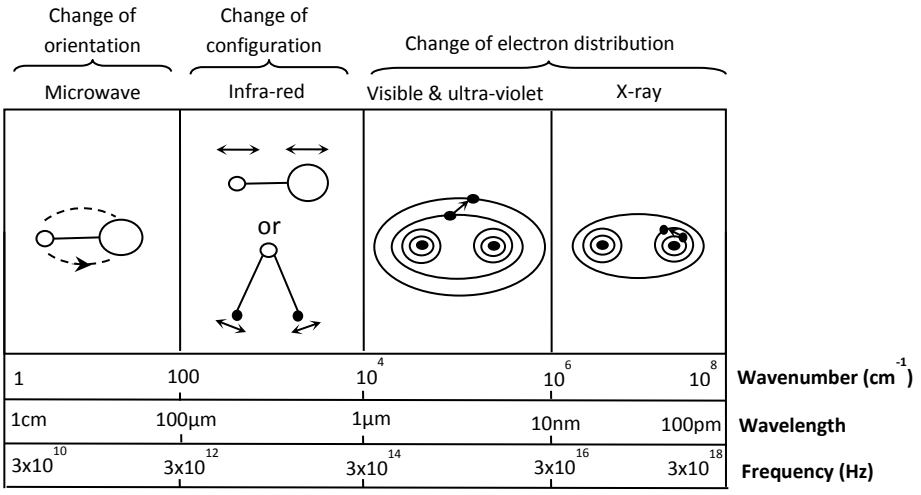

***Figure 2.4: Dominant molecular energy states at various wavelengths, adapted from Banwell et. al*[42].**

For gas detection the infrared region, i.e. $3x10^{12}$ - $3x10^{14}$Hz (100-1µm) is the most valuable spectroscopically[42], with many of the fundamental absorptions in this region. Vibrational energy is dominant in this region where bending or stretching of

molecular bonds occurs. In the higher energy UV, visible (vis) and x-ray regions, the main energy states manifest as electronic transitions, i.e. promotion of inner electrons with X-rays and outer electrons in the UV-vis region. This type of spectroscopy can be used for identification of gases such as hydrogen sulphide and formaldehyde[43]. Each molecule will have a different and unique set of molecular transitions depending on its structure, which presents as absorption bands at various regions in the electromagnetic spectrum. Optical gas detectors tend to use only one absorption region to quantitatively determine the gas concentration. The chosen region ideally contains a large absorption feature of the target gas and no absorption features of background gases that could potentially obscure the signal.

2.2.2 How selectivity is achieved - Gas absorption lines

Selectivity for the species of interest is achieved by using a light source that emits at a wavelength where absorption lines characteristic of, and unique to, that species occur. Most gas molecules have fundamental bands in the mid-infrared (3-14μm) region, whereas overtone and combination bands lie in the near infra-red (0.75-3μm) region. In the case of methane, there is a strong fundamental absorption at 3.3μm[44] due to the stretching vibration of the C-H bonds. At 1.65μm[45] the first harmonic of this fundamental absorption occurs, due to population of a higher energy vibration level. This occurs at approximately twice the frequency of the fundamental and has an absorption line two orders of magnitude weaker. Another major greenhouse gas, carbon dioxide, exhibits fundamental absorption lines[46] at 14.88μm, due to symmetric stretching vibrations, symmetric bending at 7.2μm, and 4.25μm due to asymmetric vibrations. It has an overtone band at 1.57μm[47], again two orders of magnitude weaker than the fundamental, corresponding to the rotation-vibrational states of the molecule, i.e. the “finer structure” vibrational states due to concurrent changes in the rotation of the molecular bonds.

Ideally, detection of fundamental absorption lines would be preferable as they are stronger features, however in practise producing light sources that excite in the mid IR region are more expensive[48], [49] and in general more difficult to fabricate[50]. Furthermore, as will be discussed in Chapter 4, in this body of research the wavelength region over which reflectivity of the integrating sphere wall is highest is also a factor for

consideration. Thus only the overtone bands for methane (at 1.65μm), as seen in Figure 2.5. The experimental work that will be outlined in the experimental Chapters demonstrated gas detection for methane gas however the techniques can be easily translated to other wavelengths and gases.

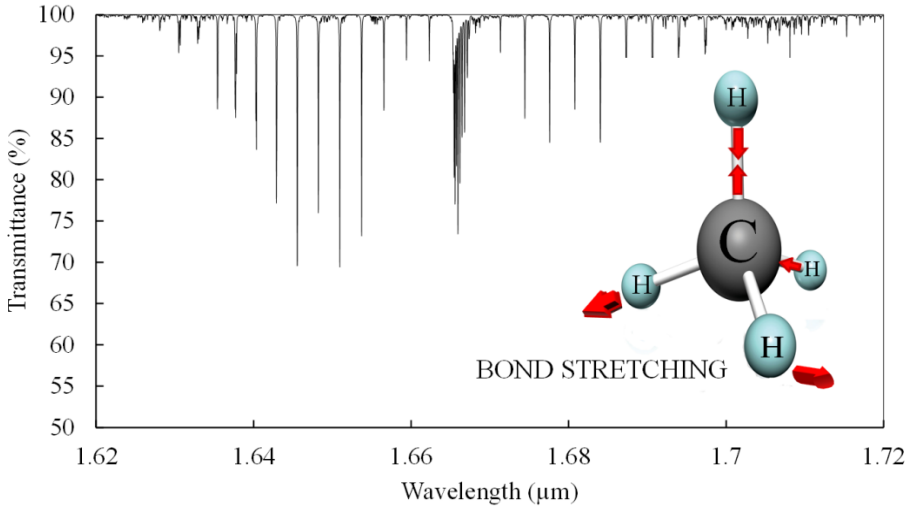

Figure 2.5: Theoretical methane (100% volume) transmittance spectrum with, in particular, 1.65μm absorption due to C-H bond stretching. Calculated using data from Hitran database[51]***. The pathlength is 1m.***

The resultant spectral line will not be infinitely "sharp"; the continuous motion of atoms and molecules means that there will always be some broadening of the absorption line. The type of broadening can be classed into three regimes, natural, Doppler (thermal) or collision (pressure) broadening. Natural broadening is related to the quantum mechanical uncertainty in energy levels, inherent in all atoms. The uncertainty in energy ΔE and lifetime Δt of the excited state can be described by the uncertainty principle[52].

$$\Delta E \Delta t \approx \frac{\hbar}{2} \qquad 2.1$$

where ħ is the reduced Planck constant (h/2π). It can be seen from this equation that for example short lived states would have larger uncertainties in energy. Natural broadening is unaffected by temperature and pressure and represents the minimum line width of the spectral line (on the order of 10^{-11}cm^{-1}). This type of broadening is not often directly observed, except potentially at the edges of the line profile at low pressure and has a Lorentzian profile as seen in Figure 2.6.

Another type of broadening, termed collision (or pressure) broadening also has a Lorentzian profile, but with a much larger line width of the order of $0.1cm^{-1}$ at atmospheric pressure[53]. In this case the molecular collisions in air reduce the lifetime of the upper state, thus increasing the energy uncertainty and resulting in a broadened linewidth. The extent of broadening is affected by both pressure and temperature, which affects the rate of collisions. This type of broadening dominates at higher pressures, e.g. >100 torr. Due to smaller peak absorption coefficients and more broadening and overlapping of lines in larger molecules, this regime tends to be more applicable to lighter molecules, such as methane.

At lower pressures, e.g. below 10 torr, Doppler (or thermal) broadening often dominates[53]. Here, due to the thermal motion of the atoms, those travelling towards the detector at a certain velocity will have a distribution of frequencies due to Doppler shift, which differ from atoms at rest. For non-relativistic molecular velocities the Doppler shift is given by

$$\omega = \omega_0 \left(1 \pm \frac{\upsilon}{c}\right) \qquad 2.2$$

where ω_0 is the angular frequency for an atom at rest, υ is the velocity of the atom and c is the speed of light. The average speed of the molecules will be proportional to the temperature. The molecular velocities are described by a Maxwell-Boltzmann distribution resulting in a line shape that follows a Gaussian function[53]. The linewidths due to Doppler broadening tend to be 1-2 orders of magnitude smaller than pressure broadened lines.

The resultant line shape for a sample is usually a combination of all of these phenomena. The contribution of each will be dependent on the temperature and pressure mainly, the result of which will be a convolution of a Lorentzian with a Gaussian profile, as seen in Figure 2.6, known as a Voigt profile[54].

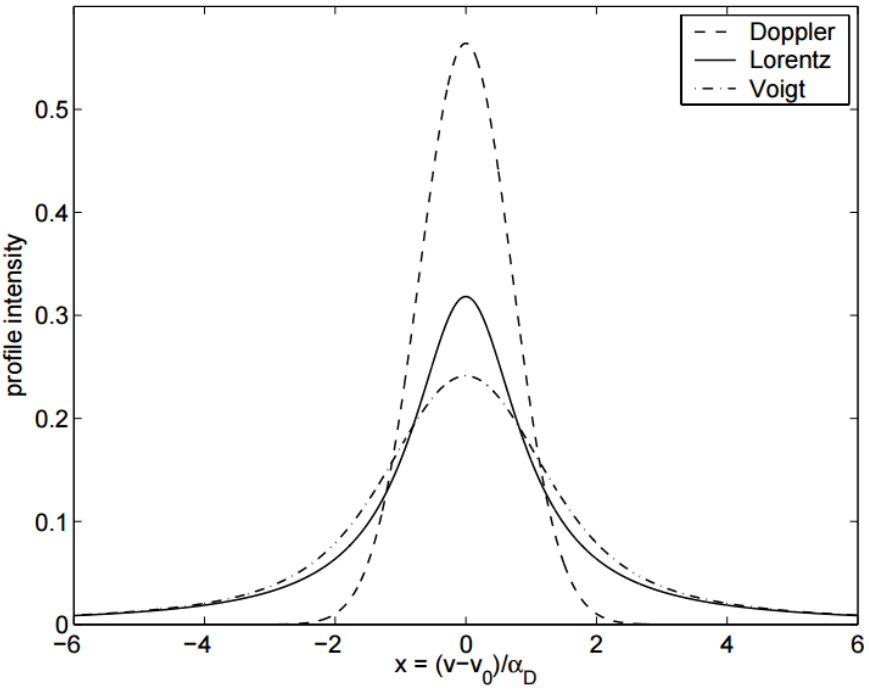

Figure 2.6: Comparison of Doppler, Lorentz and Voigt profile. The Doppler profile and Lorentz profile have the same line half width i.e. $\alpha_L = \alpha_D$. The Voigt profile corresponds to the convolution of Doppler and pressure broadening. Taken from [55]

Typical linewidths for atmospheric species are in the range of $5x10^{-3}$-$2x10^{-2}cm^{-1}$ in this region which affords increased resolution as these widths are smaller than the spacing of the rotational lines of many of the molecules of interest[53]. However vacuum pumping is required to achieve these linewidths and so measurements are limited to point sampling. The gas measurements in this work fall under the atmospheric pressure broadened regime.

2.2.3 Quantitative measurements - Beer Lambert law

Quantitative measurements of absorption are governed by the Beer Lambert law[56] which states that the absorbance of a beam of collimated monochromatic radiation in a homogeneous isotropic medium is proportional to the absorption path length, *l*, and to the concentration, C, or in the gas phase, to the partial pressure of the absorbing species. The law can be expressed as[56]:

$$A = log_{10}\left(\frac{\Phi_i}{\Phi_e(\alpha)}\right) = \varepsilon CL \qquad 2.3$$

where $\Phi_e(\alpha)$ is the radiant flux transmitted through the cell in the presence of an absorbing medium (W), Φ_i is the radiant flux incident on the gas cell (W), and *L* is the optical path length of the cavity (m). The other two variables, the gas concentration, C (in ppm for example) and ε, the specific absorptivity of the gas, (ppm m^{-1}) are often quoted as their product, which is termed α, the absorption coefficient (m^{-1}).

The conditions under which the Beer Lambert law is valid include[57]

- That the incident radiation is nearly monochromatic i.e. has a narrow bandwidth.
- That the absorbers act independently of each other. At high concentrations some ions at close proximity to each other can electrostatically interact, changing the absorption coefficient of the molecule. A change of refractive index can also occur at high concentrations or molecules can form dimers.
- That the absorbing medium is homogeneous and does not scatter the radiation. Scattered light may not reach the detector and so may result in an overestimated concentration measurement for the species of interest.
- That the incident flux is not large enough to cause saturation of the transition. Optical saturation may lead to stimulated emission and/or non-linear optical effects.

In-situ, quantitative gas measurements can be compromised by factors, illustrated in Figure 2.7, such as turbid samples causing scattering effects, optical components causing back reflections or interference due to creation of standing waves between surfaces. Furthermore, other species which also absorb light at that wavelength may be present and can obscure absorption bands of the species of interest especially if it is present in lower concentrations.

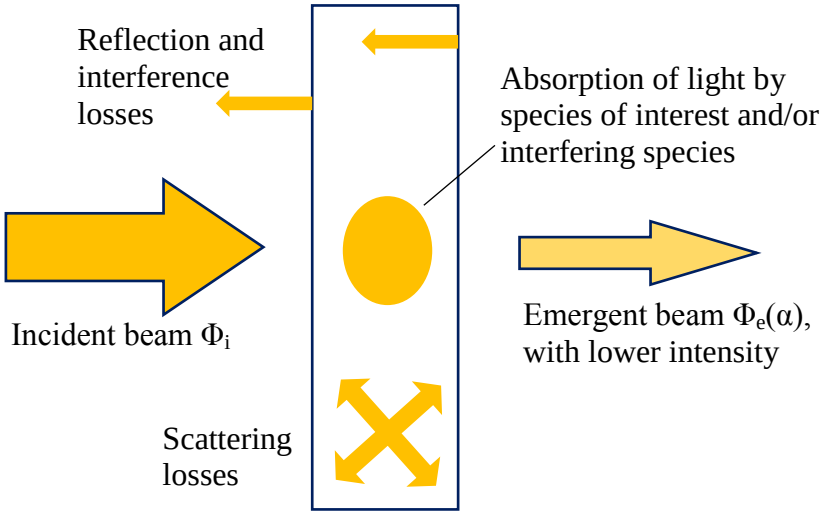

Figure 2.7: Typical light interactions when passing through a cell; incident light intensity is reduced due to absorption, reflection, interference and scattering effects.

It is some of these scattering and interference factors that the use of an integrating sphere aims to alleviate, while still providing a sensitive detection technique. The advantages and limitations of using an integrating sphere will be discussed in more detail in Chapter 4. The following sections describe some optical technologies, from the widely commercially available non-dispersive infrared (NDIR) sensor to the more specialist technologies such as cavity ringdown spectroscopy (CRDS) and off-axis integrated cavity optical spectroscopy (OA-ICOS).

2.3 Optical gas sensors

Optical gas sensors, though in general more expensive than their non-optical counterparts, are increasingly becoming the technology of choice due to their superior sensing capabilities for certain applications, such as remote sensing. One of the major advantages of optical gas sensing is that the detector does not directly interact with the gas, unlike for example a MOS or EC sensor where exposure to high concentrations of gas can have a detrimental effect on the reactive area of the sensor. As a result optical gas sensors tend to have a longer lifetime (e.g. >10years for some IR sensors as opposed to 6-24 months for an EC sensor).

2.3.1 Non dispersive infrared (NDIR)

NDIR sensors are termed “non-dispersive” as only transmission of the required wavelength is allowed (due to the use of broadband lights sources and filters) and so the

whole spectrum is not resolved. It is one of the most widely used optical techniques commercially, such as for indoor air quality analysis and industrial process control. NDIR sensors are commonly used as methane sensors, demonstrating detection capability down to low ppm levels[58], [59]. Detection limits tends to be in the low 100s of ppm for commercial sensors. The general setup comprises an infrared source, a gas cell, and a detector with integrated optical bandpass filters, as seen in Figure 2.8. The optical filter is chosen to filter out the wavelengths at which the target gas does not absorb, thus providing a sensor that is specific to that gas.

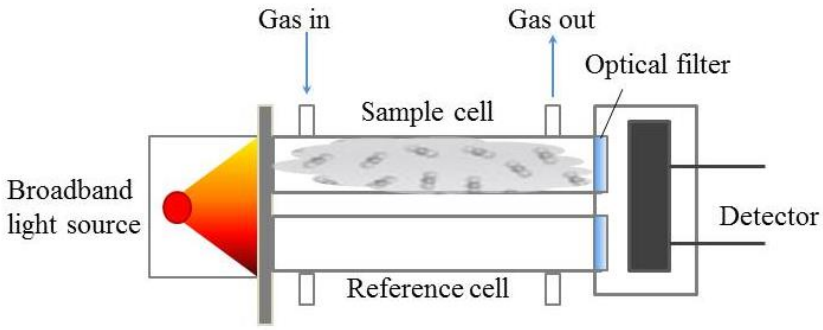

Figure 2.8: Typical setup of NDIR sensor. Detection is achieved by applying an optical filter that only permits transmission of the wavelength of interest, i.e. the absorbing region for the target species. A reference cell with an optical filter at a nearby wavelength is used to correct for intensity. Adapted from [60]**.**

Quantification of the gas is governed by the Beer Lambert law[56] as seen in Section 2.2.3. These sensors offer one of the most cost effective optical solutions, with relatively few components, allowing compact designs[61]. As the technique involves measuring a gas density, the measurement can be affected by ambient temperature and pressure changes. Temperature and pressure sensors are often included to correct for these effects. To correct for potential fluctuations in source intensity, another filter will be used at a nearby wavelength, i.e. one that the gas does not absorb light at.

For NDIR sensors, a limiting factor for sensitivity to the gas is the pathlength of the gas cell. One way to improve this is to reflect the light multiple times within the gas cell, thus achieving greater gas-light interaction within the same volume. The optical techniques described in the following sections are able to apply this approach because the lasers have a collimated beam.

2.3.2 Tunable diode laser spectroscopy (TDLS)

TDLS has been employed in this body of research for the ratiometric scheme as described in Chapter 5. The term typically refers to techniques where absorption measurements are made using a tunable diode laser. The characteristics of this type of laser include a narrow linewidth (tens of megahertz) as well as being tunable over a small wavelength region (up to tens of GHz)[23]. The tunability is achieved by controlling the temperature and electrical current of the laser. As a result, measurements can be made with very high resolution and specificity to the gas of interest. Other benefits include fast response times, portability, and non-destructive sampling[62]. The TDLS techniques that will be described in the following sections have achieved greater sensitivity through the use of specialist gas cells, namely multipass, resonant and non-resonant cavities.

2.3.3 Direct absorption spectroscopy (DAS)

Direct absorption spectroscopy (DAS) is probably the most straight forward TDLS technique. In DAS, the fast tuning capability of the diode laser is exploited by ramping the injection current which scans the wavelength across the gas absorption line. The resultant signal is a rising baseline with a dip corresponding to the gas absorption line. The measurement is effectively self-referenced by comparing the higher off gas line intensity with the attenuated on-gas line intensity. The off-gas line portion of the baseline can be used to normalize for any changes in the laser intensity e.g. due to window contamination or loss of laser power.

The biggest disadvantage of DAS is that, especially for low concentrations, it relies on measuring a very small signal against a large background[63]. As a result, a potentially small absorption signal can become obscured by the baseline noise which thus becomes the limiting factor in the sensor performance.

One strategy that is employed to achieve greater sensitivity is the use of a multipass gas cell, such as a Herriott cell[64]. This cell consists of two spherical mirrors with holes for entering and exiting beams in the mirrors. The beam traverses an adjustable number of times depending on the separation and curvature of the mirrors giving an effectively long pathlength (up to 10s of metres[65]), corresponding to the length of the cell multiplied by the number of passes made. However, these cells are susceptible to

formation of standing waves between reflective surfaces which can result in optical interference effects if beams overlap with each other. A detection limit of 20ppb has been reported for methane detection (at 1650nm), where a multipass cell (length 252m) has been used to achieve enhanced sensitivity[66].

2.3.4 Cavity ringdown spectroscopy (CRDS)

CRDS has been successfully deployed on research aircraft as well as in ground based settings, providing a highly sensitive technique for measuring greenhouse gas emissions. The typical setup[67], as seen in Figure 2.9, comprises a coherent light source, usually pulsed, a high finesse resonant optical cavity formed by two or more mirrors and a fast photodetector.

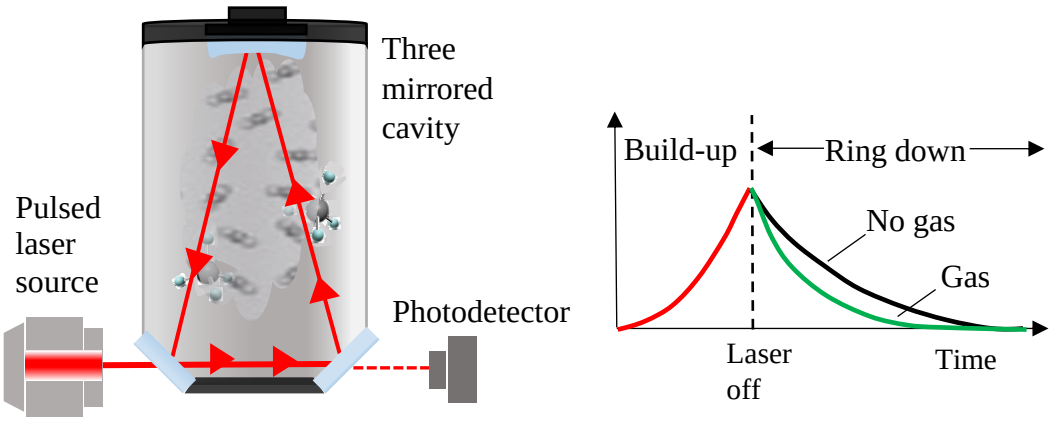

Figure 2.9: CRDS setup with typical signal output. In the presence of an absorbing species, the rate of decay of light i.e. the ringdown time, will be proportional to the concentration of the species. Adapted from[68]**.**

Light is injected into the resonant cavity and allowed to build-up, reflecting back and forth thousands of times, dependent on the finesse of the cavity, which typically have reflectivity of >99.99%. After sufficient light has been injected, the light source is interrupted or switched off, and as the mirrors are not 100% reflective, some light can escape through the mirrors causing the overall transmitted light intensity to decay exponentially over time. This rate of decay is measured using a fast detector behind one of the mirrors, where, in the absence of an absorbing species, the rate of decay is a

function of the reflectivity of the cavity mirrors, scattering, as well as the alignment. The effective pathlength is thus given by

$$L = c\tau_0 \qquad 2.4$$

where c is the speed of light and τ_0 is the decay constant, i.e. time taken for the intensity of light to fall to 1/e of the initial intensity and is dependent on the mirror reflectivity and other loss factors such as scattering or refraction.

When an absorbing species is introduced, the rate of decay will also be dependent on the magnitude of the absorption. And so this technique works by measuring the change in the rate of decay, the "ring-down time" of the light when in the presence of an absorbing species. This has the advantage of immunity to intensity fluctuations as measurements are made relative to the initial intensity[69]. Furthermore the thousands of reflections can provide a pathlength on the order of kilometres, making this an extremely sensitive technique, allowing measurements of concentrations down to ppt levels. Limits of detection for methane have been reported at 0.5ppb for the overtone band at 1.654μm and 0.16ppb when using the fundamental band in the mid-IR region.

A resonant cavity differs from a multipass cell in that rather than having a folded setup, the arrangement of the mirrors facilitates the creation of standing waves which can lead to increased intensity due to constructive interference. In this case the laser must be in resonance with the narrow cavity mode; which can lead to difficult alignment. The use of a short pulsed light source in CRDS eases the stringent mode-matching condition. However a lack of customer qualified performance as well as costly components (pulsed sources, fast detectors and highly reflective mirrors) has prevented the use of this technology on a large scale. Compared to these resonant cavities, the mean reflectivity of the integrating sphere wall is lower (e.g. 99.2% at 532nm) giving an achievable pathlength of up to 10m rather than kms. A pathlength of this magnitude would not facilitate the resolution that is typically achieved by the high finesse resonant cavities used in CRDS.

To overcome this particular issue, Fry *et. al*. developed a high reflectivity diffusive material (with measured reflectivity values as high as 0.99919 at 532 nm)[70]. When compared with a commercially available material (often used in integrating cavities),

which has a wall reflectivity of 0.992 at that wavelength, they calculated that for a sample with an absorption coefficient of 5×10^{-5} cm^{-1}, the resultant decrease in decay constant would be 23.4ns for their high reflectivity materials and 0.3ns for the commercial material. They concluded that with this increased sensitivity an integrating cavity could be implemented in combination with CRDS to provide a powerful technique for making absorption measurements, termed integrating cavity ring down spectroscopy (ICRDS)[71]. This will be discussed in more detail in Chapter 4.

2.3.5 Off axis integrating cavity output spectroscopy (OA-ICOS)

OA-ICOS is also a cavity enhanced technique but differs from CRDS in that an intensity based measurement is made rather than time based. The measurement is integrated over a time period that is much longer than the cavity "ringdown", allowing for the use of simpler electronics, e.g. the detector bandwidth can be in the region of kHz as opposed to MHz. The setup is similar to CRDS, i.e. a high finesse resonant cavity is used, however in OA-ICOS, a continuous wave laser beam is directed off axis with respect to the cavity.

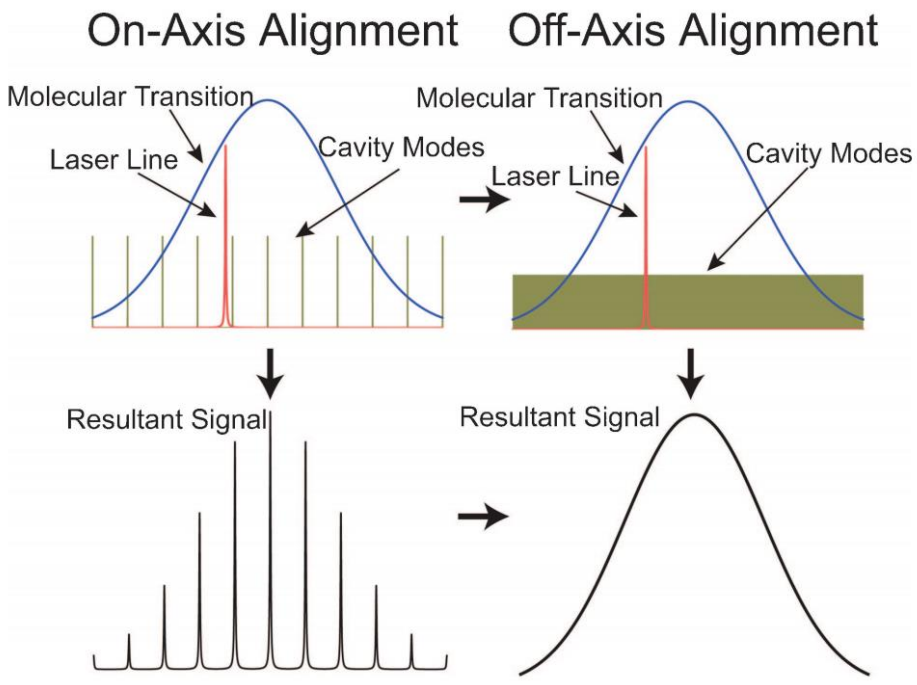

Figure 2.10: Mode spectra of on-axis vs off-axis mode structure. In the case of off-axis alignment, there are many cavity modes for each molecular transition, the laser line width is broader than the free spectral range of the cavity but narrower than the molecular line. Taken from [72]

This off axis alignment removes the need to lock the cavity to the laser wavelength. The cavity transmission is monitored while averaging the cavity mode structure, either by oscillating the cavity length or the wavelength such that the laser couples to a large number of transverse cavity modes. By exciting a number of modes and integrating in this way, better noise characteristics are achieved while also easing alignment tolerances. The off-axis path is aligned so that the multiple reflections are spatially separated in an elliptical pattern within the cavity until the light retraces its path through the cavity. As with CRDS the achievable pathlength with OA-ICOS is a function of the mirror reflectivity. The pathlength value can be quantified by inputting an absorbing sample with known absorbance and using the lineshape peak to infer the pathlength. Achieving more robust alignment in this way does have some trade-offs. These include a reduction in throughput power due to longer integration times, as well as potential additional noise due to laser fluctuations when dithering. Nevertheless the technique has been used commercially, such as for airborne mapping of atmospheric ammonia[73]. For methane, a detection limit of 0.3ppb has been reported in an academic research laboratory using a wavelength of 1.65μm and with a pathlength of several kilometres[22].

One technique of note that can be applied to both CRDS and ICOS is phase shift detection. In both cases, a modulated light source is inputted to the resonant cavity and an incident phase angle is measured. The optical loss can then be extracted from the measured phase shift relative to the initial measured phase e.g. to determine the reflectance of the optical resonator[74], or in spectroscopic applications for making sensitive absorption measurements of gas species[72], [75]. This method has the potential to simplify pathlength calibration whilst simultaneously allowing other measurements to be made[76]. One challenge for this technique is that of amplified spontaneous emission (ASE) from the laser which can cause large errors in the measured phase shift, particularly in the case of PS-ICOS where the intensity is low. Kasyutich *et. al*. [77] corrected for this by measuring the amplitude and phase of the light when the rear mirror of the cavity was tilted as it was found that this related to the ASE contribution. It was additionally shown that for a cavity base length 43cm with an enhancement factor of 1122, and using an interference filter to suppress the ASE, a

noise equivalent detection limit (S/N ≤ 1) of 0.24 ppbv was achieved for NO_2 over an integration time of 80s[75].

2.4 Summary

As detailed in section 2.2.2, absorption spectroscopy can offer high selectivity to the gas of interest if an appropriate wavelength region is chosen. This region should contain an appreciable absorption line for the species of interest but no absorption features of potential interfering gases. For this research the overtone band of methane at 1.65µm satisfies these requirements, also corresponding to a wavelength region where the integrating sphere wall reflectivity is high. In general, academic literature, as well as the commercial market lauds the benefits of optical detectors for their high sensitivity and specificity with powerful capability for remote detection. However the hurdles over which some non-optical counterparts triumph include cost, ease of use and ruggedness. It was with these challenges in mind that this research approached implementation of an integrating sphere into an optical gas detection system.

The techniques, as discussed in section 2.1 and section 2.3 are summarised below in Table 2.1 in terms of their advantages (+) and limitations (-).

Table 2.1: Commercially available optical and non-optical technologies. Advantages (+) and limitations(-) of each.

Technique	Notes
Optical	
Non-dispersive infrared (NDIR)	Measures change in intensity due to gas absorption with continuous laser source in the infrared. **(+)** Selective, sensitive, does not suffer from drift, low maintenance. **(–)** Limited to one species, can be affected by scattering particles in the optical beam path. *Typical specifications: £200-250, cylinder 20mm diameter x 16.5mm high, 10g weight, up to 10yr lifetime, 6 month calibration interval, operated by non-technical user

Direct absorption spectroscopy (DAS)	Measures change in intensity due to gas absorption using a tunable laser. **(+)** Selective, easy to use. **(–)** Sensitivity often limited by baseline noise as SNR ratio is low. *Typical specifications: £10-30k (depending on required sensitivity i.e. multigas, ppm detection limits), 439-1500 mm H x 475-900 mm W x 146 - 450mm D, 20kg weight. Non-contact sensing. Enclosed non-contact sensor, can be remotely accessed by manufacturer to allow troubleshooting
Cavity ringdown spectroscopy (CRDS)	Measures rate of decay of light intensity in a resonant cavity. **(+)** Very low detection limit (ppt), immune to intensity fluctuations. **(−)** Can be relatively high cost as high reflectivity mirrors required, complex alignment. *Typical specifications: £30-100k, 450mm x 200mm x 450mm, 30 kg weight, fully enclosed system to facilitate minimal technical input, 3-6 month calibration intervals
Off-axis integrated cavity output spectroscopy (OA-ICOS)	Measures intensity decay in a resonant cavity. **(+)** Very sensitive due to long integration times, can use simpler electronics in kHz region (as opposed to MHz in CRDS) **(−)** Low throughput due to long integration times, can suffer from laser noise. *Typical specifications: £8-80k (depending on required sensitivity), 220mm x 480mm x 600mm, less specialist input required than CRDS, user can remove and clean mirrors, 6 month calibration interval

Non-Optical	
Electrochemical (EC)	Uses an electrochemical reaction to generate a current which is proportional to the gas concentration. **(+)** High sensitivity, linear output, easy operation. **(–)** Limited shelf-life, sensor lifetime degraded by ambient temperature and humidity, suffers cross-interference. *Typical specifications: £35, 10mm x 6mm x 0.75 mm, 5-10g weight, 1-2yr lifetime, can be irreversibly damaged by over concentration, or dust or changing ambient conditions, e,g. temp, humidity, non-technical operator, tend to replace rather than repair
Flame ionisation detector (FID)	Measures the current generated by flame ionised gas particles contacting with a collector plate **(+)** Large measurement range, rugged, easy to use, low maintenance **(–)** Requires a hydrogen flame, destroys the sample. *Typical specifications: £10k, 343mm × 262mm × 81mm, 8kg weight, up to 10yr lifetime, fully enclosed system, easy to operate and calibrate by non-technical user.
Metal oxide sensor (MOS)	Metal oxide layer changes resistance in response to gas adsorption **(+)** Long lifetime, short response time, wide range of target gases **(–)** Low selectivity, high energy consumption, sensitive to environmental factors, non-linear output *Typical specifications: £2-10, 5.5mm x 7.5mm x 2.55 mm, requires heating, easy to operate, active surface can become contaminated and cross responds to other species, better for identifying presence of sample rather than quantifying, tend to replace rather than repair.

* Specifications have been obtained from datasheets provided by commercial manufacturers including SGX Sensortech (NDIR), Servomex (DAS), Picarro (CRDS), Los Gatos Research (OA-ICOS), Figaro (EC), Thermo Fisher scientfic (FID), Alphasense (MOS)

In this research, a TDLS approach is taken for detection of methane at 1651nm. This wavelength region is commonly used in the telecommunications industry and so components are available at low cost. A direct absorption spectroscopy approach has been taken for simplicity to investigate the application of an integrating sphere in this field. A temporal based approach, such as cavity ring down spectroscopy, CRDS, offers the advantage of a pathlength on the order of kms due to the high finesse cavity (>0.9999 reflectivity). By comparison, due to the comparatively low sphere wall reflectivity i.e. ≈0.9999 for CRDS vs. ≈0.987 for a Spectralon^{TM} integrating sphere at 1651nm, the achievable pathlength of an integrating sphere based gas cell would more likely be <10m. The aim is not to compete with highly sensitive trace gas detection systems such as CRDS or OA-ICOS. Rather the focus is on creating a detection system that achieves adequate sensitivity whilst being cost-effective and robust.

A pathlength of this magnitude is still capable of achieving detection limits down to low ppm levels[78], and potentially lower with further modulation techniques[79].

.

3 TDLS system performance

"Although IR spectroscopy has long been a workhorse technique in analytical laboratories, many improvements have been made in the past few years. Anything that can be done to improve the signal-to-noise ratio in IR-based measurement techniques will help drive the use of IR into new areas of application, detectors with lower noise would support higher sample throughput by requiring fewer scans per sample"- Spectroscopy[80]

When designing a gas detection system there are numerous factors to consider in terms of performance, such as how to achieve the required sensitivity and selectivity towards the species of interest, and then how to preserve that performance once introduced to a potentially less stable in-field application. This chapter aims to provide an insight into some of the common challenges for optical TDLS sensor design in particular. The chapter begins by discussing strategies that are typically employed to enhance sensor performance, namely the use of multipass cells, or modulation techniques. Some of the issues that can ultimately become the limiting factor in sensor performance are then discussed, such as sources of noise, cross sensitivity to other species and optical interference from system components. The summary section discusses these enhancing and limiting factors in terms of this body of research, and the most pertinent challenges faced when considering implementation of an integrating sphere in a gas detection system.

3.1 Performance enhancement strategies

Many of the performance enhancement strategies discussed here have been employed for this research. As well as the advantages of implementation of these strategies, the challenges that they introduce are considered.

3.1.1 Multipass cell

The invention of the multipass cell, which essentially comprises mirrors of various sizes, curvature and distance to produce multiple reflections of the incoming beam, facilitated greater sensitivity by giving a much longer effective pathlength in a relatively small volume of space. Conventional multipass cells are mainly based on either the White cell or the Herriott cell design. The White cell, first described in 1942 by John White[81], consists of three spherical concave mirrors with the same radius of curvature, as seen in Figure 3.1.

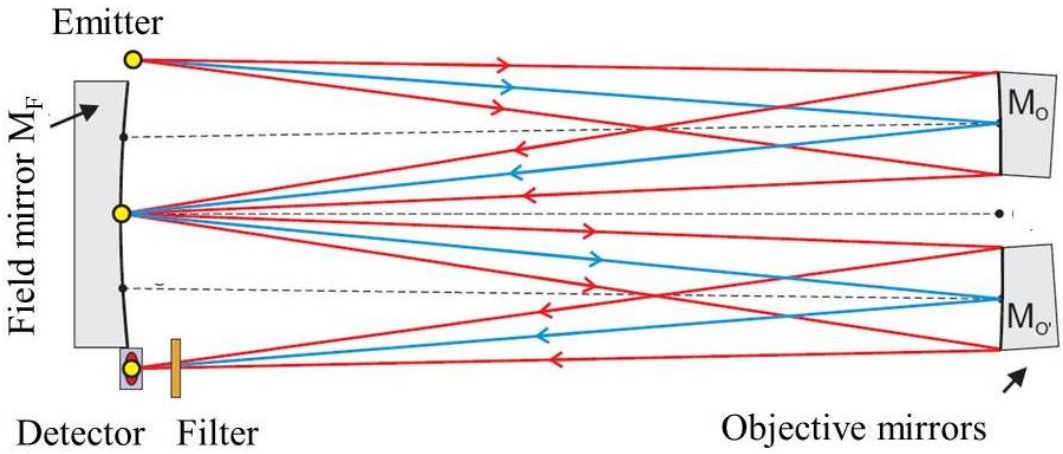

Figure 3.1: White's cell multi-pass diagram. The blue lines correspond to the chief rays whilst the red lines represent the marginal rays. The light beam bounces repeatedly between the field mirror and two objective mirrors until it is finally projected onto a detector Taken from.[82]

This cell allows for high numerical aperture beams, which was typical of the broadband sources used at the time, as the light is refocussed on the opposite mirror during each pass. The number of achievable passes is determined by the separation of the centre of curvature of the mirrors and the number of passes occurs in multiples of 4. However the mirror assembly blocks[83] do not remain very stable e.g. can suffer mirror misalignment, and thus beam displacement due to thermomechanical instability, and as a result this cell is not often used in commercial applications.

Conversely the Herriott cell, detailed in 1965 by D. Herriott[64], offers a more stable cell (as there are two rather than three mirrors to be aligned) and, as mentioned in section 2.3.3, consists of two spherical mirrors with holes for entering and exiting beams in either one or both mirrors depending on the required design. The successive

passes follow an ellipse and the overall pathlength is determined by the distance between the mirrors.

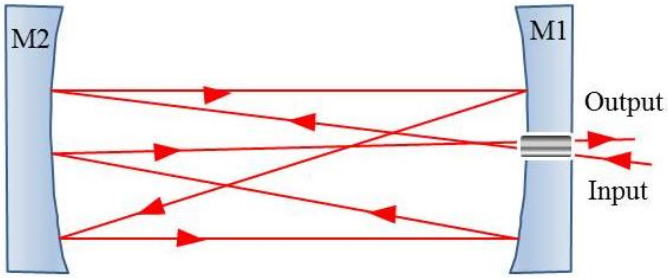

Figure 3.2: Herriott cell multipass diagram. Successive passes follow an ellipse and the overall pathlength is determined by the distance between the mirrors.

In today's commercial applications[84], [85] Herriott cells employ either the standard configuration or an astigmatic variant. Astigmatic mirrors offer a greater distribution of the beam spot pattern, giving better separation between beam passes and in general, longer pathlengths. These mirrors can be expensive though as they require precision manufacturing[86]. A consequence of the parallel setup is the potential for formation of etalons both between the cell itself and from the windows. Minimising these effects, as well as avoiding beam overlap whilst achieving a long pathlength can make the alignment of the cell difficult, with tight tolerances towards misalignment[87]. In general though astigmatic Herriott cells are thought to be relatively stable whilst providing an impressive pathlength:volume ratio[88]. To avoid potential issues with absorption line overlap due to broadening, these cells are sometimes operated at low pressure where the absorption line will be Doppler limited[89].

Another cell of interest where cell dimensions are further reduced is that of the circular multireflection cell[90]. In this case the beam encounters the walls of a polished aluminium cylinder (with height of 3cm and diameter of 8cm) producing multiple reflections concentrated in the centre of the circle. This is particularly advantageous for applications such as process monitoring in aerosol flow reactors where the gas flow is also concentrated in the centre of the flow path. Additionally the number of reflections is adjusted only by adjusting the angle of the entering beam. This means that the alignment of the cell is completely external to the cell. This is useful for applications where the region in which to interrogate may be very narrow, e.g. temperature

controlled chambers for accelerated aging tests[91]. Pathlengths of up to 1.05m have been achieved but further optimisation of beam size and focus is needed it has been concluded.

Hollow waveguide fibres have also been used as a means of increasing the gas-light interaction. Here the light is confined in a narrow hollow capillary where only certain modes are propagated. This is achieved by using a photonic bandgap guiding mechanism rather than a core region with a high refractive index i.e. the guiding principle for typical optical fibre. Gas is introduced into these hollow regions, which facilitates an impressive pathlength:volume ratio (>1m interaction length with μL of sample[92]). Other advantages include simplicity, lack of optical misalignment and ruggedness. However the propagation losses can be large which can represent a limiting factor. There is also the possibility for sample adhesion to the walls due to the large surface area of the fibre[93].

The integrating sphere by contrast has an optically rough surface resulting in diffuse reflections. Unlike for example the Herriott cell where a beam is folded multiple times producing passes of fixed length, the integrating sphere has multiple overlapping passes with different lengths. There is a limit to the achievable pathlength for any given multipass cell. This is the case as the enhanced sensitivity gained by the increasing number of passes will be offset by an increasing attenuation in output power due to imperfect reflectivity of the mirrors[94].

Table 3.1 provides a summary of these cells and some of their characteristics.

Table 3.1: Comparison of different embodiments of multipass cell that could be used in TDLS applications, adapted from [62]

Approach	Advantage	Path - Length (m)	Number of passes	Volume (L)	Length/ Volume ($10^3 m^{-2}$)	Ref
Herriott cell	Optomechanically stable, pathlength variability	30	74	1	30	[25]
Astigmatic Herriott cell	Very long pathlengths	36	182	0.3	120	[86]
White cell	Accepts high NA beams	7.5	12	10	0.75	[81]
Circular multi-reflection cell	Pathlength alignment outside cell, simple cylindrical optic	1.04	17.5	0.085	12	[90]
Hollow core fibre	Small sample volume requirement, simple alignment	27	1	$3x10^{-6}$	$8x10^6$	[92]
Integrating sphere	Simple alignment, no etalon formation	4.4	65	0.5	9	[24]

Though it cannot offer the optical pathlength of, for example, the Herriott cell (e.g. 74m vs 9m) the integrating sphere does have a significant advantage in its tolerance to misalignment as well as removing the periodicity between beams which often results in formation of etalons. The advantages and limitations of the integrating sphere will be discussed in more detail in Chapter 4.

3.1.2 Modulation

In situations where systems are noise-limited, one of the strategies for improving sensitivity is to move the detection region to a higher frequency, and thus away from common low noise sources such as laser intensity noise, intensity changes from mechanical instabilities and other external fluctuations. This is achieved by sinusoidally modulating the laser injection current whilst the laser wavelength is tuning over a gas absorption line. The modulated light interacts with the species of interest, producing a difference signal which is proportional to the species concentration. The signal can then be detected and demodulated at that frequency, where the laser noise is greatly reduced[95].

Two modulation techniques that are commonly implemented with TDLS modulation are frequency modulation spectroscopy (FMS) and wavelength modulation spectroscopy (WMS). Both techniques involve sinusoidally modulating the laser current however the modulation frequency differs for the two techniques. For WMS the modulating frequency is in the kHz to low MHz range whilst for FMS the modulating frequency is in the MHz-GHz range. Figure 3.3 illustrates how the signal interacts with the gas absorption line.

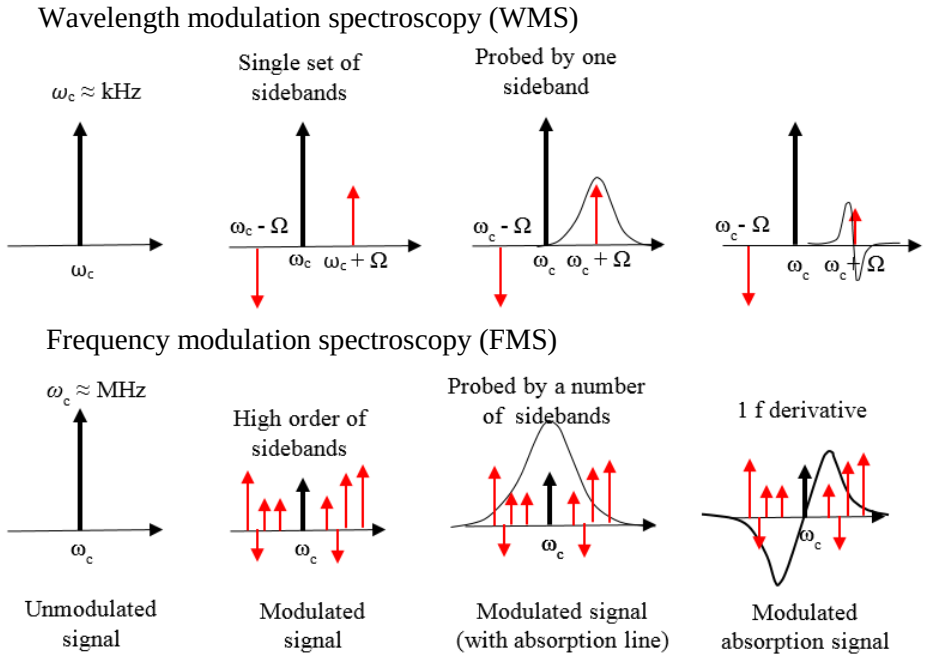

Figure 3.3: Modulation spectroscopy - Interaction of the higher and lower modulated signals with a gas absorption line, adapted from [95]**.**

For WMS, the drive current of the laser is varied at a modulation frequency ω_c, of several kilohertz, which is considerably less than the half width of the gas absorption line (typically several GHz). The resultant signal, in the absence of the absorbing line, will yield a number of sidebands at higher and lower frequencies than the centre modulation frequency. The frequencies at which the sidebands occur will depend on the set amplitude of the modulating signal, with greater amplitudes causing greater frequency deviation from the centre modulation frequency. A value called the modulation index, M, can be used to characterise the modulation and is given by the ratio of the modulation amplitude to the gas linewidth[96]. For WMS this value is typically large, i.e. M>1. The interaction of the modulated signal with the absorption feature gives harmonic components of the modulation signal which can be detected using phase sensitive electronics. A schematic of typical WMS detection signals is shown in Figure 3.4, where an additional low frequency ramped waveform allows for the full spectral line shape to be measured.

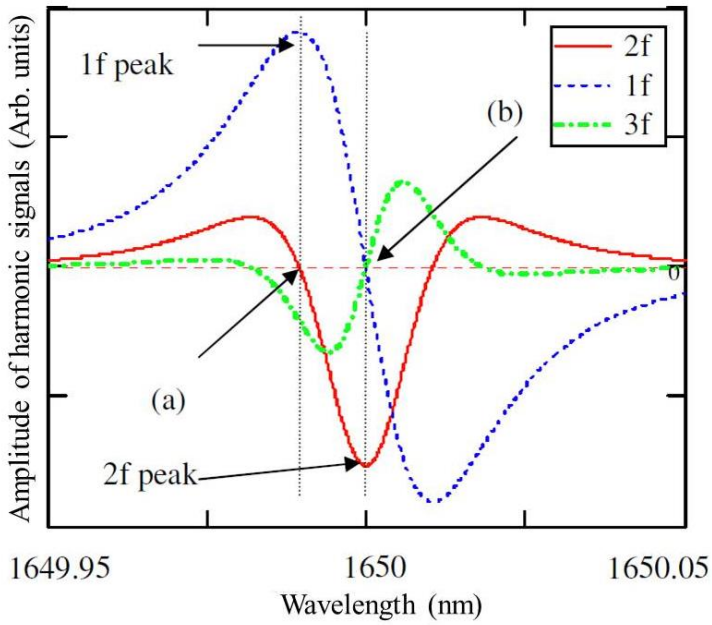

Figure 3.4: WMS harmonic components obtained when laser wavelength is scanned across the gas absorption line. The 1f signal crosses the baseline at the absorption line centre (b) and contains a DC offset due to the sloping background. The 2f signal peaks at the absorption line centre and is dependent on the gas properties. The 3f is much weaker than the 1f signal, also having a zero value at the absorption line centre. When using the 2f signal to make gas measurements the 1f and 3f signal can be used to correct for any deviations from the line centre i.e. at (a) as the resultant value will be non-zero. Taken from [97]

For gas detection, the 2f signal is often the most commonly used as it reduces the DC offset in the baseline and due to its strong dependence on the gas properties, is indicative of the lineshape of the absorption feature[98]. The 1f signal is heavily dependent on the intensity modulation[99] and carries a DC offset due to the sloping background. It can be used as a normalization tool to correct for any intensity changes, such as due to laser drift or window fouling[100], [101].

The WMS technique is popular as it is easier to implement than FMS and does not require such high speed detection electronics. Though it was originally intended to employ WMS in the system described in Chapter 5, it was later decided, for ease of signal processing, to apply a more straight forward direct spectroscopy approach while testing the ratiometric principle.

For FMS on the other hand, the drive current of the laser is varied at a modulation frequency ω_c, of several gigahertz, typically of the order of the half width of the gas absorption line[95]. The resultant signal, in the absence of the absorbing line has a set of sidebands of equal magnitude but opposite signs, as seen in Figure 3.3, which cancel each other out. In the presence of an absorption feature, one sideband interacts with the absorption feature the result being that the sidebands cancel imperfectly giving a difference signal that is proportional to the magnitude of the absorption. FMS is typically characterised by a low modulation index i.e $M<1$, where the modulation depth is small and the modulation frequency is high. The technique provides very high sensitivity as it is so far removed from the common low frequency noise sources however it is more difficult to implement and requires high speed detection. Additionally it was found that when combined with multipass cells, the optimal number of passes was lower for FMS than for WMS due to the power attenuation of the multipass cell[102]. The implication of this is that though higher sensitivity was achieved with the FMS technique, when combined with the requirement for a lower number of passes in the multipass cell, only one order of magnitude (rather than two[103]) greater sensitivity was achieved than for the WMS system with a longer pathlength.

3.2 Performance limiting factors

In order to provide quantitative gas measurements in the field, TDLS systems are calibrated in-house using known concentrations of gas to provide a calibration. As well as considering strategies for enhancing sensitivity it is also necessary to consider mitigation of the factors that limit the sensor performance. Some of the main factors include noise, drift, frequency jitter and interference fringes.

3.2.1 Noise

Noise is generally considered as random undesirable fluctuations in a signal at the output of a detection system that obscures or reduces clarity of the true signal of interest. Random error (noise) is inherent in any instrument, usually a constant value independent of the signal strength and is often the limiting factor in instrument sensitivity. As the signal strength itself can vary from strong to weak, the relative magnitude of the noise signal can become appreciable. The signal-to-noise ratio provides a useful indicator as to how much noise there is on the signal and is calculated by dividing the signal voltage or power by the rms noise voltage (or power). Examples of high and low SNR signals are shown in Figure 3.5[104]

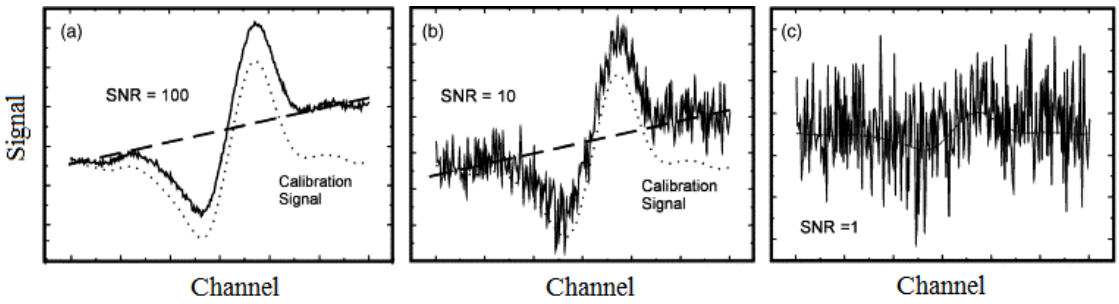

Figure 3.5: Examples of different SNR signals. (a) A signal-to-noise ratio (SNR) of 100 corresponds to a clean signal, (b) a SNR of 10 requires further signal averaging and (c) a SNR of 1 is noisy and it may not be possible to extract the signal of interest. Taken from [104]

As seen in Figure 3.5(c), with a SNR of 1 the signal is almost lost. Noise can result from frequency independent "white noise", such as thermal or shot noise or frequency dependent 1/f "flicker" noise. Noise contributions often originate from the electronics in the systems.

- Thermal (Johnson) noise (thermal agitation of electrons)
- Shot noise (rate of arrival of electrons or photons)
- Flicker noise (related to frequency of signal, often obeying a 1/f frequency dependence)

The latter noise corresponds to very low frequencies and can often contribute to drift at very low frequencies (<<1Hz).

Thermal (Johnson) noise

Thermal noise is a form of white noise and occurs due to random thermal fluctuations in stationary charge carriers, which cause a small, yet detectable, current to flow. It is present in all resistive components in the system and is independent of the quality of the material or the electrical circuit configuration. Expressing the thermal noise in terms of voltage, the root mean square (rms) voltage, V^2 for a given measurement bandwidth, Δf (Hz) is given by

$$V^2 = \sqrt{4k_B T R \Delta f} \qquad 3.1$$

where k_B is Boltzmann's constant in joules per Kelvin, T is the resistor's absolute temperature in Kelvin, and R is the resistor value in ohms (Ω). As seen in equation 3.1 the magnitude of the noise is dependent on the temperature, resistance and bandwidth. In theory white noise is infinite in bandwidth, having an even distribution from DC to infinity. However in practise, electronic systems are bandwidth-limited and so thermal noise energy can be reduced by reducing the bandwidth. This can be achieved by using bandpass filters, which has been done for the experimental work discussed in Chapter 6. Other ways to reduce the noise include lowering the electrical resistance or the temperature of instrument components.

Shot noise

The flow of current is not continuous in a circuit, rather is made up of the movement of discrete charges. Shot noise, on an electrical current is also a type of white noise and is caused by the statistical variability in the arrival time of charge carriers. The root mean square current fluctuations can be described as

$$\sigma_i = \sqrt{2qI_C \Delta\omega} \qquad 3.2$$

Where q is the elementary charge of an electron, I_C is the DC current and $\Delta\omega$ is the bandwidth. As seen in equation 3.2, the magnitude of the fluctuation increases with increasing current. This, as with thermal noise, is independent of frequency but for the same reasons as thermal noise can be minimised by reducing the bandwidth of the component. Due to the charge of an electron being so small and the number of electrons being so large, the shot noise is often insignificant with thermal and flicker noise being the dominant sources.

Flicker noise (1/f noise)

Flicker noise is often termed 1/f noise as it exhibits an inverse frequency power density curve. Unlike shot noise, which is attributed to the random motion of the charge over a barrier, flicker noise often occurs when the current is controlled at a localised barrier e.g. a resistance fluctuation. It depends greatly on materials used and device shape e.g. metallic resistors have 10-fold less flicker noise than carbon-based resistors.

3.2.2 Frequency jitter

Fluctuations in the laser current translate in frequency jitter, which can cause sampling errors, as well as spectrum broadening due to averaging. A fluctuation in the laser current of only a few mA can cause laser wavelength fluctuations of MHz[105]. Fluctuations can occur as a result of internal effects within the laser, such as mode-hop or spontaneous emission, particularly in the case of pulse build-up in pulsed lasers. In this case, the introduction of a substantial time delay i.e. placing a length of optical fibre between the source and detector can reduce the magnitude of the laser noise by moving the desired signal to a region where the laser pulse build-up effects are negligible. The laser noise could also be reduced by implementing a phase locked loop system, which suppresses the jitter for the measured signal by comparison to a reference clock[106], [107]. An alternative method is to apply digital random dithering, which breaks up the unwanted pattern and spreads the fluctuation across a number of frequencies. This does have the drawback of increasing the noise floor; incorporating noise shaping into the system can help to alleviate this effect[108], [109]

Other external influences include thermal changes, mechanical vibrations, pick-up from external sources, such as electric power lines transmission (e.g. 50Hz typically) or cross-talk from another part of the circuit. Providing sufficient shielding as well as

grounding the device can reduce interference effects resulting from electromagnetic fields, common impedance, or other forms of interference coupling[110]. In the case where electronic interference persists it may be possible to apply a band pass filter if the desired signal does not occur in the same frequency region.

Assuming that optical interference fringes (see Section 3.2.4) have been reduced to a negligible level it is expected that the system will be limited by a combination of the noise sources as described in Section 3.2.1, with the contribution of each dependent on the frequency region in which the measurement is made.

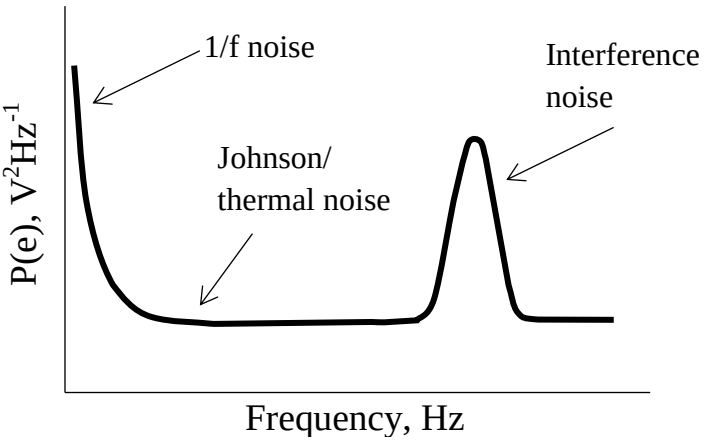

Figure 3.6: Noise power spectrum(NPS). A plot of the mean-square noise per unit frequency interval, P(e) in V^2Hz^{-1}, vs. the frequency in Hz. As seen, for 1/f noise, P(e)decreases with increasing frequency, thermal/Johnson noise is independent of frequency and interference is finite and dependent on specific frequencies

3.2.3 Drift

As seen in the previous section, faster processes like laser current noise and vibrations tend to contribute jitter and add to the linewidth, while slower timescale processes such as temperature and air pressure changes cause drifts. This slow drift can cause the centre emission wavelength to change relative to its calibration.

The solution to overcome frequency instability is to lock the laser to a frequency reference. This could be a resonant cavity where a feedback system provides adjustment if the laser deviates from resonance[111]. Alternatively the laser centre frequency could be locked to the gas line where a reference cell with a high concentration of the gas of interest is used with a feedback system to adjust the frequency accordingly[112].

3.2.4 Optical interference fringes

Though the use of narrow line width lasers in TDLS applications provides very good selectivity to the gas by interrogating single absorption lines, their long coherence lengths can result in a system that is more susceptible to optical interference. Optical interference fringes occur as a result of Fabry-Perot etalons being created between reflecting surfaces such as mirrors, detector windows or components in the gas cell. In multipass cells for example, a specular beam is being folded multiple times between two mirrors with the requirement that there is no beam overlap. Depending on the number of passes that are present (often >100), this makes the alignment of the cell difficult and also results in tight tolerance towards misalignment. The fringe spacing, F, is related to the distance, L_{SP}, between these reflecting surfaces by

$$F = \frac{1}{2nL_{SP}} \tag{3.3}$$

where n is the refractive index of the medium, usually air. If the fringe spacing is of the order of the molecular line width of the target gas, it could be mistaken for a gas absorption line giving a false positive for the gas. Alternatively the fringing could distort or obscure the gas absorption line, and if appreciable enough, could become the limiting factor in the sensitivity of the system. As the spacing of the fringes can change with mechanical and thermal instability it is not possible to simply subtract a reference signal i.e. taken with no gas present, as a means of removing any etalons. Strategies for reducing optical interference effects include the use of anti-reflection coatings on the reflective surfaces or deliberate steering off of the beam to reduce the parallel configuration. This does however reduce the power output. Another approach, similar to that in Section 3.2.2, is to apply a dither to the laser diode[113], which causes the laser to tune over a number of fringe periods. When the sweep of the wavelength tuning matches an integer multiple of the fringe spacing, the integrated signal goes to zero, thus removing the fringe signal. This will also reduce the magnitude of the absorption signal. Another option is to remove the interference using post-detection filtering[114]. For example, the use of high pass filters can be used where the modulation frequency is high to remove the lower frequency noise and interference fringes. Both techniques will not work if the fringe spacing is on the same frequency order as the target gas absorption line.

In this body of research the periodicity associated with specular beam folding is eliminated through the use of an integrating sphere which provides diffuse reflections. This will be discussed in more detail in Chapter 4.

Another source of error can arise due to polarisation mismatches, e.g. polarisation states may not be the same between components or a wavelength dependency may affect the system performance if outwith desired wavelength range. For example, polarisation maintaining fibre is a speciality fibre with a strong built-in birefringence i.e. creates a double refraction, which results in two principal transmission axes, the fast and slow axes. This can be induced in a material by applying mechanical stress, which forces the lightwave to follow a linearily polarized path. If two polarisation maintaining components are connected such that their transmission axes are not aligned, different proportions of light will couple into each axes, the extent of which will depend on the angle of the rotation of the two components relative to each other. This will reduce the intensity output along the desired polarisation state[115]. If the light is being modulated different polarisation states will have different bias points (phase difference applied by a DC bias voltage) and so the output modulation signal may become distorted with additional waveform structures[116]. Ways to reduce these effects include precise alignment of the polarisation axes and use of fibre with small polarisation mode dispersion[115].

3.2.5 Cross interference

It is important to be aware of potential interfering gases when targeting a specific gas absorption line. One molecule in particular that consistently proves problematic is water. Water has a number of broad absorption bands across the IR spectrum. The wavelength regions that have been targeted for CH_4 and CO_2 for this research are shown in Figure 3.7.

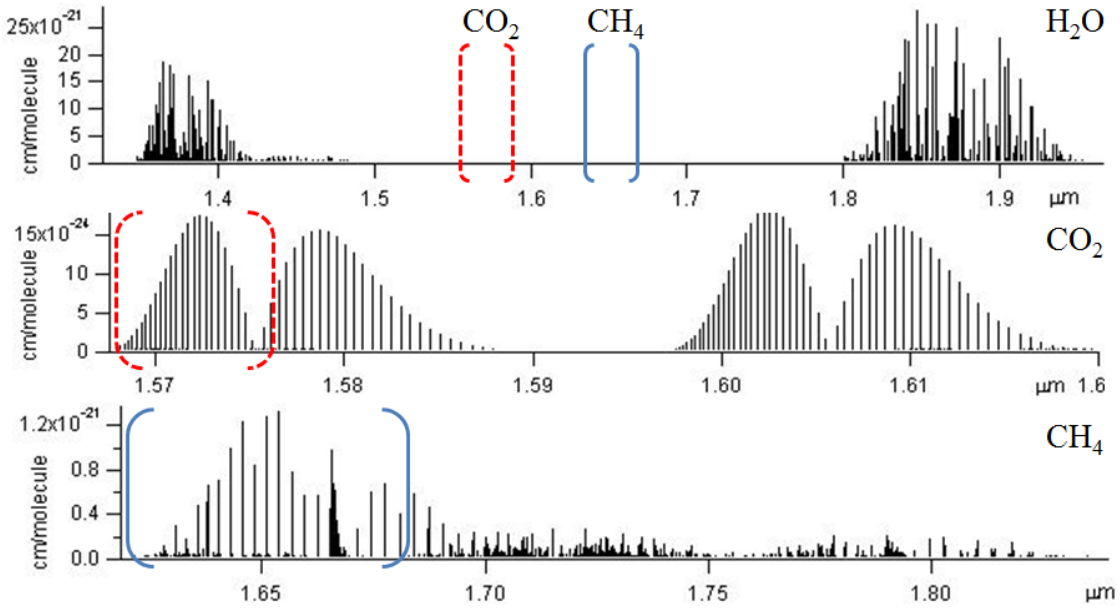

Figure 3.7: Wavelength regions targeted for CH_4 and CO_2 that avoid water absorption line overlap. Taken from Hitran[51]

If it is not possible to select a wavelength region with no interferents, strategies to minimise the effects of interferents include for example, in the case of potential water cross-interference, heating certain optical parts of the system to reduce condensation and thus presence of water absorption bands [117]. Another option is to include a fitting algorithm for the interfering species, e.g. H_2O and O_2 also and then apply a subtraction to the overall measurement[118]

3.3 Summary

As seen in this chapter, the factors that can affect sensor performance are varied and dependent on the particular situation of the sensor. For example the use of a sensitivity enhancement strategy such as implementation of a multipass cells can bring with it problems of its own, such as performance limiting etalon interference. A number of solutions, both in terms of hardware and software have been developed to overcome these factors. This includes antireflective coated windows in multipass cells to overcome fringing, or post-detection subtraction if the fringe spacing is known and stable. A number of these strategies have been implemented in this body of research as will be outlined in Chapters 5 and 6.

For this body of research, when considering implementation as a gas sensor, some of the specific performance targets include:

- Limit of detection down to low ppm i.e. 1-10s of ppm: It was found that with a sphere of 5cm diameter and port fraction of 0.0077, an effective pathlength of 1m was achieved. With this, detection of methane was achievable down to approximately 60ppm. The technique employed in this case was direct absorption spectroscopy and so it is expected that much lower concentrations could be achieved by applying modulation techniques, see section 3.1.2, and minimising the port fraction further to increase the effective pathlength.

  It is thought that contamination would represent the greatest limiting factor as a small amount could reduce the detection limit greatly. In the case where contamination does not occur, it is thought that electronic interference may represent the limiting factor ultimately. This can be alleviated somewhat using bandpass filters, as discussed in section 3.2.2.
- Selectivity: At the wavelength region of 1650nm, absorption lines of typical cross-interferents, such as water, are not present and so this technique is very selective to methane. If the technique was to be used for other gases, e.g. HF around 1200nm, it would be necessary to consider the potential interferents in that wavelength region and their contribution to the measurement,
- Response time of no longer than 30/40 sec: Active pumping rather than passive diffusion is required when using the integrating sphere to ensure homogeneous diffusion of gas. It was found that with a flow rate of 1 litre per minute, a homogenous sample was achieved after approximately 20 seconds. However one of the drawbacks of using a multipass cell is that, though sensitivity is increased through increased pathlength, the overall throughput is lower due to the less than 100% reflectivity of the cell. Additionally the diffuse reflections generated in the sphere result in a signal with a noisier baseline than typical multipass cells and so it may be necessary to increase the averaging time (particularly in the case of lower gas concentrations). This will increase the response time.
- Accuracy of ±5%: As this setup utilises a tunable diode laser, it is envisaged that this system should aim to achieve industry standards for TDL systems of ±5%.

The potential for slow drift, i.e. due to ambient conditions such as temperature or pressure has not been tested for the setups described in this research. It is proposed that wavelength drift in the laser could be corrected for by locking to the gas line using an in-built miniature reference gas cell with a high concentration of the sample.

- Easy to operate: One of the advantages of the sphere is that as it generates diffuse reflections regardless of angle of incidence, alignment tolerances are eased. Additionally the overlapping of beams eliminates generation of periodic standing waves, a phenomenon that can occur in typical multipass cells. This confers a robustness to the integrating sphere, for example in scenarios where vibrations may be an issue e.g. on aircraft. The material itself, a PTFE based material, can be cleaned with water or even light sanding and so do not require technical operators to clean and realign the cell.

4

Integrating sphere theory and applications

"Little information appears to have been published about the diffusing power of unpolished surfaces. Its ability to increase the illumination of rooms and open spaces, although well known, does not appear to be appreciated to the extent that its importance deserves; and a few numerical determinations of the coefficients of reflexion, absorption, and transmission of diffusing surfaces may prove of interest" – W.E. Sumpner[119] *(1892)*

W.E. Sumpner, in 1892, first described integrating sphere theory[119] when he began to derive quantitative measurements for the coefficients mentioned in the quote above. Though the motivation for his work was to increase illumination in rooms through the diffusion of light, it formed the foundation of integrating sphere theory in the field of photometry. This chapter aims to provide the reader with a good grasp of the theory surrounding the development of the integrating sphere, both in its traditional capacity as a tool for light flux calibration and in later years, as an optical cell for making quantitative gas measurements. The chapter begins with a general history of how the integrating sphere became the commercial component that it is today. The mathematical theory pertaining to integrating spheres, due to the many applications, is extensive and so this chapter introduces only the general equations that are pertinent to this research. Following this, the motivations for use of this cavity as a gas cell are introduced, in the form of a review of the literature, including the potential challenges for this application.

4.1 The development of the integrating sphere

At the turn of the 20th century, R. Ulbricht[120], after whom integrating spheres are often called "Ulbricht spheres", built the first integrating sphere. The working principle of an integrating sphere is that light incident on the sphere is scattered by the inner wall giving multiple diffuse reflections, which provides a uniform power distribution at

every point in the sphere. By exploiting this principle, Ulbricht had created a device capable of measuring accurately the total luminous flux of different light sources. This is achieved by placing the light source to be calibrated in the centre of the integrating sphere and measuring the total spectral output from the source. This reading is then compared to a similar reading obtained from a calibrated light source of known luminous flux. This, as noted in "Popular Science Monthly" in 1916[121], see Figure 4.1, allowed flux measurements to be made in under five minutes as opposed to half an hour with previous methods, and in fact is still widely used for manufacturing quality control in the light industry today[122], [123].

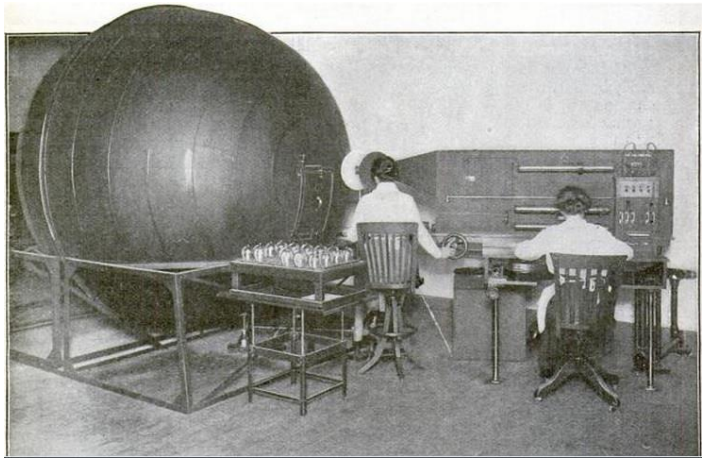

Figure 4.1: A 100 inch sphere photometer, "suggestive of the rind of some Brobdingnagian watermelon"; the Ulbricht sphere as introduced in 1916 to the readers of "Popular Science Monthly"[121]

In addition to this application, in 1916 A.H. Taylor (National Bureau of Standards), following from W.E. Sumpner, developed methods for measuring diffuse reflectance factors for reflective surfaces[124]. Integrating sphere technology took a leap forward in 1931 when A. Hardy at Massachusetts Institute of Technology (MIT) developed the first commercial spectrophotometer[125]. In this particular application, diffusion of light was achieved by coating the sphere wall with a magnesium oxide (MgO) based coating, created by "smoking" MgO shavings on a white paint layer. Indeed prior to the 1960s, most designs utilised this coating. However it was difficult to achieve layers that were reproducible to greater than ±1% accuracy in thickness[126], [127] and so the International Commission of Light (CIE), in 1969, recommended moving away from this as the primary reflectance standard. The more highly reflective barium sulfate

($BaSO_4$) coating, "Eastman 6080" was created by F. Grum and T.E. Wightman[128] of Eastman Kodak Company in the late 1960s and has become the basis for most commercial barium sulphate coatings. $BaSO_4$ coatings, are highly reflective (>98% reflective from 250-1300nm), diffuse and non-toxic[129]. They are relatively easy to apply and adhere well to most metal and plastic surfaces as well as being effective over a relatively large wavelength range (250-1800nm). However the coating is fragile and easily damaged by water due to the use of a water soluble binder during manufacture. Furthermore it can become discoloured and less reflective when exposed to humidity. One solution to overcome some of these issues is the use of a highly reflective material as opposed to a coating, namely a polytetrafluoroethylene (PTFE) based material[130]. Manufacture of this material utilises a sintering process where PFTE powder is packed against silicon vacuum grease to a constant density of approximately 1g cm^{-1}. This material is highly reflective (>98%) over a large wavelength range (250-2500nm), stable in temperatures up to 250°C and in humid conditions[131]. However it is difficult to machine, and can be quite heavy. For this project two PTFE based integrating spheres have been used, with trade names Spectralon™ and Zenith™. Two scanning electron micrograph (SEM) images in Figure 4.2 show the surface topography of barium sulphate power and Spectralon™, highlighting the difference between the powder and solid material.

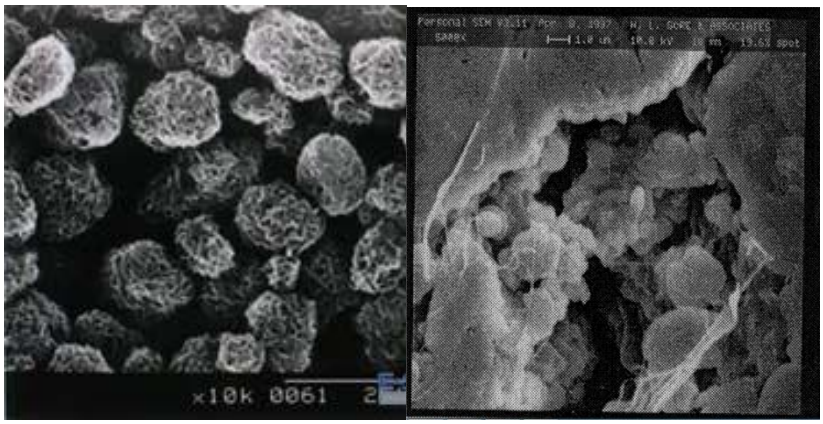

Figure 4.2: A scanning electron micrograph of (a) barium sulfate powder(x 10k mag) and (b) spectralon(x5k mag). Taken from [132] ***and*** [133]

Typical multipass mirrors often contain highly reflective coatings that can become degraded quickly by water absorptions, contamination and abrasion and so cleaning of these mirrors requires extra care, not to mention realignment when replaced in the cell.

PTFE based cells on the other hand can be rinsed with water, wiped and in some cases, higher reflectivity is restored by sanding with an appropriate grit paper[134].

The advantages and limitations of the two different materials are summarised in Table 4.1 below.

Table 4.1: Summary of advantages(+) and disadvantages (-) of reflective materials for integrating spheres.

Type	Notes
Spray-on coating	Often $BaSO_4$ based. (100°C thermal limit) **(+)** Easy to apply, highly reflective and diffuse over a large wavelength range **(-)** Fragile, can be degraded by water and humidity.
Sintered coating	Usually PTFE based (350°C thermal limit) **(+)** Highly reflective and diffuse over a large wavelength range, very stable in humidity and temperatures up to 250°C **(-)** Tedious to machine, heavy, more expensive than spray-on coatings.

4.2 Integrating sphere mathematical theory

As illustrated in Figure 1.4 in Chapter 1, the distribution of light in the integrating sphere comprises multiple diffuse reflections due to its optically rough inner surface. This surface is an ideal diffuse reflector, according to Lamberts cosine law. Lamberts cosine law states that the radiant intensity observed from a small surface area in a particular direction is proportional to the cosine of the angle between that direction and the surface normal, as seen in Figure 4.3

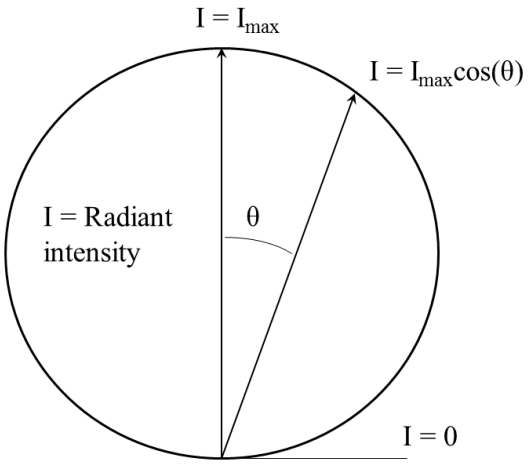

Figure 4.3: A Lambertian surface where the observed radiant intensity is directly proportional to the cosine of the angle between the direction of the incident light and the surface normal.

The radiance from a portion of the surface is the same when viewed from any angle due to the correlation between emitted power and apparent area observed. This property facilitates uniform diffusion of light in an integrating sphere.

As described in general integrating sphere theory, the light emanating from a diffuse surface can be written in terms of radiance, B_s[135], (flux density per unit solid angle)

$$B_s = \frac{\Phi_i \rho}{\Omega A_s} \qquad 4.1$$

where Φ_i is the input flux, ρ is the reflectance, A_s is the total area of the sphere inner wall and Ω is the total projected solid angle from the surface.

When considering the diffuse surface of an integrating sphere, the radiance equation must account for the losses due to presence of port openings, i.e. source input and detector output ports. The losses are accounted for by calculating the fractional area of surface that is lost to port openings, relative to the total area A_s, and is termed the port fraction, *f*

$$f = \frac{A_i + A_e}{A_s} \qquad 4.2$$

where A_i is the area of the input port, A_e is the area of the exit port. If there are additional ports, such as gas ports, the port fraction, *f*, is calculated from the sum of

these port areas. Combining the reflectance, ρ, and port fraction, f, gives a unitless quantity termed the sphere multiplier, M which accounts for the increase in radiance due to multiple reflections

$$M = \frac{\rho}{1-\rho(1-f)} \tag{4.3}$$

The radiance of an integrating sphere can then be expressed as a function of sphere diameter, reflectance, and port fraction

$$B_s = \frac{\Phi_i}{\pi A_s} * \frac{\rho}{1-\rho(1-f)} \tag{4.4}$$

It can be seen from Equation 4.4 that the radiance decreases as sphere diameter increases and so it could be assumed that smaller spheres are preferable as they will produce higher radiance. For application to gas sensing where higher sensitivity is gained through increased interaction of light with the gas sample, a larger sphere is in fact preferable to facilitate longer path lengths. When optimising the sphere design, the number and size of port openings required as well as which coating/material gives the required reflectivity must also be considered. Port opening sizes are designed such that the area consumed by openings is minimised to maintain diffusion performance whilst still facilitating use of the desired sources, detectors etc.

For a detector with active area, A_d, the total flux incident on the detector is

$$\Phi_d = B_s A_d \Omega \tag{4.5}$$

where B_s is the radiance as described in equation 4.1 and Ω is the projected solid angle, generally approximated as

$$\Omega = \pi \sin^2 \theta \tag{4.6}$$

where θ is the angle subtended from the exit pupil of the system as seen in Figure 4.4

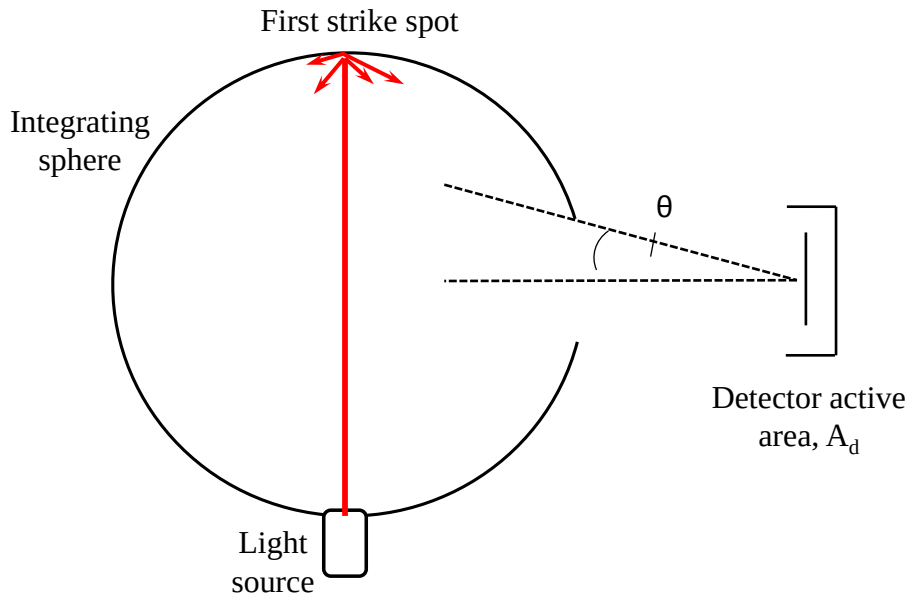

Figure 4.4: The projected solid angle Ω is derived from the angle θ i.e. the angle subtended from the detector active area. The point at which the focused incident beam first encounters the sphere wall is termed the first strike spot

The portion of the sphere surface directly irradiated by the incident flux is termed the first strike spot, as seen in Figure 4.4. It is important that the detector field of view does not encounter the first reflections from this first strike spot or else the measurement will include a portion of direct irradiation which will dominate the measured radiance. This can be achieved by using a baffle coated with the same material as the wall or else recessing the detector position from the sphere.

The equations so far have assumed steady state conditions, where the light levels in the sphere are constant so that transient effects are negligible. For rapidly varying light signals, i.e. due to rapid modulation or use of a pulsed light source the output signal has an impulse response of the form[135]

$$h(t) \propto e^{\frac{-t}{\tau}} \qquad 4.7$$

Where t is the time elapsed, τ is the decay constant calculated as[135]

$$\tau = -\frac{2}{3}\frac{D_s}{c}\frac{1}{\ln \rho} \qquad 4.8$$

where $\bar{\rho}$ is the average wall reflectance, c is the free space velocity of light, and D_s is the diameter of the sphere. As seen in equation 4.7, the integrating sphere exhibits an exponential decay, in a similar manner to cavity ring down spectroscopy as described in section 2.3.4.

The theory described so far comes from the widely accepted integrating sphere theory derived from extensive experimental work and manufacturer tests. The equations account for factors affecting the light distribution such as the sphere wall reflectivity and port openings however the presence of an absorbing species is not considered. In order to adapt integrating spheres for gas sensing applications, it was necessary to derive new mathematical equations that allowed for quantification of an absorbing species. The measured gas absorption is proportional to the pathlength and so an expression for the effective pathlength was also considered. The research to date by a number of groups is discussed in more detail in the next section but some equations of note have been included here as they were used for this research.

For steady state conditions, Tranchart *et. al*.[24] expressed the fractional absorption of a substance in an integrating sphere as

$$\frac{\Phi_e(0)-\Phi_e(\alpha)}{\Phi_e(0)} = \frac{\left[\alpha L_{sp}\right]}{(1-\rho\left[1-\alpha L_{sp}\right](1-f))} \qquad 4.9$$

where, as before, ρ is the sphere wall reflectance, f is the port fraction and α is the gas absorption. L_{sp} corresponds to the average distance travelled between successive reflections at the cavity wall i.e. for a single pass. For an integrating sphere this has been shown to be 2D/3[136]. Thus the effective pathlength L_{eff} can be calculated using a multiplication as follows

$$L_{eff} = \frac{2}{3}DM \qquad 4.10$$

where M is the sphere multiplier as defined before and D is the diameter of the sphere. For low or zero absorbance α and where the apertures are very small (f<<1), the effective pathlength L_{eff}, is of the order

$$L_{eff} = \frac{2}{3}\frac{D}{(1-\rho)} \qquad 4.11$$

4.3 Integrating sphere based gas cell: Motivations

An observation put forward by Elterman[26], in 1967, highlighted a significant advantage of using an integrating sphere as a tool for absorption measurements. He stated that if the sample to be measured is in an isotropic homogenous field, that the absorbed radiant power should be independent of scattering effects. This, as well the potential for greater sensitivity through increased sample – light interaction in a small volume, provided the main motivations for the research that has been carried out over the last forty years. The following section introduces some of the ideas of this research, categorised by the two advantages just mentioned and in terms of their theoretical and experimental approaches, as both have progressed at different rates and with different outcomes. All bodies of research are then summarised chronologically in a table format in Section 4.4 to demonstrate how the research has developed over the years.

4.3.1 Immunity to scattering effects

As mentioned in the previous section, Elterman[26] highlighted the use of an integrating cavity as a tool to alleviate scattering effects, often caused by components within the sample itself or reflections at the sample surface. Here the absorption coefficient of the sample α was determined from the ratio of the irradiances at the surface of the integrating cavity with and without the sample present, as in Equation 4.12

$$\alpha = \frac{A_s(1-\rho)(\frac{H_0}{H_\alpha}-1)}{4n^2V_c} \qquad 4.12$$

where A_s is the surface area of the sphere, ρ is the sphere wall reflectance, H_0 is the irradiance of the empty sphere, H_α is the irradiance with absorbing species present, n is the refractive index of the species and V_C is the volume of the sphere. The only requirement was that the index of refraction of the sample must be known. The cited advantages of this approach were that the measurement would be independent of the scattering within the material sample, the reflectivity of the material surface, and the geometry of the sample. To confirm this experimentally a glass sample was placed in an integrating cube followed by an integrating sphere and the absorption coefficient was

determined using Equation 4.12 for both cases. The results were also compared with a direct path transmittance measurement and found to agree to within ±10% of each other.

In subsequent years there has been much interest in integrating sphere application to the water industry, where turbidity in samples often proves challenging for typical transmission type measurements. Fecht and Johnson[137] presented a setup where absorption measurements were made by having an unconstrained falling stream of the water sample flow through the centre of the integrating sphere. This served two purposes, reducing the scattering effects of particulates within the water sample as expected, but also facilitated measurements that did not require contact with the sample cell itself, which eliminated the potential for chemical or biological deposit build-up on the windows. An expression for the voltage output, V was derived that accounted for the light which encountered the sample, $G_\alpha e^{-\alpha L}$ and that which did not ($1-G_\alpha$).

$$V = K(1 - G_\alpha + G_\alpha e^{-\alpha L}) \qquad 4.13$$

where K is the detector sensitivity, G_α is a splitting fraction (due to particulates), α is the absorption coefficient and L is the pathlength. The system was tested experimentally by introducing varying concentrations of a cobalt chloride solution of known absorbance with scattering silica particles into the falling stream and measuring the resultant absorbance for each when in the presence of a scattering medium. The measurement tolerated well the presence of scattering particles (14% error with 15ml of scattering particle addition vs. 450% using a commercial spectrometer). Instead the challenges to be overcome in this setup included ensuring a regular water flow in the stream and maintaining temperature control of the LED source used.

Other approaches looked at completely filling the integrating cavity with the sample. One embodiment of note is that of the integrating cavity absorption meter (ICAM), created by Fry *et. al*.[138], [139] as seen in Figure 4.5

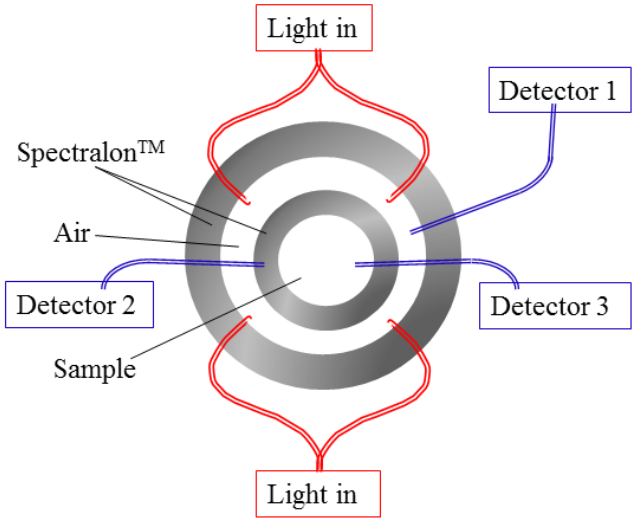

Figure 4.5: Integrating cavity absorption meter (ICAM); the "sphere-within-a-sphere" setup achieves isotropic illumination of the incoming light source for absorption measurements. The irradiances are measured for the air filled cavity (detector 1), the Spectralon™ inner sphere (detector 2) and the sample filled inner cavity (detector 3), adapted from [139]

Here, rather than having a single anisotropic point source inputted into a sphere, a "sphere within a sphere" configuration was created, with the outer sphere providing diffusion of the input beam. As a result the light that entered the inner sphere, i.e. the sample cell, was isotropically illuminated and thus did not suffer any geometrically related scattering. The setup was described mathematically by taking an energy conservation approach and forming irradiance relationships between the inner cavity and inner sphere wall. An expression for the absorption measurement α was derived as follows.

$$\alpha = \frac{1}{4V_c}\left(C_1 A_s (1-\rho)\frac{H_W}{H_\alpha} - A_s(1-\rho) - A_F\right) \qquad 4.14$$

where V_c is the volume of the inner sphere, A_s is the area of the inner sphere and C_1 is a proportionality constant derived from comparison of the radiance of the inner and outer spheres. H_w corresponds to the irradiance within the integrating cavity wall, H_α is the irradiance of the inner sphere with the absorbing species present, A_F is the area of the aperture of the fibre optic output to the detector and ρ is the sphere wall reflectance. The setup was tested experimentally where a 8.7cm diameter Spectralon™ sphere was used giving an effective pathlength of, it was predicted, up to 10m. Absorption measurements

of water at 0.63μm made in the presence of a high concentration of scattering material, i.e. 2.3g/L of quartz powder, were found to have an error of only ±8% in absorption.

Other turbid samples that have been measured include lubricant oil[140], olive oil[141] and whisky[142]; for example degradation of the lubricant oil could be determined based on the absorption changes due to increased acidification with degradation. In these cases the sample was contained within a vial so as not to contaminate the sphere surface.

Another interesting exploitation of the cavity's uniform scattering property was to improve the performance of another component. Venkatesh *et. al*[143] aimed to achieve well characterised spatial intensity distribution for a tunable diode laser source, providing an alternative to blackbody sources used for calibration of IR sensor systems. A light source at 5μm was coupled into a 3.8cm diameter gold coated integrating sphere and the intensity profile for a range of detector translations was recorded. The result was a smooth intensity profile with a Gaussian distribution. The output intensity I of the sphere was found to obey the relation

$$I = \frac{\Phi_i f_{exit}}{\Omega}\left(\frac{\rho}{1-\rho}\right) \qquad 4.15$$

where Φ_i is the radiant flux incident on the cell, f_{exit} is the port fraction related to the exit port only, Ω is the solid angle and ρ is the sphere wall reflectance. An effective pathlength, L_{sphere} of 62.2cm was determined for the sphere by comparison of absorbance measurements of carbon monoxide with a cell of known length, L_{cell}

$$L_{sphere} = \frac{A_{sphere}}{A_{cell}} L_{cell} \qquad 4.16$$

where A_{sphere} and A_{cell} correspond to the absorbance measurements for the sphere and cell respectively. A few years later Berger *et. al*.[144] found another application that exploited the diffusive nature of the integrating sphere, namely in matrix isolation spectroscopy, a technique in which the species of interest is embedded in an unreactive matrix for long enough to facilitate a spectroscopic measurement to be made. Here the integrating sphere wall, diameter 1.3cm, was coated with a thin film of a substrate

which facilitated the formation of a gas matrix between the "host" gas, CO_2 and the sample of interest (N_2O), using a NdYag laser at 8.57μm. The sensitivity towards weakly absorbing samples was enhanced as the sample was exposed to more light due to the multiple reflections. They found however that the presence of the matrix caused the measurements to deviate from the standard Beer Lambert relations and so derived an expression for the output flux in the presence of the matrix, $\Phi_e(m)$ that corrected for this deviation by introduction of a transmittance factor T

$$\Phi_e(m) = \frac{\Phi_i \rho A_d T}{[1-(1-f)\rho T]} \qquad 4.17$$

where Φ_i is the radiant flux incident on the cell, ρ is the sphere wall reflectance, A_d is the detector active area and f is the port fraction. More recently Lassen *et. al*. [145] have used the multipass nature of the integrating sphere to enhance the photoacoustic (PA) signal and thus sensitivity of a PA spectrometer. Here a 5.08cm diameter PTFE sphere was coupled with a 90mm organ tube pipe which further enhanced the signal through acoustic resonance.

Building on the idea of an ICAM, a number of groups proposed a point source ICAM, (PSICAM)[146], [147] as it was felt that the sphere within a sphere construction of the ICAM added an additional layer of complexity. Here the point source was placed in the centre of the sphere. One investigation[147] into the PSICAM took the Monte Carlo approach of repeat sampling to model the light field for cavities filled with a sample that both scatters and absorbs. The aim was to investigate to what extent an integrating cavity could maintain performance in terms of presence of scattering particles, varying concentrations of sample and sphere size. It was found that scattering effects were largely insignificant when making oceanic water measurements i.e. a scattering coefficient of $100m^{-1}$ gave a 0.35% error on the measurement. It should be noted that thecattering coefficient corresponds to the fractional decrease in intensity of the beam per unit distance traversed as result of from scattering (rather than absorption). It was suggested that uncertainties from factors such as varying absorbance and scattering could be reduced by deriving the sphere wall reflectivity using two non-scattering samples of known absorption coefficient and creating an expression as follows.

$$\rho = \frac{T_{AB}\exp(-\alpha_B r) - \exp(-\alpha_A r)}{T_{AB}\exp(-\alpha_B r)P_s(\alpha_A r) - \exp(-\alpha_A r)P_s(\alpha_B r)} \qquad 4.18$$

where T_{AB} is the ratio of the irradiance of the sphere when filled with two non scattering samples, A and B, with known absorption coefficients respectively. r is the radius of the sphere (m) and P_S is the probablility that a photon will return to the wall. One potential drawback of the scattering nature of the sphere was that the detection could become limited by optical interference as a result of laser feedback due to the diffusive nature of the light[148].

On the note of industrial application, the research into the use of an ICAM demonstrated the viability of using an integrating sphere for this purpose. Motivated by this work, as well as a patent[149], a version of the ICAM has been commercialised by Hobi labs[150] and deployed as a means of providing further understanding of the characteristics of sea water.

4.3.2 Enhanced sensitivity through increased sample-light interaction

Achieving increased sample-light interaction, potentially without the stringent alignment and unwanted etalons so often associated with the multipass cell is an inviting prospect for absorption spectroscopy applications. When first proposed, there was no existing integrating sphere theory to account for an additional absorbing component in the sphere. The absorption theory itself did not consider a multiple beam path approach; for example, the Beer Lambert law, as introduced in Section 2.2.3 assumes a single path. A major focus of the research was to derive an equivalent pathlength that correctly accounted for the propagation of light in the cavity both in the presence and absence of the absorbing sample.

Abdullin and Lebedev[151] stated that for low concentrations of the sample, the pathlength could be derived from the integrating cavity parameters, namely the cavity wall reflectivity, port fraction and cavity dimensions. They concluded that this was so, as the sphere surface would contribute much greater losses in radiant flux (from the input flux) than absorption by the sample. Thus an expression for the flux, $\Phi_e(\alpha)$, in the presence of an absorbing sample could be formed as

$$\Phi_e(\alpha) = \Phi_e(0)(\frac{1}{1+\varepsilon CL}) \qquad 4.19$$

where $\Phi_e(0)$ is the radiant flux transmitted through the sphere in the absence of an absorbing species, C is the concentration of the sample, and ε is the specific absorptivity of the sample. $L= r/3Abs_w$. Abs_w is a value that relates to the fraction of absorptance of radiation by the wall and the fraction of radiation flux at each given unit area of the sphere wall. In this way the derivation of L relied only on the intrinsic parameters of the sphere itself. A practical experiment using NH_3 to calibrate, gave an effective pathlength of 430±25cm for a 10cm diameter copper sphere.

Tranchart *et. al.*[24] it is thought were the first to employ an integrating sphere for gas absorption measurements. Here they provided a derivation relating the Beer Lambert law to the diffusion properties of the integrating sphere. The fractional absorption was shown to be

$$\frac{\Phi_e(0)-\Phi_e(\alpha)}{\Phi_e(0)} = \frac{\alpha L}{[1-\rho(1-\alpha L)(1-f)]} \qquad 4.20$$

where $\Phi_e(0)$ is the radiant flux transmitted through the sphere in the absence of an absorbing species, transmitted radiant flux $\Phi_e(\alpha)$, in the presence of an absorbing sample, f is the port fraction, and α is the absorption coefficient. L in this case was arrived at as follows. In the case of weak absorptions, where it was assumed that absorption of radiation by the sample would be negligible, it was found that the average single pass, L_{SP} through the sphere was equal to 2D/3. The effective pathlength was then a multiple of this; in the case of weakly absorbing samples and small port fraction the multiple corresponded to 1/(1-ρ) as listed in section 4.2. This conclusion did prompt comment from Fry *et. al.*[152] as to its accuracy as they stated that this pathlength expression did not include a parameter to account for the effect of gas concentration on the effective pathlength, i.e. that the optical pathlength decreases with increasing concentration of gas.

Javorfi *et. al.*[153] attempted to reconcile the measured "apparent absorbance" to that of the actual absorbance measurement. They did this experimentally by measuring the absorbance for varying concentrations of the dye, rose Bengal, using both the ICAM and a commercial spectrometer. The measurements from the ICAM i.e. the "apparent

absorbance", A', were superposed onto the commercial spectrophotometric measurements providing a fitting function so that for future measurements the actual absorbance, A could be calculated

$$A = \frac{1}{q_1}\left[\left(A'\right)^{\gamma} - 1\right] \qquad 4.21$$

$$\gamma = \frac{\log e}{q_0} \qquad 4.22$$

where q_1 and q_0 were fitting parameters and appeared to correspond to the effective pathlength and sphere wall reflectivity respectively. To confirm that this function was standard to this integrating sphere-detector pairing, the fitting function was applied to a repeat experiment where malachite green dye at similar varying concentrations was used. The result was that, with normalisation, the spectrum fitted well with the measurements obtained from the commercial spectrometer. However, this approach it was noted only corrected for differences due to the intrinsic nature of how the sphere operates (and not the effect of absorbing samples on pathlength) and so it was recommended that it should only be used for weakly absorbing samples.

In an effort to build further on the understanding of how the intrinsic integrating sphere properties shape the pathlength Hodgkinson *et. al.*[154] took a more theoretical approach and modelled the complete pathlength distribution. This included accounting for the launch/delaunch conditions i.e. where the initial incoming beam makes a pass across the sphere with no dependence on sphere reflectivity, and where the final (unreflected) pass to the detector is affected by the detector viewing angle. An expression for the fractional absorption was derived thus

$$\frac{\Phi_e(\alpha)}{\Phi_i} = \exp\left(-\alpha\left(2.52r + \frac{L_{sp}}{2}\right)\right) \times \frac{\ln\rho}{\ln\rho - \alpha L_{sp}} \qquad 4.23$$

where α is the absorption coefficient, r is the radius of the sphere, L_{sp} is the average distance for a single pass across the sphere, and ρ is the reflectance.

The theory was tested experimentally using a 50.8cm Spectralon™ sphere and detecting methane at 1651nm. The theory agreed well with the experimental data, with errors (totalling 0.5%) attributed to the absorbing effect of the gas as well as transmission

reading errors. Using the same components, predicted and experimental responses for direct transmission and 2f-WMS modulation techniques were compared for varying concentrations of methane[155]. These were compared with a predicted response for a single path equivalent to the calculated sphere effective pathlength. It was seen that the sphere results deviated from the single pass, with the non-linearity at higher concentration becoming more pronounced for the integrating sphere measurements. This more pronounced non-linearity was attributed to distortion of the resultant lineshape as a result of the exponentially decaying transfer function of the sphere. It is worth noting that this could introduce considerable errors if pathlength calculations using a reference single pass cell were derived from concentrations in the non-linear regime of the Beer Lambert law.

As well as pathlength derivations during steady state conditions, it was thought that by using a temporally short illuminating pulse the temporal decay of radiation in the integrating sphere could provide a sensitive means of calculating a pathlength. Fry *et. al.*[136] compared a derivation of the temporal response with that of a Monte Carlo simulation. Two derivations were considered, firstly where the zero of time was taken at the instant of the first reflection, i.e. the first strike spot, and secondly where the first reflection occurred at t_{sp}, the average time between reflections i.e allowing for the time it takes photons to be incident on the sphere wall.

$$\tau_1 = -\frac{1}{\ln \rho} t_{sp} \qquad 4.24$$

for first scenario, i.e. zero of time at first reflection, and

$$\tau_2 = \left(1 - \frac{1}{\ln \rho}\right) t_{sp} \qquad 4.25$$

for second scenario, i.e. first reflection occurs at time t_{SP}

where ρ is the sphere wall reflectance. t_{SP} can be expressed in terms of distance as d_{SP}/c, where d_{SP} is the average distance between reflections and c is the speed of light. The Monte Carlo simulation likewise considered these two scenarios where the photons were first started at random positions throughout the sphere and secondly where a point source on the sphere wall was chosen as the start position for the photons. In the

simulated cases it was found that the decay constants were almost identical for the two scenarios. For the analytical derivation, it was found that the results for the two scenarios lay either side of the Monte Carlo simulated decay constants, with scenario 1 i.e. zero of time at first reflection giving lesser errors. e.g. at reflectivity ρ=0.90, scenario 1 error was -0.67% vs. 9.8% for scenario 2. At high reflectivities the analytical values tended to converge e.g. at reflectivity ρ=0.99, scenario 1 error was -0.06% vs. 0.94% for scenario 2. In addition, building on Elterman's assertion that absorption measurements would be independent of the cavity geometry an expression for the L_{SP}, average distance between reflections for any arbitrary geometry was derived

$$L_{sp} = 4\frac{V_c}{A_s} \tag{4.26}$$

where V_c is the volume of the cavity, and A_s is the area of the sphere.

A practical example of an alternative geometry was demonstrated by Zhang *et. al*.[156]–[158] in their work, considering cubic cavities and their pathlength calibration. Here a reflective coating, Avian-D, was used to achieve an effective pathlength of 243±2cm for a 12cm length cube where measurements at 764nm of oxygen concentration in air provided a reference gas to make the pathlength measurement. Additionally an expression for the effective pathlength, L_{eff} was formulated by making measurements for varying port fractions. Note: varying port fractions were achieved by moving one side of the cavity by varying amounts.

$$L_{eff} = 0.723a\left(\frac{\rho}{1-\rho(1-f)}\right) \tag{4.27}$$

where α is the absorption coefficient, ρ is the sphere wall reflectance and f is the port fraction.

An alternative approach towards describing the temporal decay was demonstrated by Manojlovic *et. al*.[159], where the method was based on energy conservation rather than beam reflection analysis, in this case photon number conservation. By assuming that the initial number of photons in the cavity was much greater than unity and that during a time interval dt there were a large number of photon collisions with the cavity wall, the

number of photon collisions with the walls during that time interval could be quantified as

$$dN_c(t) = N(t) \cdot \frac{dt}{\tau} \qquad 4.28$$

where N(t) corresponds to the number of photons overall and τ is the decay constant of the sphere.

The probability of a photon being absorbed during a collision was given as (1-ρ) and thus the decrease in the overall number of photon i.e. due to absorption, during the time interval dt was equal to

$$dN_A(t) = (1-\rho) \cdot dN_C(t) \cdot \frac{dt}{\tau} \qquad 4.29$$

where ρ is the sphere wall reflectance. By combining equations 4.27 and 4.28 an expression for the decay time was found to be

$$\frac{dN_A(t)}{N(t)} = -\frac{1-\rho}{\tau} \cdot dt \qquad 4.30$$

The experimental work carried out in recent years by Hawe *et. al*.[78], [160], [161] using a 5cm diameter Spectralon sphere highlighted the range of gases, as listed in Table 4.2, that could be detected using Spectralon material. Another experimental body of research carried out by Chambers *et. al*.[162] likewise used a 5cm spectralon sphere for detection of CO_2, but in addition, an equation was derived to account for the transmitted flux when an absorbing species is present $\Phi_e(\alpha)$ and with a fibre coupled entry port

$$\Phi_e(\alpha) = \frac{\pi(r_f)^2}{4\pi(r)^2} \int_{-\sin^{-1}NA}^{\sin^{-1}NA} (\alpha)\cos(\alpha)d\alpha \qquad 4.31$$

where r_f is the radius of the fibre input, r is the radius of the sphere and NA is the numerical aperture of the fibre.

It was quickly realised that an integrating sphere multipass cell brought some of its own uncertainties. Indeed for this research, when initial derivations began for the ratiometric scheme as described in Chapter 5, the resultant discrepancies between the theory and

experiment could be corrected for by realising both a "gas pathlength" and a slightly longer "light pathlength" due to its additional propagation through the wall, termed by Fry *et. al*.[70] recently as the "wall time". In that body of research, a newly developed reflective material was described which, it was cited has a reflectivity of >99% at the desired wavelength e.g. 532nm. The wall time was calculated to be on the order of several nanoseconds, and though it was noted as important the conclusion was that, compared to the overall time that light spends in the cavity, the fraction of wall time would be minimal.

Indeed much of the work that has been described here and is summarised in Table 4.2 in Section 4.4 found that the change of sphere wall reflectance had contributed a much greater error to the predicted pathlength than factors such as changes in optical pathlength due to high concentrations of the species. To demonstrate just how heavily dependent the pathlength is on sphere wall reflectivity, the resultant theoretical pathlength vs sphere wall reflectance is plotted below in Figure 4.6 for a 5cm diameter integrating sphere, with port fraction 0.04 using Equation 4.3 and 4.10.

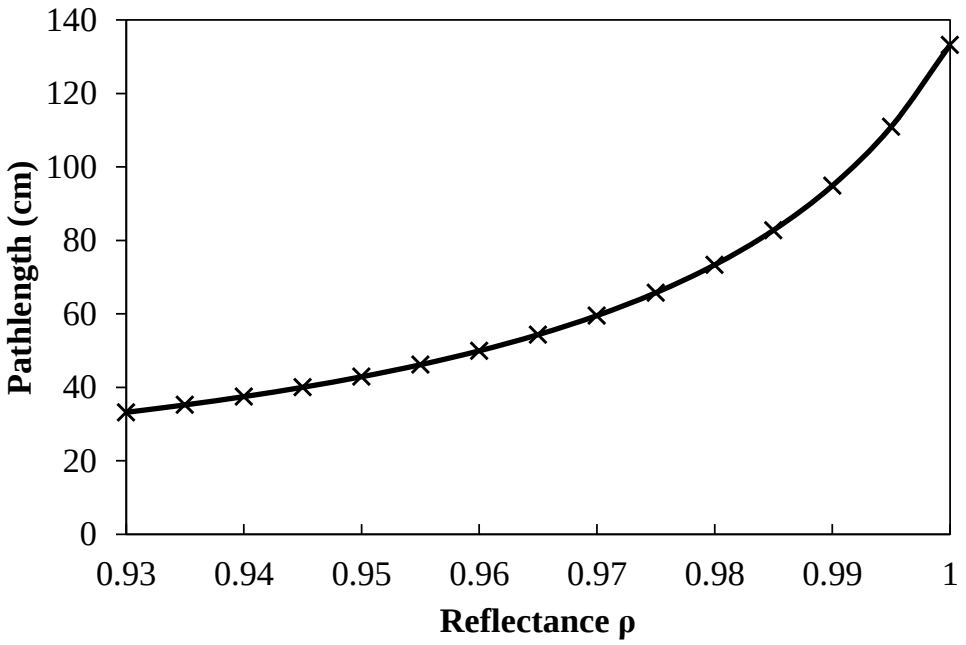

Figure 4.6: Dependence of pathlength on sphere wall reflectance, for a 5cm diameter sphere with a port fraction, f of 0.04

These parameters have been chosen as they are similar to those of the parameters in this body of research. It is evident from Figure 4.6 that a large reduction in pathlength can

occur with a small change in reflectance, for example a 1% reduction in reflectance from 0.99 to 0.98 reduced the pathlength by 21cm i.e. 23%.

4.4 Summary

Integrating spheres, as seen in the first section, have been well researched, from their earliest application making light flux measurements to their present day and largest application measuring reflectance and transmittance of diffuse or scattering materials. A wealth of mathematical relations exists to describe the diffusion of the light for these applications in terms of the sphere parameters, e.g. port fraction, reflectance.

When integrating spheres were proposed as a potential tool for absorption measurements, this prompted much research into the area, where different approaches and mathematical theories were developed to account for this new parameter, i.e. the absorbing species and its interaction with the sphere.

The research, as discussed in the previous section, is listed in table format below, highlighting some of the main ideas and theoretical derivations as well as the practical considerations in terms of components that were used and samples that were interrogated. The table has been divided into experimental (shaded sections) and theoretical work (clear sections). The terms in the equations have been standardised for the purposes of this thesis to be more comprehensible for the reader and are detailed in a key below the table.

Table 4.2: Summary of the development of the integrating sphere as a cell for absorption measurements

Author	Theoretical: Main idea	Theoretical: Equation	Experimental: Cavity properties: Material	Cavity properties: D	Cavity properties: Light source	Absorption variables: Specimen	Absorption variables: Wavelength	Absorption variables: Pathlength	Absorption variables: Limit of detection
Elterman[26] 1970	Integrating cavity to measure absorption coefficient of glass, while alleviating scattering related errors.	Refractive index of sample must be known $\alpha = \frac{A_s(1-\rho)(\frac{H_0}{H_\alpha}-1)}{4n^2V_c}$	$BaSO_4$	3.2 cm	Mercury lamp	Glass	0.55 µm	-	-
Venkatesh[143] 1980	IS to improve spatial intensity distribution for tunable lasers. Uses gas to calculate an effective pathlength for single and tandem sphere setup comparison	For single sphere $I = \frac{\Phi_i f_{exit}}{\Omega}(\frac{\rho}{1-\rho})$	Gold&180 grit SiC	3.8 cm	Lead salt laser	CO	5.00 µm	62.2 cm	-
Abdullin[151] 1988	IS as a multipass cell, pathlength determined by IS parameters not gas absorbance, as radiant losses are much greater from sphere surface. Thus pathlength related to sphere properties	$\Phi_e(\alpha) = \Phi_e(0)(\frac{1}{1+\varepsilon CL})$ where $L = \frac{r}{3Abs_w}$	Copper	10 cm	CO_2 laser	NH_3	9.30 µm	430±25cm	-
Berger[144] 1989	Coats IS wall with thin film to enhance sensitivity for matrix isolation spectroscopy. Weakly absorbing samples measurement enhanced as they experience more reflections. Does not obey Beer's law due to matrix effects	Corrects Beer's law deviation by including a transmittance factor $\Phi_e(m) = \frac{\Phi_i \rho A_d T}{[1-(1-f)\rho T]}$							

	Gold	1.3 cm	NdYAG laser	N_2O in CO_2 film	8.57 µm	NA	0.001 Absorbance units
Fry[138], [139], [163] 1990-1992	Integrating cavity absorption meter (ICAM). Sphere in a sphere setup which achieves isotropic illumination as incident light is diffused into inner cavity as opposed to typically from a single direction. Sphere is completely filled with sample.			For inner cavity containing sample $\alpha = \frac{1}{4V_C}(C_1 A_s(1-\rho)\frac{H_W}{H_\alpha} - A_s(1-\rho) - A_F)$			
	Spectralon cylinder	8.7 cm	Xenon arc lamp	H_2O	0.63 µm	Up to 10m	-
Kirk[146] 1995	Follows from Fry's ICAM, mathematically shows setup is unaffected by scattering. Models pathlength in terms of photons trajectories. Introduces a point source version, a PSICAM (central light source)			$N(t) = 1 - \frac{1}{2\alpha^2 r^2}[1 - \exp(-2\alpha r)(2\alpha r + 1)]$			
Tranchart[24] 1996	First use of IS for gas absorption. One drawback is non-linear relationship of absorbed power vs gas concentration			$\frac{\Phi_e(0) - \Phi_e(\alpha)}{\Phi_e(0)} = \frac{\alpha L}{[1-\rho(1-\alpha L)(1-f)]}$			
	Spectralon	10 cm	Multimode laser	C_4H_{10}	1.20 µm	203 cm	$3x10^{-3}$ cm^{-1}
	Spectralon	10 cm	Single mode laser	H_2O	0.83 µm	442 cm	$2x10^{-5}$ cm^{-1}
Fecht & Johnson[137] 1999	Falling stream in an IS. To alleviate scattering errors due to particles in water			$V = K(1 - G_\alpha + G_\alpha e^{-\alpha L})$			
	PTFE	10 cm	Blue LED	$CoCl_2$	0.43 µm	NA	0.005 AU
Davis[147] 2000-2003	Development of a PSICAM as introduced by Kirk, quantifying potential scattering errors. Also measures the absorption coefficient, using a transmittance ratio with a reference of known absorption						

Fry et. al[136] 2006	Using temporal response in an IS to derive average distance between successive reflections. Also derives an average distance for varying cavity shapes			$\tau_1 = -\frac{1}{\ln \rho} t_{sp}$ $\tau_2 = \left(1 - \frac{1}{\ln \rho}\right) t_{sp}$			
Javorfi[153] 2006	Accounting for attenuating effect of sample absorption on pathlength. Applies a correction to measured absorbance using experimentally derived fitting function. Correction function unique to each IS/detector setup			$A = \frac{1}{j_1}\left[\left(A'\right)^{\gamma} - 1\right]$ $\gamma = \frac{\log e}{j_0}$			
Hawe et. al.[78], [160], [161] 2006-2008	Spectralon	5 cm	Deuterium/ Halogen	O_3	0.63 µm	70cm	<500 ppm
			Deuterium/ Halogen	NO_2	0.37 µm	55cm	<5ppm
			LED	CO_2	2µm	36cm	10^{-4}
			Broadband	SO_2	1.57 µm	40.9cm	<15 ppm
Hodgkinson et. al.[154], [155], [164] 2009-2012	Modelled the pathlength distribution, accounting for launch/delaunch conditions. Demonstrated greater dynamic range due to its pronounced nonlinearity but potential for limiting effects due to speckle			$\frac{\Phi_e(\alpha)}{\Phi_i} = \exp\left(-\alpha\left(2.52r + \frac{L_{sp}}{2}\right)\right) \times \frac{\ln \rho}{\ln \rho - \alpha L_{sp}}$			
	Zenith	5 cm	DFB laser	CH_4	1.65 µm	125cm	1ppm
		10 cm	DFB laser	CH_4	1.65 µm	340cm	0.4ppm
Chambers[162] 2010	Equation to described a fibre coupled IS			$\Phi_e(\alpha) = \frac{\pi(r_f)^2}{4\pi(R)^2} \int_{-\sin^{-1} NA}^{\sin^{-1} NA} (\alpha)\cos(\alpha) d\alpha$			
	Spectralon	5 cm	LED	CO_2	2µm	63cm	

Manojlovic et. al.[159] 2011	Applies a photon energy conservation approach to measuring decay time in a sphere as opposed to beam reflection analysis. Agrees with other literature for high sphere wall reflectivities			$dN_c(t) = N(t) \cdot \frac{dt}{\tau}$ $dN_A(t) = (1-\rho) \cdot dN_C(t) \cdot \frac{dt}{\tau}$ $\frac{dN_A(t)}{N(t)} = -\frac{1-\rho}{\tau} \cdot dt$			
Lassen et. al.[145] 2014	Combination of an IS with organ tube for photoacoustic measurement. Tube present to further enhance signal through creation of resonance modes						
Zhang [129 ,130] 2014	Pathlength calibration of a diffuse cubic cavity, by using a variable port fraction and measuring oxygen line at 763nm Also used to estimate error as result of reflectivity change			$L_{eff} = 0.723a\left(\frac{\rho}{1-\rho(1-f)}\right)$			
	Avian-D cubic	5,8, 12 cm	VCSEL laser	O_2	764nm	243cm	-
Mason et. al. [70], [71], [165] 2015-2016	Studied water properties in 300-800nm region using ICAM. Using integrating cavity ring down spectroscopy (ICRDS), quantifies "wall time" of photon Applies ICRDS for absorption spectroscopy Low cost IS			$\tau = \frac{1}{-\ln\rho}\left(\frac{d_{avg}}{c} + \delta t\right)$			
	Fumed Si cylinder	6.35 cm	LED		468nm		

Notation list for Table

α	Absorption coefficient (m^{-1})	L	Pathlength (m)
A	Absorbance (unitless) = $\log_{10}(\varphi_i/\varphi_e)$	L_{eff}	Pathlength (m)
A’	Apparent absorbance (unitless)	n	Refractive index
A_d	Area of detector (m^2)	N(t)	Number of photons overall
A_F	Area of fibre optic output (m^2)	$dN_A(t)$	Number of photons absorbed by wall during time interval t
A_S	Area of sphere (m^2)	$dN_C(t)$	Number of photon collisions during a time interval t
Abs_w	Proportionality constant	Π	Solid angle (sr)
c	Speed of light (m/s)	$\Phi_e(0)$	Radiant transmitted flux, no absorbing species (W)
C	Concentration (ppm for example)	$\Phi_e(\alpha)$	Radiant transmitted flux, absorbing species (W)
C_1	Proportionality constant (between radiance of inner & outer sphere)	$\Phi_e(m)$	Radiant flux in presence of thin film matrix (W)
ε	Specific absorptivity (ppm/m)	Φ_i	Radiant flux incident on cell (W)
f	Port fraction	ρ	Reflectance
f_{exit}	Port fraction relative to exit port only	r	Radius (m)
$G\alpha$	Splitting fraction (i.e. due to particulates)	r_f	Fibre radius (m)
H_0	Irradiance of empty sphere	τ	Decay constant ($-\frac{2}{3}\bullet\frac{D}{c}\bullet\frac{1}{\ln\rho}$)($s^{-1}$)
H_α	Irradiance with absorbing species present	t	Time (s)
H_w	Irradiance within the integrating sphere wall	T	Transmittance factor
I	Radiant intensity (Wsr^{-1})	V	Voltage (V)
j_1, j_0	Fitting parameters, experimentally determined	V_c	Volume of cavity (m^3)
K	Detector sensitivity (V)		

The research that has been carried out to date has highlighted the challenges of adapting an integrating sphere for absorption measurements. These included discrepancies between predicted and measured pathlengths due to, for example geometry dependence

of beam passes assumed to be isotropic. Some of these challenges as well as proposed solutions are listed in Table 4.3.

Table 4.3: Some challenges and proposed solutions for adaptation of integrating spheres for absorption measurements

Challenge	Proposed solutions
Deviation in absorbance measurements due to intrinsic sphere parameters	A fitting function was defined experimentally which was limited to that particular sphere-detector pairing but usable for different absorbers [153]
Light backscattered to the laser create detection limiting interference fringes	Suggestions included an optical fibre delivery and / or a glancing-angle incidence beams to reduce the backscattered contribution[148]
Geometry dependence of beam passes assumed to be isotropic	A sphere-within-a-sphere setup created a completely isotropic input [139] A mathematical derivation was created to accommodate additional geometries within the pathlength distribution[154]
Multiple optical paths cause non-linearity in response.	An analytical equation that described the non-linearity was derived and validated experimentally[155]
The effective pathlength is a sensitive function of the sphere wall reflectivity, requiring a calibration check when in use.	The absorption of a selected line of oxygen in air was measured periodically; the O_2 concentration was assumed constant [158], [166] A correction factor was created by comparison of the calibrated empty sphere response with post-use empty sphere response[150]

The final challenge in Table 4.3 formed the main motivation for this thesis, namely optimizing the sensitivity of pathlength to sphere wall reflectivity. Two proposed solutions are listed in the Table: however these solutions in themselves have their limits. The first suggestion i.e. to measure the absorption of a selected line of oxygen in air, whilst having the advantage of not requiring a reference sample in situ, restricts the operating wavelength region to that of the oxygen absorption line, 764nm in this case. The other suggestion, where an in-situ dry sphere response was compared with a previously calibrated dry sphere response to normalise the absorption measurements, negated the requirement for a pure reference sample. This however is not done in real time and so does not account for potential contamination at the point of measurement. Furthermore to carry out inspection for potential pathlength changes, the sensor has to be removed from its location.

This body of research aimed to provide pathlength calibration even in the presence of sphere wall contamination. It was felt that though some preliminary academic based research has been carried out to demonstrate how an integrating sphere functions as a multipass cell, there had been no investigation into how the sphere would function if its performance worsened, e.g. if the sphere wall became contaminated. Two different strategies for calibrating the sphere pathlength were investigated and are described in Chapters 5 and 6.

5

A ratiometric technique for pathlength calibration

"The reflectance of an integrating sphere is a decisive factor for the attainable measuring accuracy. A maximally high reflectance close to 100 % is desirable in order to achieve optimum mixing of the light. However, the sensitivity to dirt and ageing of the coating goes up as the reflectance increases. The variations in the spectral throughput of the sphere also increase as a result" – Instrument Systems[167]

A review of the work to date, as discussed in Section 4.3, has shown that the achievable effective pathlength is highly dependent on the sphere wall reflectivity which is in itself very sensitive to particulate deposits and ageing. Much "proof of principle" type research has been carried out employing different strategies for initial pathlength calibration of an integrating sphere, including temporal based[136] or intensity based approaches [157], [168]. However, there has been little investigation into potential subsequent errors in these calibrated pathlength values if the system is subjected to an environment where conditions may degrade the reflectivity of the sphere wall, such as contamination. The technique detailed in this Chapter aims to provide real time pathlength adjustment in the event of sphere wall contamination using a low frequency ratiometric configuration. In this way gas absorption measurements can continue to be made accurately, as long as the contamination does not reduce the sensitivity to below an acceptable detection limit.

The first section describes the original application on which this technique is based, which is widely used in the water industry for measuring the turbidity of water samples. The main advantage that motivated the use of this configuration was that, as a result of the manner in which the measurements are processed, changes in intensity due to cell wall or window contamination can be factored out, allowing for ongoing accurate turbidity measurements to be made. The second section describes how the configuration is adapted for use in an integrating sphere. This includes a mathematical derivation, which combines the integrating sphere theory with the Beer Lambert law so that both

pathlength and gas measurements can be made. The experimental design is discussed, highlighting important considerations in terms of the alignment and data processing. The third section introduces the experimental results where the compensation and pathlength calibration capability of the scheme are tested for a number of scenarios where contamination or variation has occurred. The final section contains a discussion about the benefits of this type of configuration as well as the limitations, especially in terms of extensive contamination.

5.1 The original four beam ratiometric technique

The four beam ratiometric technique is so called because of both its configuration, i.e. there are four beam paths in the setup, and its principle of operation, i.e. that the final desired measurement e.g. turbidity or in this case, absorption, is calculated using a ratiometric algorithm constructed from these four flux measurements.

5.1.1 Working principle

As mentioned in the introduction, the proposed technique incorporates an adaptation of a four beam configuration that is extensively used in the water industry to provide an accurate measurement of fluid turbidity[169], [170]. An optical sensor of this design can be used to detect bacterial growth, cleanliness of water, or liquid levels in a fermentation tank. As cited in the original patent[171], the advantages of this four-beam technique are minimization of errors due to signal offset and gain, and accommodating fluids over a wide range of turbidity levels by adjusting the gain controls. The method can also compensate for component variation such as ambient temperature, ageing and degradation of component, voltage variations, and sample chamber contamination due to scratching or fouling (either biological or chemical) on the sample chamber body.

The typical configuration comprises two light sources and two detectors, spaced at 90° intervals around the sample chamber, as in Figure 5.1. The two light sources are alternately switched on and off, as seen in Figure 5.1(a) and Figure 5.1(b), while both detectors make a separate flux measurement for each light source, giving four independent measurements. The straight pass, e.g. from source 1 to detector 1 measures the transmitted light while the diagonal pass, e.g. from source 1 to detector 2 measures the scattered light, the magnitude of which is determined by the composition of the sample of interest present.

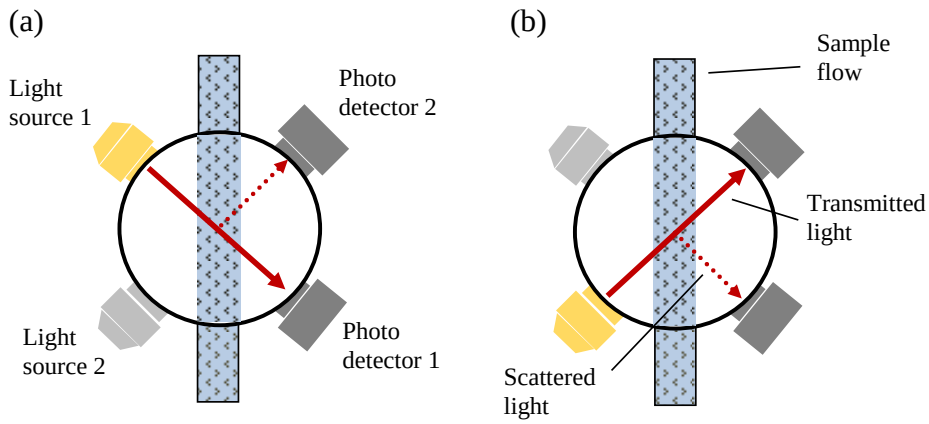

Figure 5.1: Typical four beam setup for turbidity measurement, comprising two light sources and two detectors spaced at 90 degree intervals. The two light sources are alternately switched on and off, (a) and (b), making four independent flux measurements. Adapted from Hydrolab[172]**.**

Relating the transmitted light flux to the scattered light for each source provides a means of ascertaining the level of turbidity. In the four beam configuration, a ratiometric algorithm is constructed from these values giving an expression of the form:

$$Q = \sqrt{\frac{\Phi_{12}\Phi_{21}}{\Phi_{11}\Phi_{22}}} \qquad 5.1$$

where Φ_{12} and Φ_{21} correspond to the scattered flux from source 1 to detector 2, and source 2 to detector 1 respectively. Φ_{11} and Φ_{22} correspond to the directly transmitted flux from source 1 to detector 1, and source 2 to detector 2 respectively. By using this ratiometric form, rather than the direct output from each detector, the overall light input and output remains directly proportional and errors due to cell contamination and/or component variation are thus eliminated. For example, if light source 1 experiences a reduction in light output, this will affect the measured flux at detector 2, i.e. Φ_{12} and detector 1, i.e. Φ_{11} equally and so the ratio between them will remain constant. As a result the overall ratiometric algorithm, as detailed in Equation 5.1, is unaffected by changes in sources or detectors powers, whether caused by component fluctuations or cell/window contamination The technology has been used in a number of industries, including milk fat monitoring in the food industry [22]. In this case the fat concentration is determined, using appropriate signal processing where the light absorption in the

direct path and the scattered light in the diagonal path allows for quantitative measurements of milk fat while compensating for scattering effects.

Where an absorption measurement is being made, the expressions for the transmitted fluxes take the following form[173]

$$\Phi_{11} = \Phi_{i11} S_1 K_1 \exp\left(-\alpha L_{11}\right) \qquad \Phi_{12} = \Phi_{d12} S_1 K_2 \exp\left(-\alpha L_{12}\right) \tag{5.2}$$
$$\Phi_{22} = \Phi_{i22} S_2 K_2 \exp\left(-\alpha L_{22}\right) \qquad \Phi_{21} = \Phi_{d21} S_2 K_1 \exp\left(-\alpha L_{21}\right)$$

The values of L_{ab} are the optical pathlengths from source a to detector b. S_1 and S_2 are factors that scale with the fluxes from sources 1 and 2 respectively, and K_1 and K_2 represent the sensitivity of detector 1 and 2 respectively. Φ_{iab} and Φ_{iab} represent the incident flux for the direct and indirect/diffuse measurement respectively.

These quantities take account of the (fixed) proportions of light entering the respective straight and diagonal paths, plus potential reductions in flux resulting from transmission through the cell windows. Forming the Q ratio then allows these factors, which can potentially change as a result of window fouling for example, to cancel, thus:

$$Q = \frac{\Phi_{12}\Phi_{21}}{\Phi_{11}\Phi_{22}} = \frac{\Phi_{d12}\Phi_{d21}}{\Phi_{i11}\Phi_{i22}} \exp\left[-\alpha\left(L_{12} + L_{21} - L_{11} - L_{22}\right)\right] \tag{5.3}$$

5.1.2 Practical considerations

For practical implementation of this system, there are a number of design considerations that can influence achievable sensitivity, and accuracy of the system. For example the resolution of this configuration can be improved by increasing the difference between the length of the transmitted and scattered paths[173]. However this has consequences for alignment as wider source dispersion and detector acceptance angle is required.

Furthermore the compensation scheme works on the assumption that the transmitted flux of the straight-through and diagonal paths for each light source remains proportional. In practice this is not completely preserved as, depending on the sampling environment, the system may be subjected to contamination which will not be identically distributed for each path, whether as a result of geometrical effects or structure of the fouling particle[173]. From a geometrical point of view, especially when using planar windows, the level of attenuation for each path differs as they are subject to

different layer thicknesses dependent on the angles of the beams passing through, as in Figure 5.2. This divergence from proportionality will increase with increased fouling.

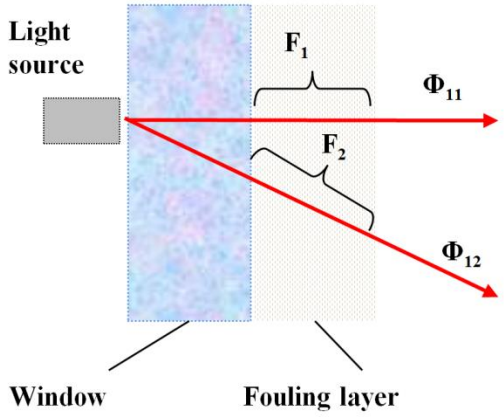

Figure 5.2: Scheme showing variation in attenuation by fouling layer due to angle of the beams. Adapted from Johnson[173]**.**

From a structural point of the view, the uniformity of the contamination layer as well as its particulate nature will affect the proportionality between the transmitted intensities. If the layer is not uniform or the particulates are of similar size as the source/detector the two paths can experience very different levels of attenuation. However this has not prevented the technique from being used successfully, where the application can tolerate sizeable errors e.g. up to 15%[173]. With these considerations in mind, an adaptation of this technique was implemented for an integrating sphere.

5.2 The adapted four beam ratiometric technique

5.2.1 Working principle - theoretical

It is proposed that the cited advantages of the four beam configuration can be exploited for an integrating cavity using an adaptation of this arrangement. For adaptation of this technique to an integrating sphere, four beam paths must be created, as shown in Figure 5.3. Port openings for the detectors are introduced in the sphere directly opposite the light sources openings, i.e. detector 1 sits at the first strike spot for source 1 and likewise for detector 2 and source 2. A portion of the light makes a single pass through the sphere, of length roughly equal to the sphere diameter, providing the direct (short) path. The remaining portion of the light encounters the sphere wall, and is diffusely scattered around the sphere. After multiple random passes, of different lengths, a

proportion of the light is detected by the detector perpendicular to the source and this, corresponding to the diffuse (long) path, or mean effective pathlength.

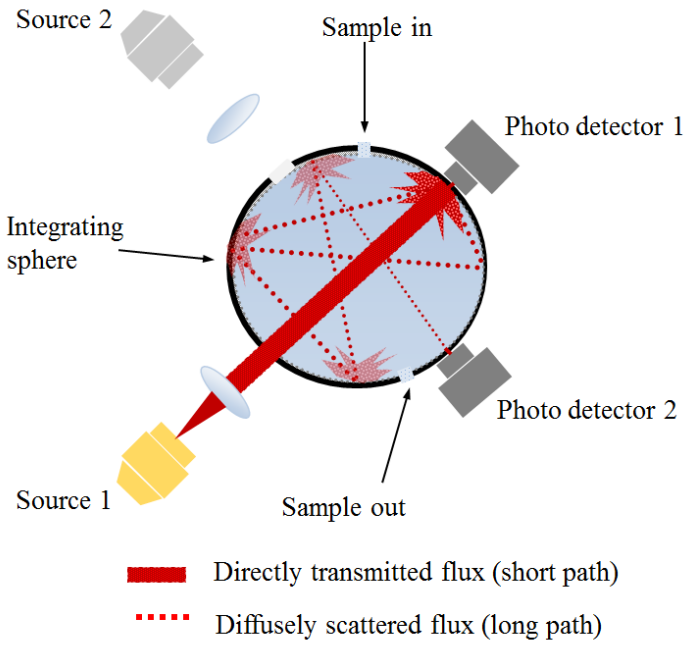

Figure 5.3: Adapted four beam ratiometric scheme; where for example, with source 1, a single path through the sphere provides a direct (short) path with flux Φ_{11}. The diffusely reflected light measured from each detector orthogonal to the light source provides the diffuse (long) path, with flux Φ_{12}. The same principle applies to source 2.

In terms of the design, it is necessary to control the divergence of the source beam so that the short and long paths operate as independently of each other as possible. This is achieved by using a narrowly diverging beam such that a considerable proportion of the light (30-40%) is directed to the short path detector. As a result, changes to the sphere wall that reduce the diffuse long path flux will have a negligible effect on the detected short path flux. Simultaneously, a sufficient proportion of the light encounters the sphere wall so that the radiant flux in the diffuse path is detectable, i.e. above the noise level of the corresponding detector. This should be true for both combinations of sources and detectors. In addition it is important that the two source/detector combinations are symmetrically aligned for accurate compensation as the mathematical derivation assumes equivalent mean effective pathlengths.

To account for the pathlength change due to cavity wall contamination, two Q expressions of the form as seen in Equation 5.1 are formed simultaneously, one

accounting for the presence of the sample of interest, Q(α) and the other with zero analyte present, Q(0). In this way the changes in throughput (for the diffuse (long) paths in particular) due to absorption by the sample of interest can be differentiated from other causes of throughput changes, i.e. cavity wall contamination. This allows for the pathlength to be adjusted accordingly and thus the gas absorption coefficient can be determined continuously without needing to recalibrate the sphere in situ.

One point to note is that the use of this configuration does potentially introduce a disadvantage in that the port fraction is increased as a result of the requirement for two additional port openings i.e. to accommodate a source and detector. The consequence of this in terms of achievable pathlength for this particular setup, i.e. for an integrating sphere with diameter of 5.08cm, experimentally determined reflectivity of 0.975 at 1650nm is listed in Table 5.1. Here the current setup with 6 ports is compared with the same setup if one source and one detector port opening were omitted. The theoretical achievable pathlength is calculated using Equations 4.3 and 4.10.

Table 5.1: Effect of port fraction on effective pathlength. Data shows the theoretically achievable pathlength when additional ports are introduced i.e. 4 ports vs. 6 ports. For a sphere with diameter = 5.08cm and reflectivity = 0.975

	Port fraction, f	Theoretical pathlength
Four beam setup (6 ports)	0.0077	99.8cm
Conventional setup (4 ports)	0.004	112.2cm

In this case, though it is conceded that both factors i.e. reflectivity and port fraction have a large effect on the resultant pathlength, the focus of this body of research is on changes in reflectivity specifically rather than port fraction optimisation. It is felt that, unlike the port fraction, this value can deviate from the calibration when placed in the field e.g. due to sample containing particulates or even aging of the sphere material causing deviations from the quoted value as given by the manufacturer. In this body of research the pathlength has been calculated experimentally without assuming a constant reflectivity of 98.7% as given by the manufacturer. It is worth mentioning that one must be careful when using the quoted reflectivity as stated by the manufacturer as these

values assume optimum conditions, e.g.. ideal material thickness, no degradation of reflectivity. In reality, and indeed in the case of this research, machining may result in tapering at the port openings. In the case of the 5cm sphere that was used in this research, the material on the ports is only a few mm thick and thus it is not expected that the reflectivity at these ports will be as high as the bulk material. Additionally the sphere was purchased in 2006 and was stored with openings exposed and so it could be suggested that there may be some degradation/contamination of the sphere surface that may lower the overall reflectivity.

5.2.2 Working principle - mathematical

The mathematical description of this configuration can be derived from combination of integrating sphere theory as detailed in Section 4.2, with the relations governing absorption spectroscopy, namely the Beer Lambert law, i.e. Equation. 2.3

Considering the Beer Lambert law in the absence of gas, assuming that the beam is collimated and there are no other components in the beam path that absorb or scatter the light, the transmitted flux is equal to the incident flux and the Beer Lambert law reduces to

$$\Phi_e(0) = \Phi_i \exp(0) = \Phi_i \qquad 5.4$$

For the four beam configuration, this can be applied to the direct, short paths where the light does not contact with the sphere walls. For each diffuse long path on the other hand, the transmitted flux has an additional dependence on the reflectivity of the sphere wall and detector field of view. And so for the diffuse long paths, the incident flux term Φ_i can be replaced by another term namely the expected transmitted flux, Φ_d. The expected transmitted flux is described by the flux incident on the detector Φ_i, as detailed in equation 4.5. Relating this to the Beer Lambert law, in the absence of the analyte, the equation becomes

$$\Phi_e(0) = \Phi_d \exp(0) = \Phi_d \qquad 5.5$$

Equations 5.4 and 5.5 describe the expected flux for the direct short paths and diffuse long paths respectively. Following from the four beam explanation as described in

section 5.1.1 a ratiometric expression for Q(0) i.e. no analyte present, can be created, using equations 5.4 and 5.5, to become

$$\Phi(0) = \frac{\Phi_{d12}(0)\Phi_{d21}(0)}{\Phi_{i11}(0)\Phi_{i22}(0)} \qquad 5.6$$

Forming the Q ratio in this manner has the advantage of removing sensitivity to source power fluctuation, average window degradation and/or detector responsivity, as cited in section 5.1.1. The zero measurement for each path can be obtained by measuring the radiant flux at one or a number of wavelengths where the analyte does not absorb light (a baseline measurement) and inferring the value of the measurement in the absence of the analyte at the absorbing wavelength(s). To correct for changes to the integrating sphere pathlength, we proceed as follows.

Pathlength correction When contamination of the sphere wall occurs, it is assumed that the transmitted flux of both diffuse long paths will drop equally. Because the optical beams in the direct paths do not encounter the sidewalls, it is reasonably assumed that changes to the direct short paths L_{11} and L_{22} as a result of sphere wall contamination are negligible. Changes to the diffuse long pathlength can be recognised, and adjusted for by relating changes to the Q(0) expression from its in-house, calibrated state, designated as $Q(0)_{cal}$, to the in-field, potentially contaminated situation, designated as $Q(0)_{foul}$. This is done by forming an expression for the fractional change in the two values

$$\frac{Q(0)_{foul}}{Q(0)_{cal}} = \frac{\Phi_{d12}(0)_{foul}\Phi_{d21}(0)_{foul}}{\Phi_{i11}(0)_{foul}\Phi_{i22}(0)_{foul}} \times \frac{\Phi_{i11}(0)_{cal}\Phi_{i22}(0)_{cal}}{\Phi_{d12}(0)_{cal}\Phi_{d21}(0)_{cal}} \qquad 5.7$$

Substituting the values for the diffuse long path transmitted fluxes from equation 4.5, the expression becomes

$$\frac{Q(0)_{foul}}{Q(0)_{cal}} = \frac{\Phi_{i12}kM_{12}(0)_{foul}\Phi_{i21}kM_{21}(0)_{foul}}{\Phi_{i11}(0)_{foul}\Phi_{i22}(0)_{foul}} \times \frac{\Phi_{i11}(0)_{cal}\Phi_{i22}(0)_{cal}}{\Phi_{i12}kM_{12}(0)_{cal}\Phi_{i21}kM_{21}(0)_{cal}} \qquad 5.8$$

As it is assumed that changes to the direct short paths are negligible, the flux values cancel for all short paths. The k constants likewise cancel leaving an expression in terms of the multiplier only

$$\frac{Q(0)_{foul}}{Q(0)_{cal}} = \frac{M_{12}(0)_{foul} M_{21}(0)_{foul}}{M_{12}(0)_{cal} M_{21}(0)_{cal}} \quad 5.9$$

By rearranging equation 4.10, the multipliers can be expressed in terms of their mean effective pathlengths [97]

$$M = \frac{2}{3} DL \quad 5.10$$

where D is the diameter of the sphere, and L is the mean effective pathlength. Substituting this into equation 5.9 for each value of M, the constants cancel and the expression becomes

$$\frac{Q(0)_{foul}}{Q(0)_{cal}} = \frac{L_{12}(0)_{foul} L_{21}(0)_{foul}}{L_{12}(0)_{cal} L_{21}(0)_{cal}} \quad 5.11$$

It is assumed that, due to the sphere's property of uniform light diffusion, the paths have been set up symmetrically, i.e. $L_{12}=L_{21}$, and so the expression becomes

$$\frac{Q(0)_{foul}}{Q(0)_{cal}} = \frac{(\mathrm{L}(0)_{foul})^2}{(L(0)_{cal})^2} \quad 5.12$$

Thus the $L(0)_{foul}$ can be calculated by rearranging this equation to become

$$L(0)_{foul} = L(0)_{cal} \sqrt{\frac{Q(0)_{foul}}{Q(0)_{cal}}} \quad 5.13$$

Once the pathlength has been adjusted as detailed above, the gas absorption can be made as follows.

Making the gas measurement Utilising the four beam ratiometric principle two Q expressions are formed and combined with equation 2.3 to give a general expression for gas absorption measurement as

$$Q(\alpha) = Q(0) \exp^{-\alpha L^*(0)} \quad 5.14$$

where Q(0) is the expression as detailed in equation 5.6. L*(0) is the pathlength sum equal to $(L_{12}+L_{21})-(L_{11}+L_{22})$. Q(α) corresponds to the ratiometric expression of the

transmitted fluxes, measured in the presence of the analyte of interest, and is formed in the same manner as equation 5.6

$$Q(\alpha) = \frac{\Phi_{e12}(\alpha)\Phi_{e21}(\alpha)}{\Phi_{e11}(\alpha)\Phi_{e22}(\alpha)} \quad 5.15$$

Initially the sensor is characterised and calibrated, inputting methane at varying but known concentrations so that an effective absorption coefficient, α, is assigned for that particular setup and is given by

$$Q(\alpha)_{cal} = Q(0)_{cal} \exp(-\alpha L^*(0)_{cal}) \quad 5.16$$

which corresponds to the clean, as per calibration state that measurements will be related back to. If the system deviates from its calibrated state the expression is termed

$$Q(\alpha)_{foul} = Q(0)_{foul} \exp(-\alpha L^*(0)_{foul}) \quad 5.17$$

where the Q expressions correspond to the flux measurements in a potentially contaminated state, with analyte, $Q(\alpha)_{foul}$, and without analyte, $Q(0)_{foul}$. $L^*(0)_{foul}$ corresponds to the adjusted pathlength sum as calculated from equation 5.13. Thus, the gas concentration may be accurately determined in conditions where the sphere pathlength may have degraded. In this way, the integrating sphere relations are used to make measurements of sphere transmitted flux, which relates to the mean effective pathlength. The four beam configuration allows for measurement of that flux in a manner that is insensitive to changes in source intensity, average window degradation or detector responsivity.

5.3 Experimental implementation of four beam technique

5.3.1 General setup

Absorption measurement setup A schematic of the setup is shown below in Figure 5.4(b). Two 1651nm distributed feedback single mode fibre pigtailed (DFB) lasers (NTT Electronics corp. NLK 1U5EAAA) with a typical output power of 20mW at 100mA were used, with the beam divergence for both controlled using aspheric lenses (Thorlabs C280TM-C). The interrogation system used was a simple form of direct absorption spectroscopy, in which the emitted wavelength from each tunable

diode laser was scanned across a methane line at 1651nm. This was achieved by applying a 1kHz sawtooth waveform produced by a function generator (Hewlett Packard HP33120A) to a driver (Laser 2000 LDC202), which resulted in the current varying between a minimum of 90mA and a maximum of 130mA (corresponding to a wavelength range of 0.28nm (31 GHz)).

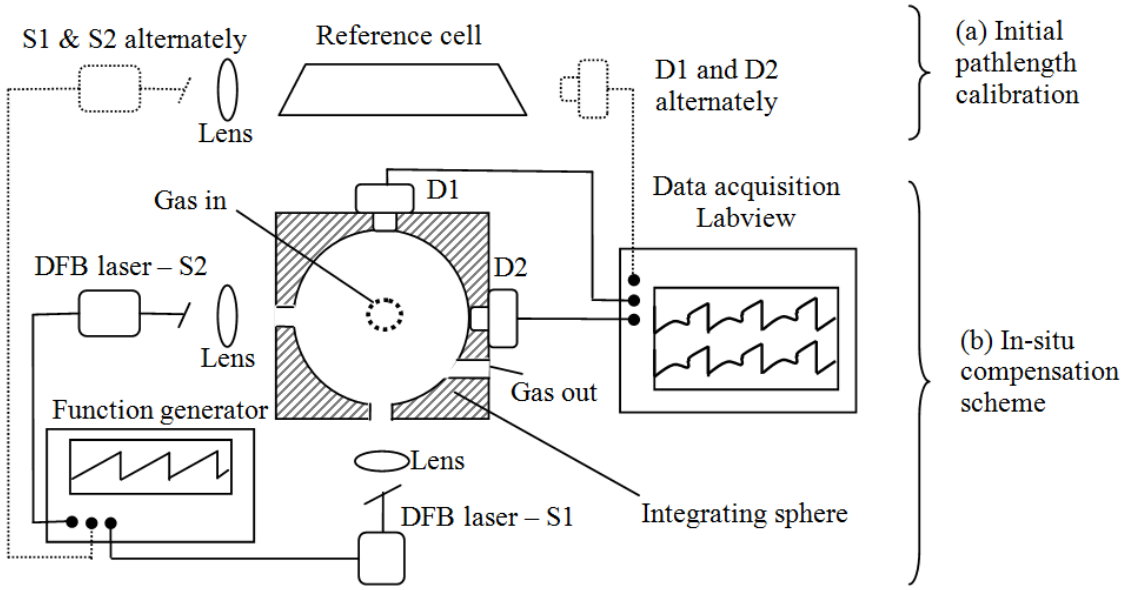

Figure 5.4: Experimental setup of ratiometric four beam technique. S1 and S2 are light sources, D1 and D2 are amplified detectors. (a) is the initial pathlength calculation stage using a reference cell of known length, and (b) is the subsequent in-situ measurement

The integrating sphere was composed of Zenith^{TM} material (Thorlabs IS200-4, manufactured by Sphere Optics), with an internal diameter of 5.08cm and an experimentally determined reflectivity of 97.5%. The sphere was modified to contain six ports; two facilitated light entry for the sources, two facilitated light exit at the detectors, and two provided gas entry and exit points. These were spaced around the sphere so that each detector was positioned opposite one source and at 90° to the other source. The detectors were recessed from the sphere ports so that baffles were not required. Orientation of the final two ports, i.e. for gas entry and exit, was not important as long as they avoided first strike spots and areas opposite each detector. Two variable gain amplified detectors were used (Thorlabs PDA10CS) at different gain settings. This was necessary as the exit flux of each direct short path was three orders of magnitude greater than that of the long path. Triggering from the falling edge of the sawtooth

waveform, transmitted flux measurements for direct short paths, i.e. S1 to D1, and S2 to D2 were made at 0dB gain and diffuse long path measurements i.e. S1 to D2 and S2 to D1 were made at 50dB gain.

Test gases were fed to the gas cell from three certified cylinders (Scott Specialty Gases), one containing hydrocarbon (HC) free air and the other two containing methane (1010ppm and 2.5% volume in hydrocarbon free air). The gas flow rate was maintained at 1000 standard cubic centimetres per minute (sccm) for all measurements using a bank of thermal mass flow controllers, MFCs, (Brooks 0254 controller and GF40 series MFCs). Different gas concentrations from 0 to 6250ppm were achieved by controlled downstream mixing of air and methane from the relevant cylinder.

Initial pathlength calculation setup The initial pathlength of the sphere was determined experimentally using a second setup as shown in Figure 5.4(a). Each laser was first coupled into a 114.5cm gas cell with AR coated wedged windows, and then coupled into the integrating sphere at the respective port, as in Figure 5.4(a). The gas inlet and outlet pipes were connected so that the reference cell and integrating sphere were filled with the same concentration of gas, in series.

The transmitted signal was recorded with methane present (1010ppm concentration), corresponding to $\Phi_e(\alpha)$, and with hydrocarbon free air, corresponding to $\Phi_e(0)$. This was recorded for the reference cell and sphere for both lasers. The pathlength was calculated as detailed using the following equation

$$L_{sphere} = \frac{A_{sphere}}{A_{cell}} L_{cell} \qquad 5.18$$

where A_{sphere} is the measured absorbance in the sphere and A_{cell} is the absorbance in the reference cell. The pathlength of the reference cell, L_{cell}, was measured as 114.5±0.1cm The resultant mean effective sphere path lengths, L_{sphere} were thus calculated to be 99.2±0.4cm for source 1 to detector 2 (L_{12}) and 100.4±0.4cm for source 2 to detector 1 (L_{21}). These pathlength values are then included in the initial, calibrated Q expressions, to which all subsequent in-situ Q expressions are compared.

5.3.2 General data processing

Figure 5.5 shows an example of raw data collected directly from the detector, for hydrocarbon free air and a methane concentration of 1010ppm. The data for each beam path measurement was collected in this way.

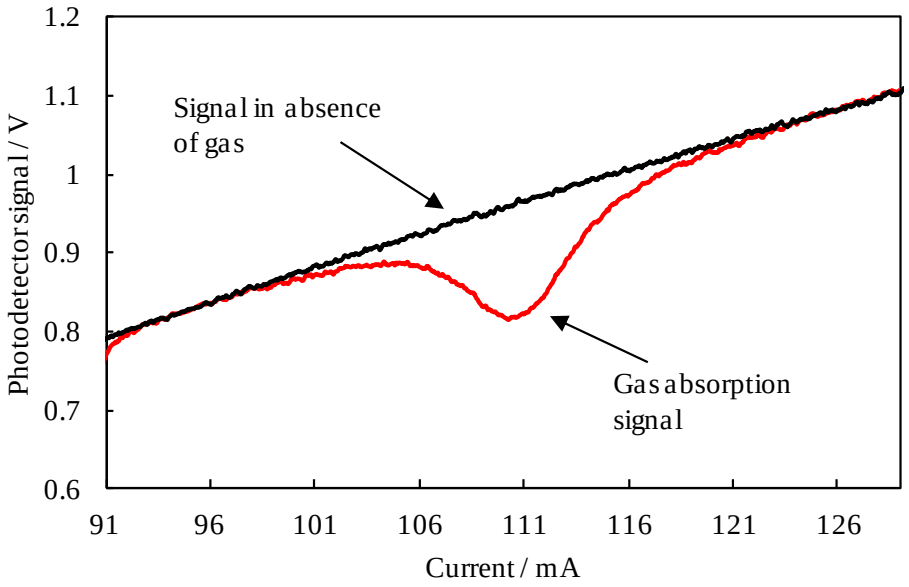

Figure 5.5: Example of raw data obtained for each path. In the presence of methane, a dip corresponding to a gas line is observed.

In the absence of gas, a rising output intensity with current was seen, as expected. In the presence of methane, a dip corresponding to a gas line was observed. The $\Phi_e(\alpha)$ "absorbing" value for each beam path was calculated by averaging over 30 data points (i.e. 1% of the total scan) closest to the line centre, corresponding to a wavelength range of 0.67pm around the gas line centre. The $\Phi_e(0)$ "zero-gas" value for each beam path was derived by using the measured radiant flux values at each wavelength along the ramped waveform where the analyte *does not* absorb light (a baseline measurement) and inferring "zero-gas" values at the absorbing wavelength(s). As with the $\Phi_e(\alpha)$ value, the $\Phi_e(0)$ was calculated by averaging over 30 of these inferred data points corresponding to the portion of the scan where the gas absorption measurements were taken. The measurements for all short and long paths are treated in this way for all conditions, i.e. whether with induced errors or not, and form the Q expressions.

To summarise how the four beam setup is implemented, Figure 5.6 contains a chart of the main equations relating to the setup. See explanation overleaf.

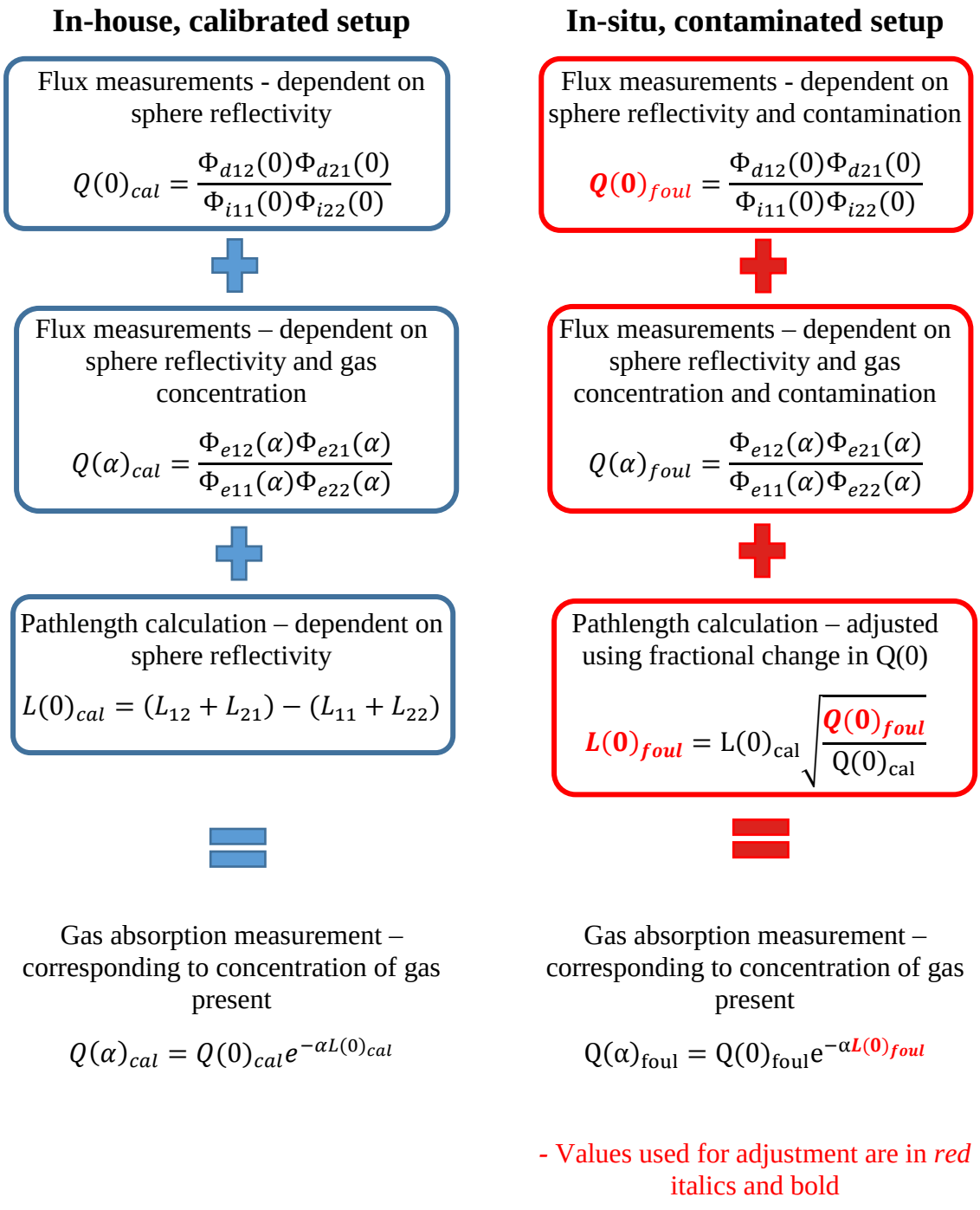

Figure 5.6: Comparison of the equations pertaining to the in-house calibrated vs in-field potentially contaminated setup. Correction factors for contamination are applied by adjusting the values in red

The left hand side in blue, relates to the setup when it is first calibrated i.e. there is not expected to be any contamination and so changes in output flux are attributed to the presence of the absorbing gas. The right hand side in red relates to the in-situ setup where, as well as an absorbing gas, there is also the potential for contamination which will introduce errors into the absorption measurement. To compensate for this, correction factors for contamination are applied by adjusting the values highlighted in red and bold italics.

To aid understanding, the chart for the contaminated setup (on the right hand side) will be included in the experimental section for each source of error induced with the corresponding value that has been affected by the error source, highlighted in red.

5.3.3 Induced errors

It is claimed[171] that the four beam method, as configured for turbidity measurement can compensate for component variation, and sample chamber contamination, and so it was decided to test whether these advantages held in an integrating sphere setup. Unlike for the traditional four beam configuration, any sphere wall contamination will contribute to pathlength changes in the diffuse long path, introducing a further error into the calculations, as described in section 5.2. Thus three different degradation scenarios were considered in the setup, Figure 5.7.

- component variation
- sphere wall contamination
- sphere window contamination

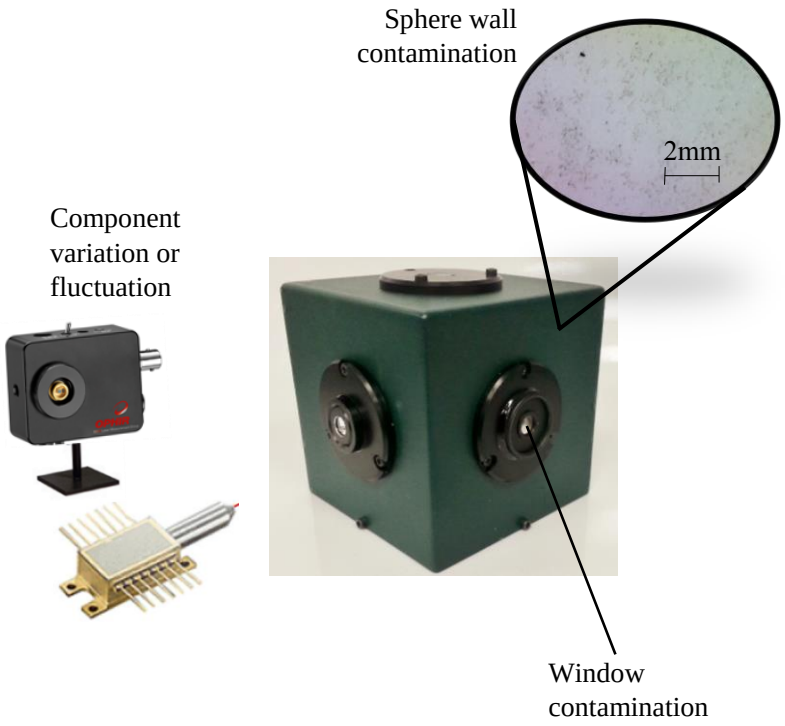

Figure 5.7: Illustration of error sources tested, change in flux due to component variation or fluctuation, contamination on the input or output windows, or change in pathlength due to sphere wall contamination. (not actual sphere used)

5.4 Experimental results

5.4.1 Component variation

Absorption measurements using TDLS are self-referenced and therefore not expected to be affected by changes in source power or detector responsivity. However it was considered important to confirm that such advantages would be maintained for the four beam technique without introducing additional errors. To test the effect of component variation on the compensation scheme, a reduction in the output power of source 1 was simulated by reducing the laser current from 110mA to 105mA. Simultaneously the laser temperature was adjusted from 14.53 to 14.58°C to ensure that the methane gas line at 1651nm remained centred as the wavelengths were scanned. The chart in Figure 5.8 shows that mathematically, the source 1 long and short path flux values are affected by the component variation, however, due to their ratiometric configuration, the overall Q expressions are unaffected by the changes.

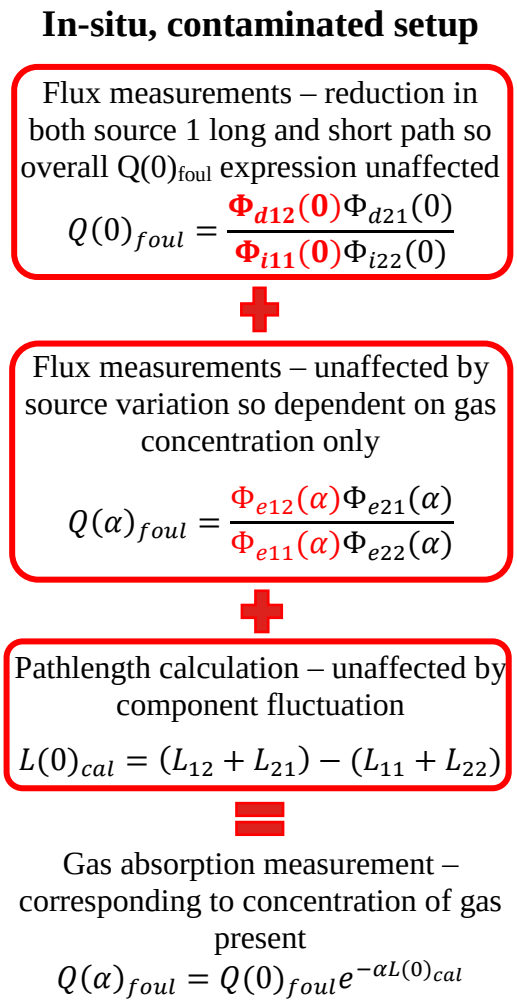

Figure 5.8: Component variation, reduction in source 1 power gives equal reduction in the respective long and short path powers thus leaving Q expressions unaffected overall.

To investigate the effect of a reduction in source intensity, the Q(α) expressions for a number of concentrations were compared with the calibrated Q(α) expressions, where there was no reduction in intensity. With a reduction in laser current from 110mA to 105mA, a percentage reduction of approximately 4.5% in source output power would be expected

Experimentally, as seen in Table 5.2, the errors as a result of component variation amount to less than 0.5% when the four beam compensation scheme is applied. In contrast, the single long path values have an average error of 4.4%, which is close to the predicted error of 4.5%. There is some deviation from the predicted error but this is attributed to the effects of the temperature also being tuned to ensure the gas line is centred in the wavelength range being scanned.

Table 5.2: Effect of component variation on measured flux when using the four beam ratiometric compensated vs. a single uncompensated diffuse path. The values correspond to the changes in output flux and associated measured absorption following a reduction in the emitted power of the laser diode

	Uncompensated (diffuse long path L_{12})		Compensated (four beam configuration)	
Methane conc. (ppm)	Output flux, (% change)	Absorption(α), (% change)	Q(α) flux, (% change)	Absorption(α), (% change)
0	-4.1	N/A	-0.2	N/A
1500	-4.5	1.4	0.0	1.0
3125	-3.4	-1.9	-0.1	-0.9
6250	-4.1	-1.3	0.4	-0.6

The effective absorption coefficient was then calculated for the compensated scheme and uncompensated single diffuse path measurement. As detailed in Section 5.3.2, the absorption coefficient is calculated by comparison of the peak absorption to an inferred zero level measurement from the same data sample, and so the measurement is effectively self-referencing. The result of this, as seen in Table 5.2, is for an uncompensated single diffuse path, component variation did not contribute an appreciable error to the resultant absorption coefficient. It can be seen likewise that, despite a potential for increased error due to four beam paths being considered, the errors in Q(α) flux and absorption measurements due to source variation are similar to those in the single path. With errors of less than 1% in the flux measurements, the four beam configuration compensates well for source variation and using this type of configuration does not contribute a further error to the absorption measurement.

5.4.2 Sphere wall contamination

To test the effect of contamination onto the sphere wall it was necessary to come up with a method for inducing contamination that would be repeatable and wouldn't irreversibly damage the sphere. It was decided to use something adhesive so that contamination could be implemented at various locations around the sphere wall rather than just settling at the bottom. Black adhesive insulating tape was used as it was suitably non-reflective so as to cause an appreciable reduction in the overall reflectivity.

It was cut into approximately 7x5mm black tabs, as seen in Figure 5.9(a). In order to prevent disruption of the alignment, the induced contamination could only be inserted through one port opening at the top i.e. by removing the gas input port giving an opening of approximately 1cm diameter. This made insertion of the tabs more challenging and so small loops, using the same adhesive insulating tape, were added to aid placement and subsequent removal of the tabs without damaging the sphere wall.

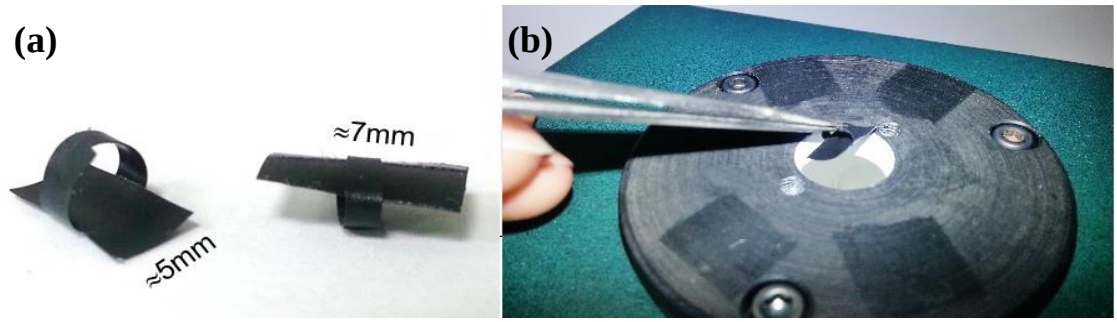

Figure 5.9: (a) black adhesive fouling tabs used to simulate contamination of the sphere wall, and (b) placement of tabs in integrating sphere (not actual sphere used)

During the experimental design it was considered that the addition of loops to the tabs, as well as the fact that the reflectivity of the tape is not known adds a level of uncertainty to the measurements in terms of actual pathlength contamination. But actually, as the technique is relating changes (that in practise would not be known) back to a calibrated setup it is not necessary to know the reflectivity of the contamination or indeed the exact coverage of the sphere wall contamination. Knowing that all areas of absorption have not been accounted for in these values, i.e. the tab loops, the experimental results for sphere wall contamination have nevertheless been quoted in terms of % sphere wall coverage based on the dimensions of the tabs to facilitate logical presentation of the data.

Using Equation 5.16, effective absorption coefficients for a number of methane concentrations were calculated with no induced contamination on the sphere wall. These were taken to be the calibrated values for this sphere setup. Fouling tabs, as seen in Figure 5.9, were placed into the sphere, one at a time, taking flux measurements of the four paths each time a new tab was placed inside the sphere. The $Q(\alpha)$ and $Q(0)$ expression were formed as described in Section 5.3.2. The $Q(0)_{foul}$ expression for each

contaminated setup was related back to the uncontaminated $Q(0)_{cal}$ expression, so that the L*(0) pathlength sum could be adjusted to reflect the change in mean effective pathlength due to contamination, as illustrated in the chart in Figure 5.10. For each level of induced contamination an effective absorption coefficient was calculated, substituting in the adjusted L*foul as calculated for each level of contamination. These were compared with the original calibrated absorption values to ascertain the level of compensation achieved.

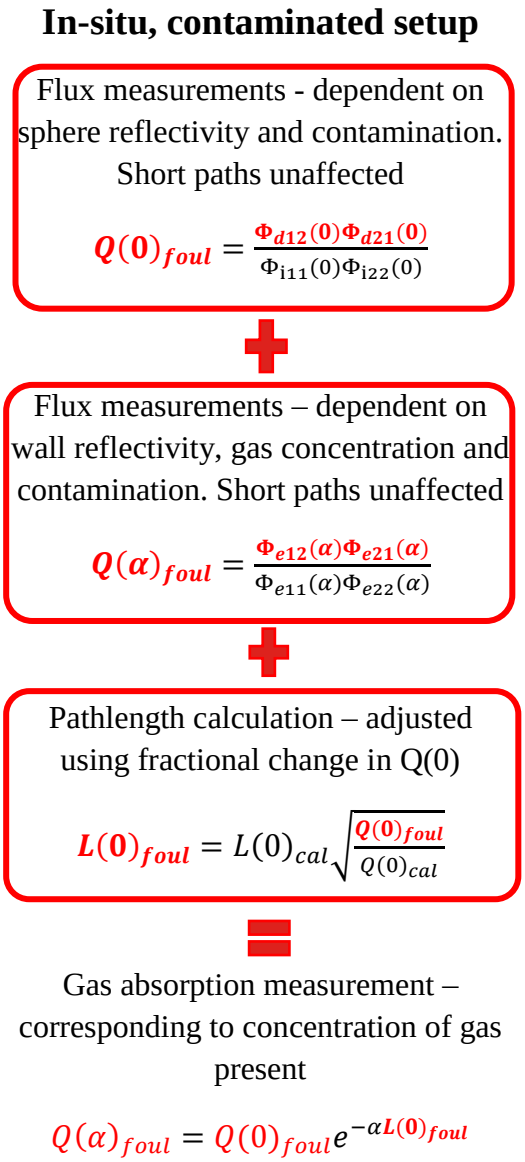

Figure 5.10: Sphere wall contamination, contamination of the sphere wall causes a reduction in the long (diffuse) paths and as a result the pathlength sum. The pathlength sum can be adjusted using the fractional change in Q(0), thus allowing for accurate gas concentration measurement

As a comparison, for each concentration, the effective absorption coefficient was calculated using the Beer Lambert law for one set of long path measurements; a single diffuse path but without applying a pathlength adjustment. To demonstrate the extent of the difference between the uncontaminated calibrated system and the subsequently fouled situations for both the compensated ratiometric scheme and the unadjusted single diffuse path, the absorption coefficient values were expressed in terms of their percentage errors (from calibration), as shown in Figure 5.11. The random error was calculated by repeating the experiment three times (removing all tabs and replacing at different positions each time) for a single concentration and looking at the standard deviation for each level of sphere wall coverage. The quoted random error value is then an average of these standard deviations.

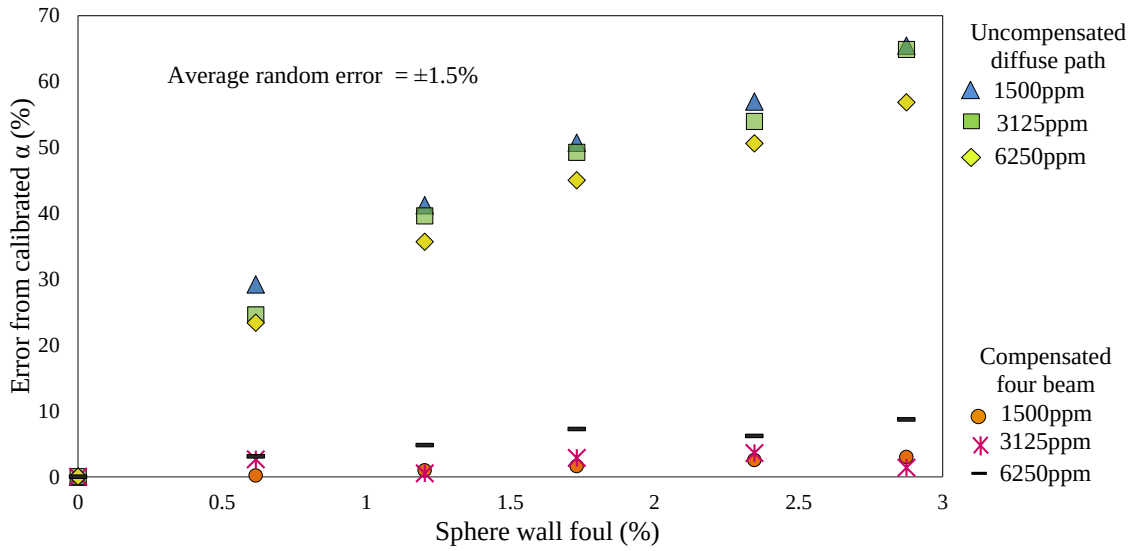

Figure 5.11: Percentage error as a function of both sphere wall contamination for different methane gas concentrations for compensated ratiometric scheme vs. a single uncompensated path (i.e. L_{12})

As seen in Figure 5.11, the percentage error in measured absorption coefficient was much greater for the unadjusted single diffuse path. For example, at 1500ppm, with no pathlength adjustment, contamination representing 1.2% sphere wall coverage gave a reduced absorption coefficient which had a percentage error of 41±1.5% from the calibrated value (which had no fouling). With the ratiometric scheme, this error was reduced to 1±1.5%. At the highest concentration of 6250ppm, with the most severe level

of contamination tested, 2.87% sphere wall coverage, the resultant errors amounted to less than 9% for the four beam compensation scheme, with the average error being 6%.

The errors in the compensated scheme increase both with increased levels of contamination and increasing concentration of gas. Addressing the increasing error with increasing sphere wall contamination first, it is proposed that this is due to a breakdown of symmetry between the two diffuse long pathlengths i.e. at high levels of light absorption by the fouling tabs they no longer have the same mean effective pathlength. This is discussed further in Section 5.4.4. Regarding the errors relating to concentration, it is proposed that the introduction of higher concentration samples into the sphere, whilst absorbing a proportional quantity of the radiation, additionally has an attenuating effect on the beams traversing the cavity, thus reducing the effective pathlength [20]. This is not accounted for in the current derivation however it is a predictable error and so it is envisaged that a further correction factor could be included to account for this.

5.4.3 Sphere window contamination

As mentioned in section 5.2.1, unevenly distributed contamination, or deposits with particle sizes of the order of the source or detector can introduce errors into the assumed proportionality between the direct and diffuse paths. With this consideration in mind, a preliminary experiment attempted to represent two particle sizes; millimetres e.g. 1-6mm, which would be equivalent to particles such as sand, metallurgical dust, fly ash or textile fibres, and much finer particles e.g. 0.1-50 µm, which would aim to represent a typical size for atmospheric dust, combustion related burning or saw dust. A supplementary experiment was performed at a later date than the previous error experiments to look at how each path (long and short) would be affected by particle build-up on the window. The setup was as in Figure 5.4, using two Hammamatsu InGaAs detectors (G11777-003P with cut-off frequency 600MHz) and amplifiers (Femto DHPCA-100 with potential cut-off frequency of 175MHz). These detectors and amplifiers had a higher bandwidth and gain than the Thorlabs detectors. The affected flux values are highlighted in Figure 5.12.

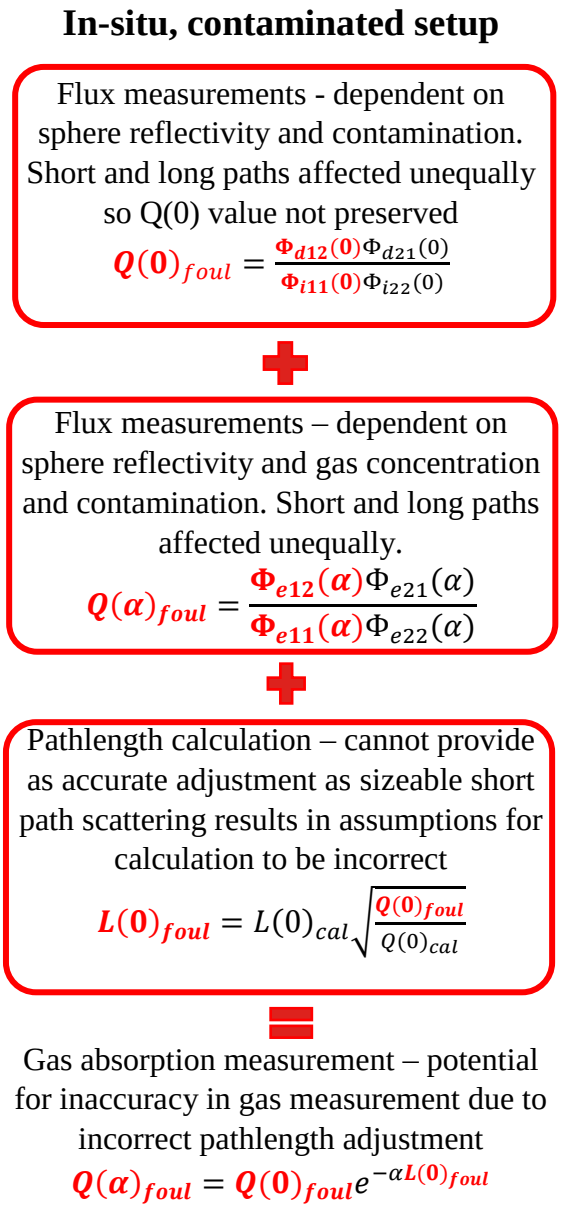

Figure 5.12: Sphere window contamination, contamination of the window causes a proportionally unequal reduction in the affected long (diffuse) and short (direct) path. As a result the Q(0) value is not preserved and is dependent on window contamination, and so the pathlength sum can't be as accurately adjusted.

The theoretical analysis shows that average window contamination may be compensated, i.e. contamination that is homogeneous across the full incoming laser beam. For the four beam implementation, there is also an implicit assumption that light striking the window will not be deviated from its initial direct path towards the opposite detector and into the diffuse path, or vice versa. To investigate these assumptions, contamination on the window was simulated using two microscope cover slips as seen in Figure 5.13. One was covered with a layer of crumpled plastic film, Figure 5.13(a), to

represent particulate contamination on the order of much less than the source or detector size which would provide low levels of light scattering. The other cover slide, as in Figure 5.13(b), was sprayed with grey paint to give a speckled effect on the millimetre scale, simulating heterogeneous particulate contamination on a scale similar to that of the beam diameter, i.e. 1s of mm. Each cover slide was placed at the S1 input port position and the resultant transmitted flux for the pathlengths, S1 to D1 and S1 to D2 were measured, looking at the change in transmission for each path.

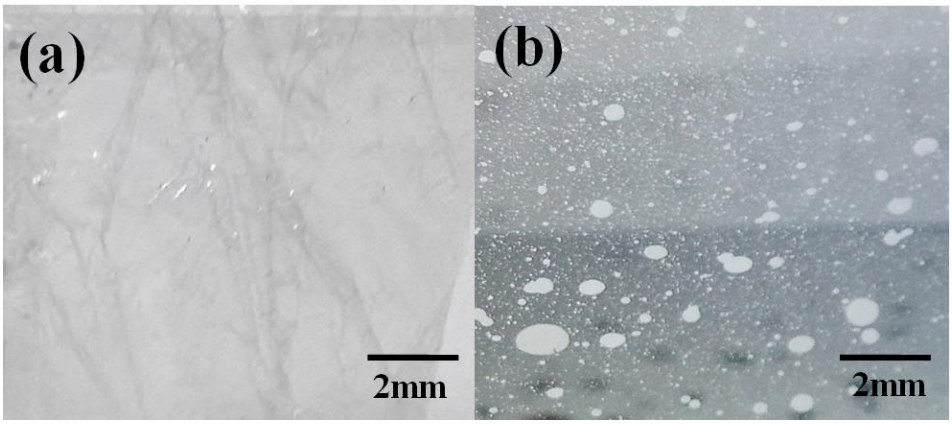

Figure 5.13: Particulate contamination on sphere window; To investigate low levels of scattering contamination, a plastic film was used as seen in (a), whilst a speckled cover slide was used to simulate heterogeneous particulate contamination of the order of the beam diameter as seen in (b)

The change in transmitted flux with window contamination was noted for the short and long path of S1, and the results were expressed in terms of percentage change in transmission, as seen in Table 5.3. The experiment was repeated three times and the errors represent the standard deviation. It might be expected that the transmission of both paths would decrease with contamination build-up on the window. As seen in Table 5.3, for the speckled paint, there was a large reduction in transmission for the direct (short) path however the diffuse (long) path experienced an increase in transmission. This occurred because, as well as a large proportion of the light being absorbed by the particles, some light was also scattered out of the direct (short) path onto the sphere wall and so actually contributed to an increased flux measurement of the diffuse (long) path.

Table 5.3: Effect of sphere window contamination on the light transmission for both short and long paths in terms of percentage change in transmission

	Plastic film		Speckled paint	
	500ppm	1000ppm	484ppm	1010ppm
Direct (short) path L_{11} (%T)	-29% ± 10	-28% ±11	-93% ± 1	-93% ± 1
Diffuse (long) path L_{12} (%T)	-5% ±2	-4% ± 2	10% ± 0.4	10% ± 1

In terms of the compensated setup for an integrating sphere, i.e. Figure 5.3, the mathematical derivation for pathlength adjustment assumes that changes in the short path fluxes are negligible. However as seen from the results in Table 5.3 this is not the case; the effect of window contamination is not predictable and heavily dependent on the particle size. In the case of the plastic film, a reduction in transmission was seen for both the direct (short) and diffuse (long) path, but it had a less severe effect on the short path than the speckled paint. As is evident from these results, when window contamination occurs, it disproportionately affects the direct (short) and diffuse (long) paths. This violates the assumption that the short and long path flux path measurements vary proportionality as stated for the traditional four beam case in Section 5.1.1.

To test the extent to which this type of contamination may affect the four beam compensation scheme, these percentage changes in transmission were applied to the source 1 long, Φ_{12} and short Φ_{11} paths of the previously measured data as detailed in the preceding section and reworked into the calculations as discussed in Section 5.4.2. The results are displayed in Table 5.3. It was found that for the smaller particulate contamination, i.e. using the plastic film, for a 1500ppm concentration of methane, the calculated effective absorption coefficient had an error of approximately 13%. In concentration terms, the concentration was underestimated to be approximately 1300ppm. For the larger particulate contamination, i.e. using the speckled paint, for a 1500ppm concentration of methane, the calculated effective absorption coefficient had an error of approximately 70%, severely underestimating the concentration to be approximately 430ppm.

5.4.4 Additional error sources

During the initial stages of implementation it was found that when trying to reconcile the theoretical assumptions with the experimental implementation there were some discrepancies between the two. A major challenge for this four beam setup was trying to account for how the light propagated once introduced into the sphere for both the short and long paths.

Expected transmitted flux Φ_d when using a recessed detector An experiment was carried out to confirm that, in the absence of gas, the expected transmitted flux Φ_d could indeed be calculated from knowledge of the sphere wall reflectivity and the incident flux, using equations 4.4 and 4.5. The experiment, using the setup as in Figure 5.4, compared the theoretical calculation of the expected exit flux for source 1 long Φ_{12} (diffuse) path, with an actual exit flux measurement for that path. The flux measurements were made using both the variable gain detector (Thorlabs PDA10CS) and the surface mount detectors (Hamamatsu G11777-003P).

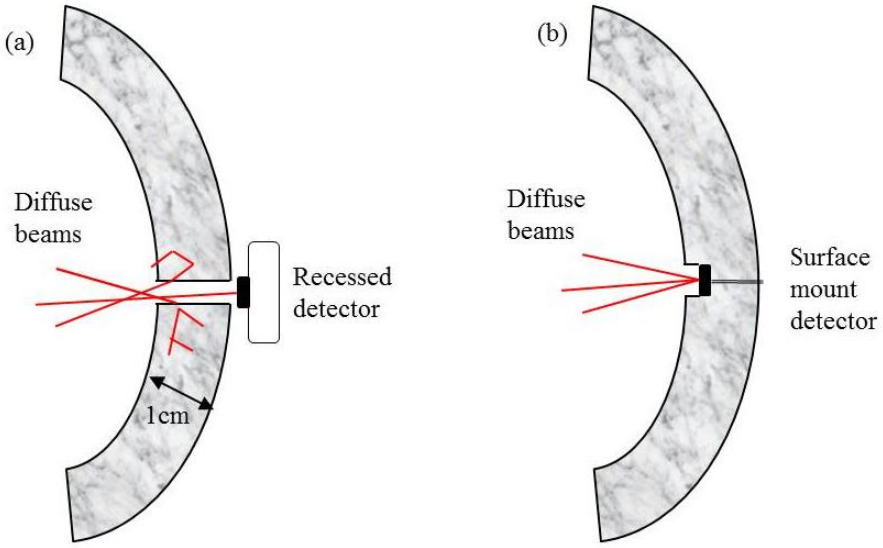

Figure 5.14: Recessed detector vs. surface mount detector. In the case of the recessed detector (a), there is the possibility for some exiting beams to re-enter the wall at the port opening whereas with the surface mount detector (b) more of the exiting beams are sampled with less potential for re-entry to the wall.

It was found that when the recessed variable gain detectors were placed at a port opening with a surface area of 0.79mm^2, the theoretically calculated exit flux appeared

to be overestimated, as seen in Table 5.4. The deep port adaptor meant that the detector was recessed from the surface of the inner wall by over a centimetre. The surface mount detectors had an active detector area of 0.3mm^2 but as the detector was embedded into the port adaptor, an area of the sphere wall was lost to the non-active area of the detector, approx. 1mm^2. When the surface mount detectors were used, the exit flux values were much closer to the expected theoretically calculated flux, and in fact underestimated in the theoretical calculation. It is proposed that this discrepancy occurs because for the theoretical calculation, it is assumed that the non-active surface area of the detector, i.e. ≈1mm^2, has 0% reflectivity when in reality the area would have some specular reflections of incoming beams.

Table 5.4: Effect of detector position on long path output flux value. There is a larger difference between the theoretical and experimental measurement for a more recessed detector

	Theoretical	Measured
Narrow port opening – 0.8 mm^2 active area, 0.79mm^2 port opening area (Incident flux 5.07mW)	25.4μW	0.07 μW
Surface mount detector – 0.3mm^2 active area, 1.28mm^2 non active area (Incident flux 3.52mW),	6.7 μW	17.3μW

It is concluded that in the case of the recessed detectors, as the output light passes through the 1 cm deep port opening, a portion of the light re-enters the wall of the opening, causing a reduction in the detected transmitted flux. In the case of the surface mount detectors, this does not happen as the detector is almost in line with the sphere inner wall. The word "almost" is used as the port containing the surface mount detector was recessed slightly so that the detector did not have a direct line of sight with the source. In the case of the four beam implementation where the variable gain detectors were used, this underestimated expected flux (due to light re-entering the wall) was taken as the expected flux measurement.

Theoretical pathlength vs experimental pathlength It was found that the theoretically calculated pathlength, using Equation 4.10, was consistently longer than the experimentally determined pathlength, using the method as described in section 5.3.1. For example, for the setup as in Figure 5.4, with a port fraction of 0.0077 and

quoted reflectivity of 0.987, the theoretical optical pathlength was calculated to be ≈1.62m whereas the experimental gas pathlength was measured as ≈1m. It was concluded that this could be due to a number of factors, such as the quoted sphere wall reflectivity value no longer corresponding to the actual reflectivity due to aging of the sphere wall, or in this case, tapering of the material to a depth of 2-3mm as it approached the port openings. Indeed the experimental data suggests an overall reflectivity of 97.5%, not 98.7% as quoted by the manufacturer. Additionally, as mentioned in Section 5.4.2, the presence of the gas itself has an attenuating effect on the light when in the non-linear regime of the Beer Lambert law. As a result of all of these effects, the pathlength calculation using the gas method will underestimate the optical pathlength value. The experimentally determined gas pathlength values for each long path were used for the four beam calculations as the end goal was to measure the gas concentration which would be related to the gas pathlength. Additionally the contamination that was introduced did not penetrate the sphere wall and so contamination could be accounted for through the gas pathlength.

Breakdown of symmetry with increased contamination As seen in Section 5.4.2, increased sphere wall contamination increases the resultant error. It was suspected that the assumptions of uniform and homogenous diffusion of the light were no longer holding at higher levels of contamination. To investigate whether the two pathlengths were equivalent at each stage of contamination, a mean effective pathlength for each diffuse path at each level of contamination was calculated, using the method for pathlength calculation as described in Section 5.3.1 and displayed in Figure 5.4(a). The results are plotted below in Figure 5.15, along with the percentage errors incurred in each corresponding gas absorption measurement. The error bars correspond to the standard deviation values of three repeat measurements.

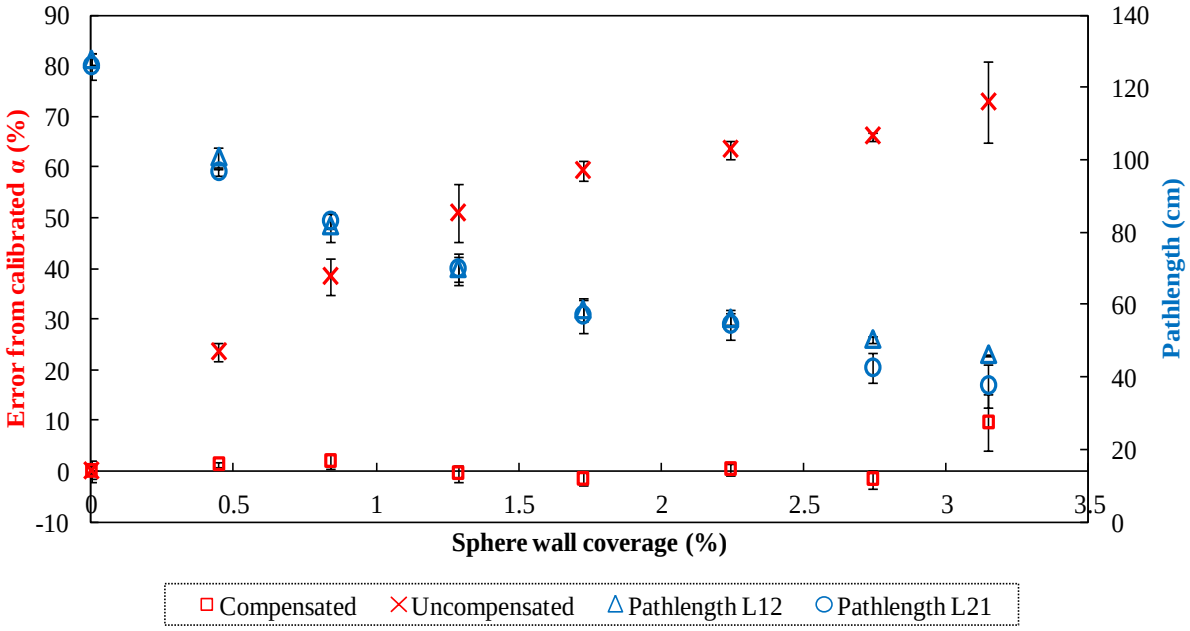

Figure 5.15: Effect of contamination on pathlength symmetry. At higher levels of contamination, the two long pathlengths diverge relative to one another (in blue) which causes a resultant increased error on the effective absorption measurements (in red)

As seen in Figure 5.15, for increasing levels of contamination the two pathlengths diverge relative to each other. For example, for 2.87% sphere wall coverage the diffuse long paths deviated from each other by approximately 6cm, whereas for lower levels, such as 1.2% the diffuse long paths deviated by approximately 1.5cm. This could suggest that at these levels the light may not be uniformly diffused and the integrating sphere relations break down.

First strike spot cannot be compensated The four beam compensation scheme has shown improved accuracy of gas absorption measurements in the event of sphere wall contamination. However it was supposed that the scheme may not be able to compensate for contamination on the area of the sphere wall where the incoming specular beam contacts i.e. at the first strike spot, in this case an annulus around the detector opposite each entrance aperture. To test this, an experiment, as in Figure 5.4 was used where a fouling tab (≈10x4mm) was placed at the first strike spot of laser source 2, i.e. at the detector 2 position. The effective gas absorption was calculated for a gas concentration of approximately 1000ppm. It was found that when the compensation scheme was applied as for the other sphere wall contamination in Section 5.4.2, the

resultant gas absorption measured was overestimated by approximately 40%. The long path measurements were looked at in isolation and compared with the results from earlier where the sphere wall contamination was introduced into the bottom of the sphere.

Table 5.5: Comparison of effects of two sphere wall contamination locations, firstly at a first strike spot and secondly on the bottom of the sphere.

Location of contamination	% drop in long path flux measurement (Φ_{12}) from calibrated	% drop in long path flux measurement (Φ_{21}) from calibrated	% error in absorption coefficient from calibrated α
At source 2 first strike spot.	12	63	40
At bottom of sphere wall	26	25	1.32

As seen in Table 5.5, the long path flux measurements reduced disproportionately for the incident where the first strike spot for source 2 has been contaminated. When compared with the sphere wall contamination where there is no interruption of the first strike spot the long path from source 2 to detector 1, i.e. Φ_{21} has reduced by over twice as much for the first strike spot contamination. This is probably due to the fact that at this location the incoming beam is a specular beam with a greater incoming power than for a diffuse reflection. However, the level of error is likely to be lower than the error that would result from similar levels of contamination present on the rest of the sphere sidewall, because after the first strike spot photons encounter the sidewall an average of M times before striking the detector. Thus, if contamination within the sphere is well distributed and not confined to the first strike spot, errors will still be reduced by use of the compensation scheme.

5.5 Discussion and future work

The research in this Chapter aimed to investigate a method that could account for potential deviations from calibration for an integrating sphere based gas sensor, for example as a result of sphere wall contamination. The approach taken is a new modification of the so-called four beam ratiometric compensation scheme, as used in water analysis, combined with use of the integrating sphere relations. The following

sections discuss both the achievements that were made, including a mathematical derivation that can adjust for pathlength change, as well as the limitations, such as sphere window contamination.

5.5.1 Benefits of and improvements to work to date

Compensation for component variation One of the cited advantages of the original four beam technique was compensation for component variation and it was hoped to maintain this for a sphere adaptation. As seen in Section 5.4.1, for the integrating sphere adaptation, a reduction in intensity of source 1 was compensated for to within a 1% error. This showed that this configuration did not contribute a further error to the absorption measurement, even for high concentrations of gas. The construction of the Q expression dictates that four beam passes are needed so that all potential component variation can be compensated for i.e. whether at source or detector position. However this does introduce a requirement for two sources and two detectors which increases complexity as well as the port fraction due to the additional port openings. For future embodiments, it is intended to construct a two beam setup where a single source and two detectors are used so that only one short(direct) path and one long (diffuse) path are considered. This is possible as the pathlength adjustment calculation for sphere wall contamination can be done without the requirement for four beams. This would of course mean that some component variation is not accounted for, i.e. detector fluctuations, however given that other sources of variation, such as sphere wall or window contamination contribute a much greater error, the advantages of reducing the number of components, i.e. reduced cost, or ease of manufacturing, may outweigh this loss.

Compensation for sphere wall contamination The initial focus for the mathematical derivation was to be able to differentiate whether changes in the transmitted flux occurred as a result of the presence of an absorbing gas or contamination of the system, or both. It was shown both theoretically and experimentally that the fractional change in the Q(0) expression could be used to adjust the pathlength sum, allowing for a gas absorption measurement to be made even in the presence of sphere wall contamination, with only a minor resultant error (an average of 6% for the contamination levels tested) due to the presence of contamination. When it

came to experimentally implementing the mathematical derivation it was found that there were additional factors that could contribute further uncertainty to the measurement. These included an increase in errors for increasing contamination, as well as for increasing gas concentration.

Regarding the increasing error with increasing contamination, it was concluded that the error occurred as a result of divergence of the two long pathlengths relative to each other. This suggests that at these levels of contamination the light may not be uniformly diffused and consequently this may have implications for alignment tolerances. On the note of the higher gas concentrations, the resultant errors increased relative to the concentration which suggests a predictable error. Future work would look to be able to factor this in, possibly through use of the short path as an indicator of the fact that there is a higher concentration present.

The other sphere wall element that was not compensated for was the first strike area, an annulus around the detector opposite each entrance aperture, as demonstrated in Section 5.4.4, when the first strike spot for source two was contaminated. Contamination at this point did not affect the direct flux but did reduce the diffuse long path flux of source 2, giving an error that could not be compensated for with pathlength adjustment. Further investigation showed that the long path flux measurements for source 1 and 2 reduced disproportionately for the incident where the first strike spot for source 2 has been contaminated. This disproportionality could, in practice serve as an indicator of first strike spot contamination specifically. The size of the fouling tab used meant that quite a substantial portion (approximately 40%) of the source 2 first strike spot was contaminated. It is unknown whether this scenario would be likely in-situ and so future work would aim to investigate this.

On that note, the method of inducing contamination, i.e. using relatively large fouling tabs as seen in Figure 5.9, was quite a severe simulation of contamination, but was done in this way so that any observed effects could definitely be attributed to the contamination induced, as well as to allow for easy removal of induced contamination without disrupting the alignment. In reality it is expected that for any in-situ implementation of this technique, a particulate filter would be attached to the gas inlet so that if any particulates enter the sphere they would be on the order of microns.

Potential sources of contamination include airborne dust particles that have not been captured by sampling line filters, or condensation of water or oils present in sample gas streams. One aspect of this compensation scheme that has not been investigated is the long term accuracy and repeatability of this type of compensation scheme. Future work would aim to test this scheme in a more representative environment, i.e. use of smaller more dispersed particulates and over a longer period of time, e.g. a month. Some factors to consider would include what level of contamination is acceptable before the detection limit is compromised and how long does it take for the sphere to accrue this level of contamination.

Sphere window contamination The contamination source representing the greatest cause for concern, as was evident from the resultant errors, was the sphere window contamination. The magnitude of the error was very dependent on how much the short path flux deviated from the calibrated setup as it affected both the pathlength adjustment calculation and the gas measurement itself. In practice, as the direct (short) path flux is very sensitive to contamination build-up on the window, it is envisaged that monitoring of the direct (short) path flux change over time would provide a warning to alert the user to appreciable contamination on the windows.

Furthermore, from an alignment point of view, though the beam divergence for each path needs to be controlled, the symmetrical setup means that the alignment of the system itself is not complex as long as the beam divergence is controlled. It is envisaged that the diverging lenses can be secured with custom adaptors and thus a "plug-and-play" type system should be achievable. What this means is that, as the alignment would be fixed by the component adaptors, even if appreciable window contamination occurred, the windows could be removed, cleaned and replaced in-situ by the operator without the need to return the sensor to the manufacturer for recalibration. This would be preferable to the need to clean or recalibrate the sphere, which would be the alternative for the uncompensated scheme. Ideally to reduce the necessity for this, as mentioned before, a particulate filter would be included at the gas inlet. Further investigation needs to be carried out to look at how changes in transmission due to window contamination translate in terms of errors with absorption coefficient calculations for the four beam setup. For particles with dimensions of the order of the crumpled plastic film, depending on the application, the resultant error may be

acceptable. It is expected that larger particles on the order of millimetres would contribute an unacceptable error. Indeed a similar issue exists for more conventional four beam systems[173] which are nevertheless used successfully in industrial applications subject to fouling.

Future work On a general note about the four beam technique, as cited for the traditional four beam configuration[171], having the ability to measure a wide range of concentrations due to the option of variable gain would provide an advantage for absorption measurements. The availability of short path measurements could be useful for higher concentrations where otherwise, saturation of long path signal may occur. At the other end of the scale, application of modulation techniques, as described in Chapter 3, is a possibility to achieve greater detection capability reaching low ppm and possibly even ppb levels. In terms of the ratiometric scheme, it may be possible to implement this in a cubic cavity. This would ease the complexity in cavity manufacture and possibly allow for easy construction and deconstruction of the cavity if contamination has occurred. From a calibration point of view it is envisaged that the pathlength calculation technique that will be described in Chapter 6 may be combined with this technique to allow for pathlength calculation without the requirement for a reference gas cell. This would also allow for an optical as well as gas pathlength to be calculated, which would aid with the intended long term measurement accuracy investigations, as mentioned in the sphere wall contamination section of this discussion.

5.5.2 Summary

In this chapter a four beam ratiometric scheme for an integrating sphere based gas cell was presented that, in the event of sphere wall contamination, could be used to adjust the pathlength. In this way gas absorption measurements can continuously be made without needing to calibrate or remove and clean the sphere.

The chapter summarised the background to the original four beam compensation scheme on which this scheme is based and described the proposed adaptation to an integrating sphere setup. A mathematical derivation was provided showing how the scheme is intended to work. To demonstrate the technique, methane gas was detected at concentrations from 0 to 6250ppm using tunable diode laser spectroscopy at 1651nm, with increasing levels of sphere wall contamination from 0 to 2.87% sphere wall

coverage. For example, for a 5.08cm diameter sphere, a 1500ppm concentration of methane with fouling over an area representing 1.2% of the sphere wall, gave a reduced absorption coefficient which had an average percentage error of 46% compared with the calibrated value (which had no fouling). With the ratiometric scheme, this error was reduced to 1%. There were some factors that contributed further uncertainty, namely errors that increased with increasing levels of contamination, due to a loss of assumed symmetry between the long paths. Increasing concentrations of gas also produced an increase in error, attributed to the attenuating effect of the gas. Contamination of the first strike spot caused a substantial error in absorption measurements and thus represents the greatest concern for sphere wall contamination. It is the position where the incoming specular and thus relatively (to the diffuse reflections) intense, beam pass first contacts the wall. The disruption of the incoming beam greatly affected subsequent diffuse reflections and could not be compensated using the pathlength adjustment as this pass is not accounted for in the calculation. Further investigation is required to solve this issue; one possibility may be to monitor the difference between the two diffuse path fluxes, Φ_{12} and $\Phi_{21,}$ as an indicator of failure.

Additionally other cited advantages of the traditional four beam setup were tested, namely component variation and sphere window contamination. The scheme compensated well for component variation, i.e. a 0.38% error in Q(gas) expression resulted instead of a potential 4.5% error, when compared with the calibrated value. Preliminary experiments looked at sphere window contamination, using two particle sizes, i.e. millimetre on the order of the beam diameter and a much finer particle size, i.e. much less than the detector or source size. The results indicated that, depending on the particle size, this type of contamination may contribute a sizeable deviation from the originally calculated pathlength in the system.

In the course of this study it was necessary to develop repeatable methods for simulating different types of contamination without causing permanent changes to the sphere. This was achieved using adhesive tabs as described in Section 5.4.2, allowing for different potential contamination locations to be tested. On a more general note this could potentially provide an experimental basis for comparison of different techniques.

The contribution of the various contamination sources are summarised in Table 5.6.

Table 5.6: Summary of the various contamination scenarios tested, and their effect on the resultant absorption measurement when compensated for and uncompensated.

Sphere characteristics	
Diameter	5cm
Sphere reflectivity	97.5% experimentally (manufacturer quoted as 98.7%)
Effective optical pathlength	≈100cm long path, 5cm short path

Error sources	**Effect of error**	**Compensated (%error) @1500ppm**	**Uncompensated (%error) @1500ppm**
Sphere wall contamination	Effective pathlength of long path reduced, output power is reduced. Mathematical derivation corrects pathlength to new "contaminated" scenario	3% error in gas measurement with 2.87% sphere wall contamination	65% error in gas measurement with 2.87% sphere wall contamination
Sphere window contamination	Output power tended to: Decrease in both short and long path for <<mm scale contamination Increase in long path and decrease in short path for mm scale contamination	mm particulate contamination 70% error <<mm particulate contamination 13% error	Not calculated as it could be determined qualitatively that the result would yield a large error.
Component variation i.e. laser/ detector fluctuation	Measured output power will differ. Four beam setup cancels this out ratiometrically	1.4%	1%
First strike spot	Corresponding long path throughput reduced, and disproportionately to other long path throughput	63% reduction in corresponding long path 12% reduction in other long path	

For future work, there are many further avenues to explore in terms of detection capability, e.g. modulation, and embodiments of the ratiometric scheme, e.g. a two beam setup or even a cubic structure. In summary, the adapted four beam configuration for an integrating sphere has the potential to provide a means of pathlength calibration for continuous, in-situ, operation.

6

Phase detection techniques for pathlength calibration

"FPGAs meet critical timing and performance requirements with parallel processing and real-time industrial application performance, permitting greater system integration and lower development cost"- EE times[174]

The motivation for this work stemmed from a desire to be able to measure the effective pathlength of the sphere in situ and without the requirement for using a reference gas cell for the initial calibration. The decision to use the techniques as described in the proceeding sections came about following a conversation with a fellow researcher, Dr. Thomas Kissinger, who has been researching range resolved interferometric signal processing based on code division multiplexing[175], [176]. Here, return signals from multiple interferometric signal sources can be separated based on their time of flight, through the encoding of the outgoing light with a pseudo-random digital code. It was hypothesised that some aspects of this signal processing scheme could be incorporated into an integrating sphere setup to achieve real-time measurement of the sphere effective pathlength.

It was envisaged that the technique would work in a similar way to that of phase shift cavity integrating cavity output spectroscopy (PS-ICOS), as described in Section 2.3.5, where a measured phase shift could yield information about the reflectivity (and thus pathlength) of the sphere. To provide a pathlength calibration in distance units a comparison of the phase shift for the sphere output signal (with unknown pathlength) could be compared to that of the phase shift for a separate measured signal with a known length. Unlike some PS-CEAS applications, the motivation was to measure a pathlength rather than trace gas concentrations and so the same measurement precision would not be required. For example, it can be necessary to have longer integration times (on the order of a few minutes) when trying to achieve ppb detection limits[75],

whereas measurements of pathlength do not demand the same sensitivity e.g. measurement uncertainties of ±1cm could be acceptable.

An advantage of employing this scheme is the enhanced resolution achieved through implementation of high frequency modulation of the intensity. The achievable frequency range far exceeds the limits of standard laboratory lock in amplifiers (1mHz - 102kHz) and is made possible due to the high clock frequency (150MHz) of the hardware used, i.e. a field programmable gate array (FPGA). An additional advantage of using this approach is that the signal generation and processing are carried out by the FPGA, and so the modulation and demodulation are synchronised. Thus, in effect, it works much like a lock in amplifier, facilitating measurement of weak signals in a potentially noisy environment. The use of this type of hardware gives a lot of flexibility in terms of the bandwidth selection i.e. harmonics of the modulation frequency can be measured. This provides an advantage over techniques like OA-ICOS (Section 2.3.5), where output power is sacrificed to allow for the use of lower bandwidth electronics, or the ICRDS (Section 2.3.4) where high reflectivity material and high bandwidth electronics have to be used to achieve sufficient resolution of the exponential decay.

As an additional step, it was envisaged that by simultaneously applying a lower frequency ramp waveform, as utilised in Chapter 5, an off gas line, as well as on gas line measurement could be made, to record pathlength change due to contamination only, thus maintaining knowledge of the sphere pathlength. Due to time constraints, implementation of the lower frequency ramp waveform for spectroscopy was not tested and so pathlength calibration was investigated at the gas line wavelength only.

To test the signal processing scheme in an integrating sphere setup, two different types of signal generation were used to interrogate the system where the intensity was modulated. The first signal used is a straightforward high frequency sinusoidal modulation of the incoming signal, and the second is a pulsed modulation, which is introduced through use of a digital code known as a maximum length sequence (MLS). The first section of this Chapter describes the signal processing scheme itself as designed and built by Dr. Kissinger, the hardware used, and the considerations for signal optimisation and data analysis. The second section describes the sinusoidal

modulation approach, including the considerations for design optimisation such as the compromises between sensitivity and gain. The experimental results for both a single pass setup and multiple pass sphere setup are shown, introducing some of the issues with throughput and interference that need to be addressed in the future. The third section describes the pulsed modulation approach, including the theory behind the code used and some experimental design strategies for signal optimisation. The results are presented in a similar format as for the sinusoidal modulation with a single pass setup and multiple pass setup considered. The fourth and final section describes the limitations of both techniques; the discussion for both has been combined as many issues, such as interference and throughput, are common to both techniques.

Dr. Kissinger's contribution to this work has been;

- Configuration and assembly of the FPGA with appropriate signal converters to facilitate generation and processing of signals.
- Creation of programming code to enable control of FPGA and processing of acquired data.
- Collaborated on mathematical derivation, along with Dr. Hodgkinson as detailed in Section 6.1.2.

The remaining aspects of the work, i.e. the experimental design and data analysis as described in this Chapter are the work of the author.

6.1 The signal processing scheme

As mentioned in the introduction, the signal generation was carried out by the same piece of hardware, a field programmable gate array (FPGA), which ran at a clock frequency of 150MHz. A more detailed overview of how the FPGA works is described in Appendix A. The signals were post-processed on a PC to facilitate greater flexibility with the experiment optimisation and measurement. Due to bandwidth limitations the frequencies that were processed on the PC were lower frequency integer factors of a higher modulation frequency i.e. 150MHz. The specific values for the sinusoidal and pulsed modulation techniques will be discussed later in the relevant sections

The general setup applied to both modulation techniques is shown in the schematic in Figure 6.1. The specific setups will be discussed in more detail when the experimental implementation for each technique is described in Sections 6.2.1 and 6.3.2.

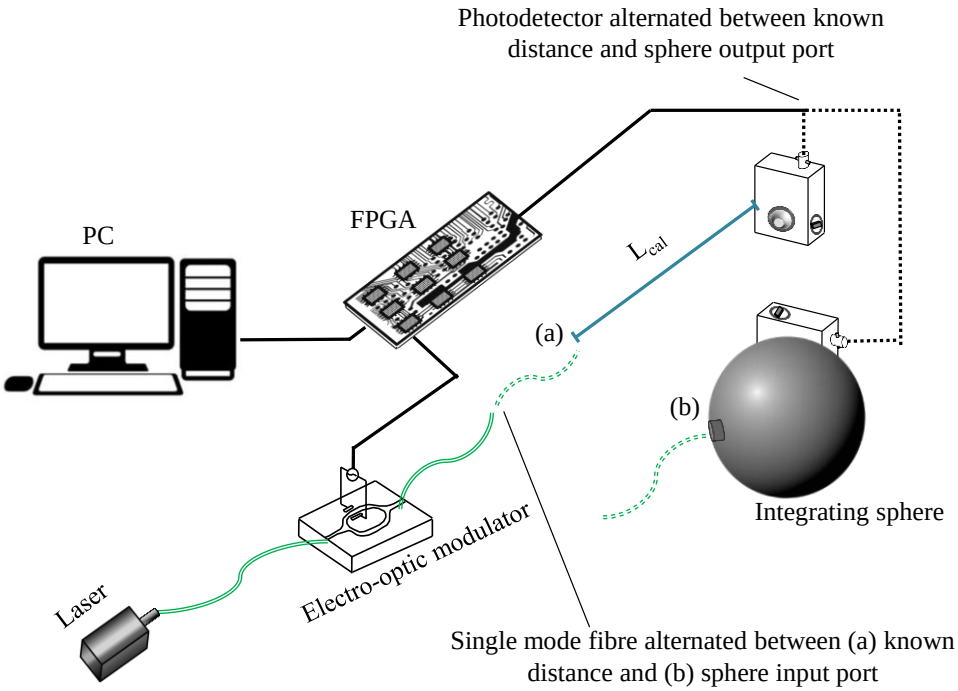

Figure 6.1: General setup: Light emitted from the laser diode is intensity modulated using an electro-optic modulator. The photodetector is initially placed at a known distance, L_{cal} from the fibre output and a measurement is made. Subsequently it is placed at the sphere output port while the fibre output is placed at the sphere input port and another measurement is made. The photodetector signals are acquired using the FPGA and a sphere pathlength is calculated by processing both signals on a PC.

As seen in Figure 6.1, light emitted from the laser diode was intensity modulated using an electro-optic modulator (EOM), driven by the FPGA which was directed by the PC program. The single mode fibre output from the EOM was first placed at a position in free space a known distance from the photodetector and the resultant phase shifted signal (relative to the phase angle of the inputted signal) was acquired by the FPGA and processed by the PC. The fibre was then placed at the integrating sphere input port, whilst the photodetector was placed at an exit port orthogonal to the input port and that phase shifted signal was measured. Both signals were processed by the PC and a resultant sphere pathlength was calculated by comparison of the phase difference between the two signals. The following sub-sections provide a step by step description

of the role of each component in the signal processing scheme and how the phase signals were generated and processed.

6.1.1 Signal generation and acquisition

Signal generation was initiated by a PC program, allowing for parameters such as the digital code length (for pulsed modulation) or averaging time to be set. Depending on the programmed commands (in Python programming language), the FPGA generated either a pulse or sine waveform. An initial phase angle θ_i was recorded by the FPGA (derived from the FPGA internal counter) as a point of reference for subsequent measured signals. The waveform generated by the FPGA was outputted to the electro-optic modulator (EOM) which produced intensity modulation of the incoming beam, as seen in Figure 6.2.

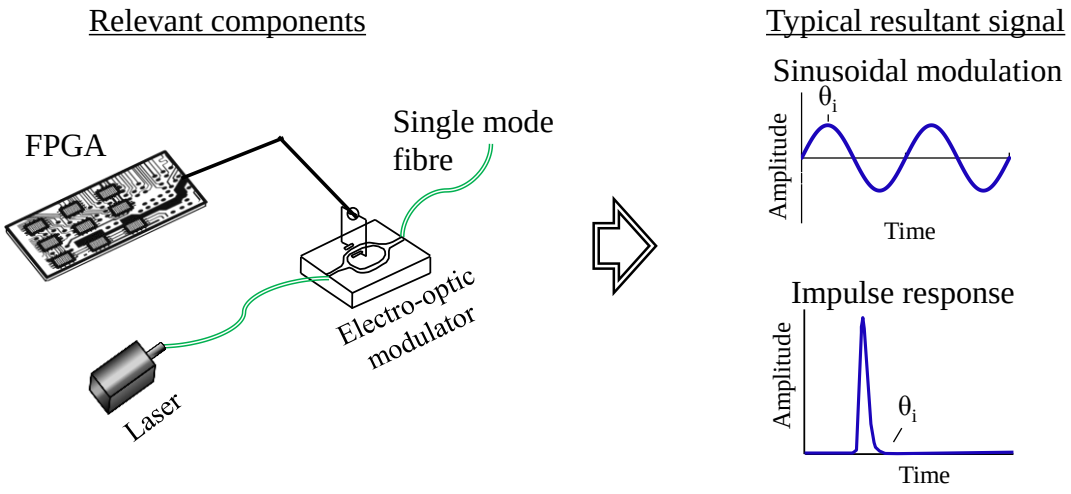

Figure 6.2: The waveform generated by the FPGA is outputted to the electro-optic modulator producing intensity modulation of the incoming beam

The fibre output of the modulated beam was then placed at the relevant locations to make pathlength measurements. For a single pass the fibre output was placed a certain distance (in free space) from the photodetector and a measurement was made as in Figure 6.3 (a). For an integrating sphere the fibre output was placed at an input port of the sphere and the photodetector was placed at a port orthogonal to the input, as in Figure 6.3 (b).

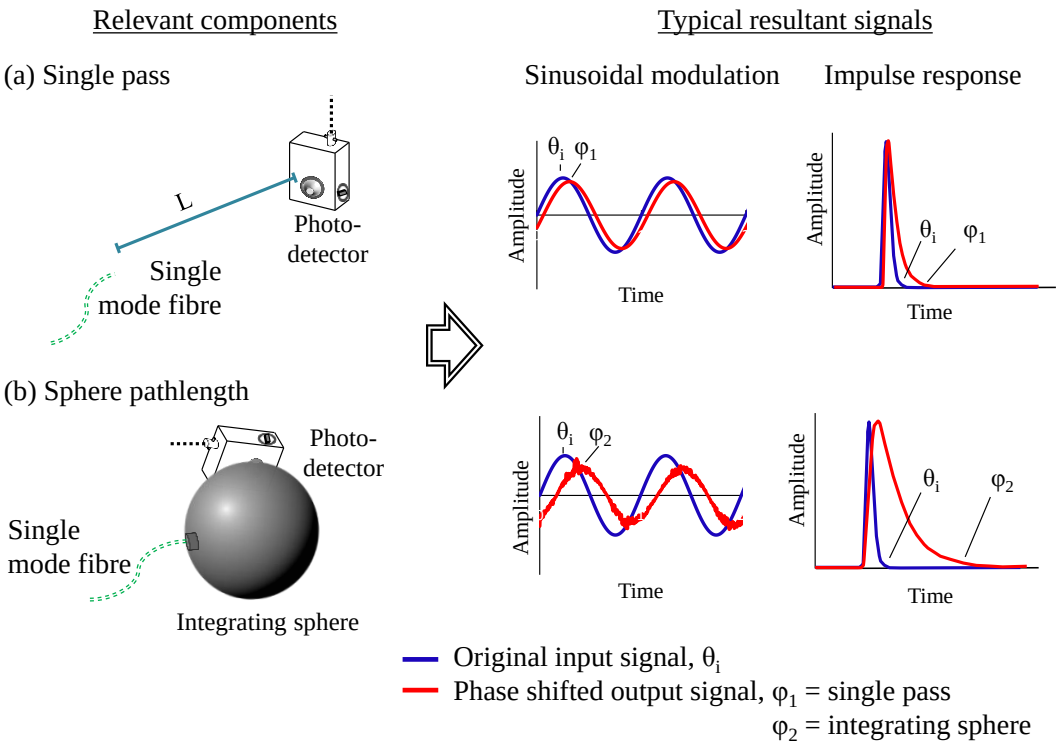

Figure 6.3: Measurement of the phase shifted output signal for (a) a known length and (b) the integrating sphere unknown pathlength.

For the sinusoidal modulation the sine waveform will be shifted relative to the original input signal, the extent of which is related to the distance from the fibre output to the photodetector. The output signal from pulsed modulation has an impulse response that resembles a "stretched pulse", the extent of which will again depend on the distance that the light has travelled before reaching the photodetector. The detected signals were transmitted to the FPGA where they were averaged and the phase angles φ_1 and φ_2 were recorded i.e. relative to the original input phase angle θ_i as logged by the FPGA. The data was transferred to the PC for further processing.

6.1.2 Data analysis

The raw data input from the FPGA comprised time varying signals and so the signals were converted to the frequency domain to extract the phase information at frequencies of interest i.e. harmonics of the modulation frequency. For the sinusoidal modulation technique, the waveform corresponded to a sine wave at a single frequency as seen in Figure 6.4 (a). The signal was Fourier transformed and the phase and amplitude at that frequency determined. Multiple frequencies were recorded consecutively so that results

could be compared to the pulsed modulation technique where a single measurement comprised a range of frequencies. The resultant phase shifts were plotted against frequency for both techniques, as seen in Figure 6.4(c) and (f)

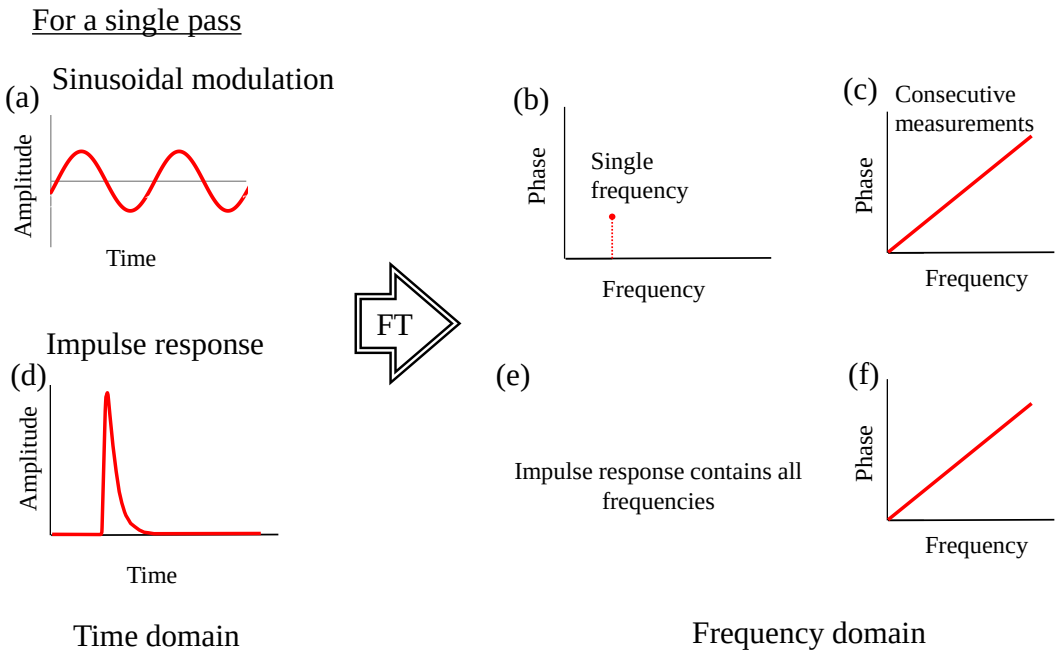

Figure 6.4: The raw data inputs for both techniques are time varying signals i.e. (a) and (d). To extract the phase information, the signals are Fourier transformed (FT) into the frequency domain i.e. a single frequency (b) and all frequencies (c) and (f). Note: figure (e) does not contain a single frequency plot as the impulse response contains all frequencies already.

For a single pass at any given length, the phase varies linearly with frequency, with the phase shift increasing at higher modulation frequencies. For an integrating sphere the effective pathlength is derived from the integration of multiple beam passes of multiple lengths. These passes have varying phases and amplitudes which overlap extensively. As a result, the overall phase shift that is measured exhibits a different relationship to the frequency, dependent on the extent of interference amongst the beam passes, as seen in Figure 6.5. The effective pathlength of an integrated sphere unlike a typical single pass is arrived at by considering the statistical distribution of the light in terms of the number of successful beam passes and their propagation. With increasing interference and cancelling among these beam passes it could be expected that the achievable effective pathlength would reduce as a result.

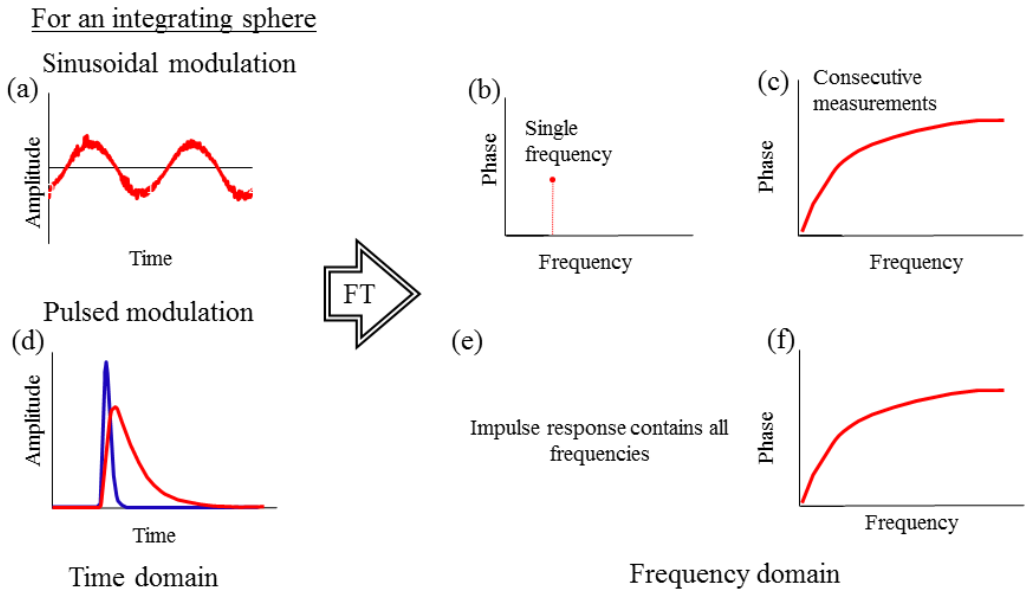

Figure 6.5: Resultant signals for an integrating sphere: the raw data inputs are time varying signals i.e. (a) and (d). In the frequency domain i.e. (c) and (f), the phase shift and frequency of detection relationship varies depending on the extent of overlap of beams. It is thought that at higher frequencies the measured overall phase shift is less than for a single pass due to increased beam overlap resulting in indistinguishable phase shifts between beam passes.

In order to understand the relationship between the overall phase shift in a sphere and modulation frequency for an integrating sphere, an analytical model was derived in collaboration with Dr. Kissinger and Dr. Hodgkinson as follows.

For each beam pass the signal as a function of time y(t), will have the form.

$$y(t) = I(\sin 2\pi\Omega_0 t + \Delta\varphi_t) \qquad 6.1$$

where I is the intensity of the signal and Ω_0 corresponds to the modulation frequency of detection. $\Delta\varphi_t$ corresponds to the phase shift of the sinusoidal function from its origin i.e. t=0, to its position at some elapsed time t and can be expressed either in terms of time or distance as

$$\Delta\varphi_t = 2\pi\Omega_0\Delta t = \frac{2\pi\Omega_0 L_t}{c} \qquad 6.2$$

where L_t is the corresponding effective pathlength at that elapsed time t. This equation applies for a single path measurement where the optical pathlength difference varies linearly with the phase shift of a sinusoidal function.

As well as this fundamental relationship of phase shift and frequency, pathlength calculation for an integrating sphere has to take into the account how the light is distributed in the sphere. Thus the measured phase shift that is used to calculate the integrating sphere pathlength is an integration of multiple sinusoidal functions of varying phases and amplitudes, dependent on how long the photons have spent within the cavity before being measured. The photons that make more passes within the cavity, and which results in a longer pathlength interval, will have a large phase shift but reduced amplitude due to reflectivity losses with each subsequent pass.

Thus to calculate the overall phase of all of these beam intervals, the integral of the function y(t), Equation 6.1, for the beam pass intervals can be denoted by

$$y(t) = I_{dL} \exp\left[i(2\pi\Omega_0 t + \Delta\varphi)\right] dL \qquad 6.3$$

Note Equation 6.1 is expressed as a complex exponential function here.

As described in Section 4.2, the intensity of the measured signal, at time t, $I_{dL,}$ will decay exponentially, the rate of which will be proportional to the sphere wall reflectivity

$$I_{dL} = I_0 \exp^{\frac{-t}{\tau}} \qquad 6.4$$

where I_0 is the initial signal intensity at time 0, t is the elapsed time, and τ is the decay constant as described in Section 4.2. For small port fractions the decay constant can be expressed as

$$\tau = -\frac{L_{sp}}{c}\left(\frac{1}{1-\rho}\right) \qquad 6.5$$

where ρ is the sphere wall reflectivity and c is the speed of light. L_{sp} corresponds to the average length of a single pass across the sphere and is given as 2D/3, where D is diameter of the sphere. It was seen in Section 4.2 that for low or zero absorbance α and where the apertures are very small (f<<1), the effective pathlength L_{eff}, is of the order

$$L_{eff} = \frac{L_{sp}}{(1-\rho)} \qquad 6.6$$

and thus the decay constant can be expressed as

$$\tau = \frac{-L_{eff}}{c} \tag{6.7}$$

Substituting this back into equation 6.4 gives the expression for the intensity at elapsed time t (in terms of distance/pathlength) corresponding to a beam pass interval dL as

$$I_{dL} = I_0 \exp^{\frac{-L_t}{L_{eff}}} \tag{6.8}$$

Equation 6.8 and 6.2 are then are substituted into the integral function, equation 6.3 to give

$$y(t) = \int_0^{\infty} I_0 \exp^{\frac{-L_t}{L_{eff}}} \exp\left[i(2\pi\Omega_0 t + \frac{2\pi\Omega_0 L_t}{c}) \right] dL_t \tag{6.9}$$

which becomes

$$y(t) = \frac{I_0 \exp^{2i\pi\Omega_0 t}(c^2 + 2i\pi\Omega_0 L_{eff} c)}{(4\pi^2 L_{eff}^2 \Omega_0{}^2 + c^2)} \tag{6.10}$$

The final signal, y(t) will have the form

$$y(t) = I \exp\left[i(2\pi\Omega_0 t) \exp(i\Delta\varphi) \right] \tag{6.11}$$

Thus, considering all beam pass intervals, equation 6.11 can be equated to equation 6.10 giving

$$I \exp(i\Delta\varphi) = \frac{I_0(c^2 + 2i\pi\Omega_0 L_{eff} c)}{(4\pi^2 L_{eff}^2 \Omega_0{}^2 + c^2)} \tag{6.12}$$

Looking at the magnitude and phase components individually and expressing them in terms of their real and imaginary parts gives

$$I = \frac{I_0 c}{\sqrt{4\pi^2 L_{eff}^2 \Omega_0{}^2 + c^2}} \tag{6.13}$$

and

$$\Delta\varphi = \arctan\frac{2\pi\Omega_0 L_{eff}}{c} \qquad 6.14$$

Finally substituting equation 6.14 into the phase difference equation 6.2 the actual effective pathlength at time t, L_t becomes

$$L_t = \frac{c}{2\pi\Omega_0}\arctan\frac{2\pi\Omega_0 L_{eff}}{c} \qquad 6.15$$

The first fraction of the equation accounts for the fundamental change in phase shift which varies linearly with frequency while the second fraction accounts for the overall phase shift of the effective pathlength of the sphere, which is an integral of multiple beam passes and varies as an arctangent function with increasing frequency.

To demonstrate this graphically a typical output over a range of frequencies is shown in Figure 6.6 for both a single pass and multipass derived pathlength. The delta phase Δφ measurement varies with varying frequencies, i.e. linearly for a single pass and as an arctangent function for an integrating sphere.

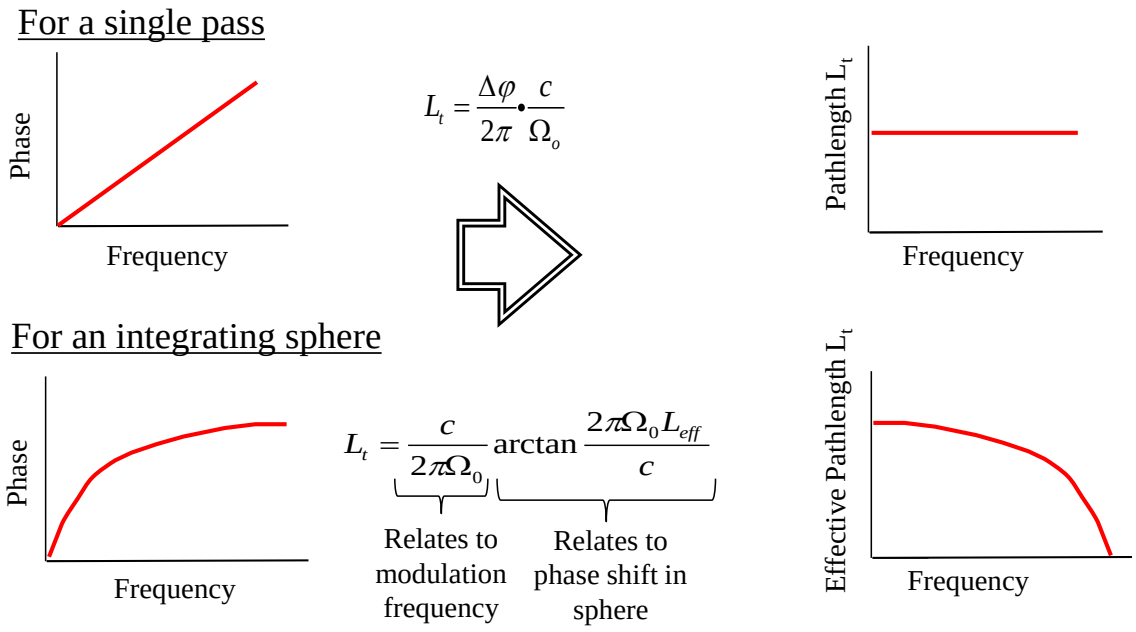

Figure 6.6: Pathlength calculation for a single pass and the multipass derived integrating sphere pathlength. For a single pass, the phase varies linearly with frequency whilst for multiple passes as in the integrating sphere, the phase varies as an arctangent function with frequency.

As seen in Figure 6.6, the phase varies with frequency as an arctangent function, giving a pathlength value that is constant at all frequencies. The data will be discussed in more detail in the relevant sections for each technique.

6.2 Sinusoidal modulation

High frequency modulation (MHz-GHz) has been applied to some gas sensing applications[177]–[179] however the requirement for fast detection components and more sophisticated demodulation and filtering means that often wavelength modulation spectroscopy at lower frequencies (kHz-MHz) is the preferred option. This technique hopes to alleviate some of these requirements through use of the signal processing scheme as detailed in the previous section.

Due to bandwidth limitations the frequencies that were processed on the PC were integer multiples (i.e. harmonics) of a base frequency rather than at the clock frequency of 150MHz. The base frequency F_b, was calculated by dividing the clock rate of 150MHz by the number of samples that were acquired per second during each cycle of the measured signal, e.g. 128 samples/s. So, for example with an acquisition rate 128 samples per second the resultant base frequency would be 1.172MHz and thus frequencies of interest could include integer multiples such as 2.344MHz and 3.516MHz.

In order to quantify the pathlength in terms of distance an additional calibration step was undertaken to convert the phase shift to these units. The resultant phase shift φ_{cal}, for a known pathlength was measured, in the same way as seen in Figure 6.3. The phase shift was then measured for the unknown pathlength e.g. integrating sphere φ_2 or single pass φ_1. The unknown pathlength could then be quantified in length units using Equation 6.2 or 6.15 (for integrating sphere) for phase difference, where $\Delta\varphi$ (in radians) corresponds to the phase difference between the known pathlength phase shift φ_{cal} and the unknown pathlength phase shift (i.e. $(\varphi_{cal}-\varphi_n)$, where n=1 or 2).

6.2.1 Experimental setup

For this particular implementation of the technique, as illustrated in Figure 6.7, a 1651nm distributed feedback (DFB) fibre pigtailed laser (NTT Electronics corp. NLK 1U5EAAA) was used with a typical output power of 20mW at a bias current of 100mA.

Its temperature was controlled at 14.5°C so that the wavelength was tuned to the methane gas line at 1651nm. The single mode fibre pigtailed laser was connected to a polarisation maintaining optical fibre (Corning HB1500T aligned along the slow axis) which in turn was connected to an electro-optic intensity modulator, EOM, (Lucent Technologies 2623-NA). The modulator output fibre was connected to a 90:10 fibre coupler (Newport F-CPL-S22151) where 90% of the light was directed to the sphere/cell of interest and the remaining 10% was connected to an optical spectrum analyser, OSA, (Yokogawa AQ6370C) so that the wavelength and power output could be monitored.

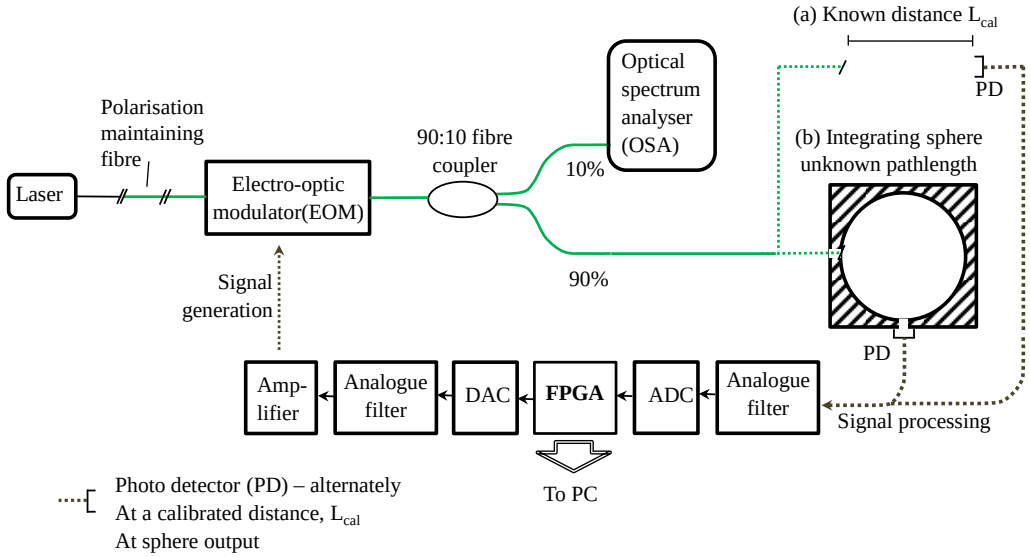

Figure 6.7: Setup for sinusoidal intensity modulation using signal processing as described in Section 6.1. An optical spectrum analyser is used to monitor the wavelength of the light.

The modulation was generated as detailed in Section 6.1.1, where the signal from the FPGA (Altera Cyclone IV on Terasic DE2-115 board) was transmitted to the DAC (Altera data acquisition daughter board). An analogue low-pass reconstruction filter (Mini circuits BLP 90+ with 3dB cut off frequency 90MHz) was connected at this point to provide attenuation of any high frequency components present in the DAC output signal. The signal was amplified by a high-frequency amplifier (Mini-circuits ZFL-1000VH2) to boost the drive voltage of the electro optic modulator to achieve greater modulation depth.

To test the accuracy of both techniques, the pathlength calculation was applied to a range of known single pass distances, as illustrated in Figure 6.8. The distances were measured using an engineering ruler with a measurement uncertainty of ±1mm.

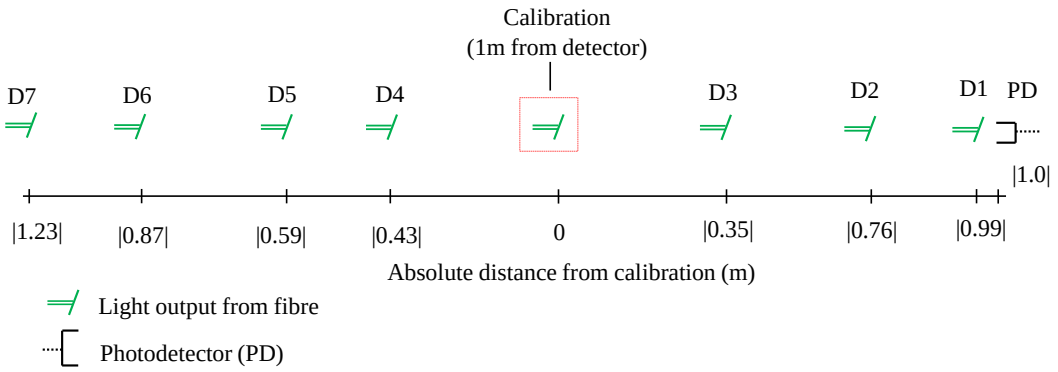

Figure 6.8: Single pass setup to test accuracy of signal processing; the light output is placed at various known distances (±1mm) from the calibration point using the setup as in Figure 6.1 with an open path in place of the integrating sphere.

The pathlengths of two different spheres were measured, one with a diameter of 5.04cm (termed the 5cm sphere), made with Zenith^{TM} (Thorlabs IS-400) and the other with a diameter of 13.46cm (termed the 13cm sphere) and made with Spectralon^{TM} (Labsphere 3P-GPS-053-SL). To ensure that specular reflections from the first strike spot did not influence the measurement signal, the photodetector was placed orthogonal to the input port. It was found that the measured output power from the laser was reduced by 95%, i.e. from approximately 20mW to 1mW after passage through the EOM, due to, it is thought, the wavelength being out-with the bandwidth range of the EOM resulting in reduced visibility. This greatly reduced the incoming power into the sphere and resulted in a noisy output signal at the detector i.e. output on the order of a few µW.

After detection (Thorlabs PDA10CF fixed gain, 10kV/A, 150MHz BW, 0.2mm^2 active area), to prevent aliasing, the signal was filtered with a low pass analogue filter (Mini-Circuits BLP-50+ with 3dB cut off frequency 50MHz) digitized at sample frequency, f_s = 150MHz by the ADC (Altera data acquisition daughter board), then transmitted to the same FPGA. The signals were processed as described in Section 6.1, i.e. the phase shift of a known distance was compared with the "unknown" distances i.e. D1-D7 to calculate the expected pathlength, according to the equation in Figure 6.6. For each frequency selection, the measurements were averaged over ten seconds to improve the

signal to noise ratio. The chosen frequencies of detection were integer multiples of the base frequency, which in this implementation corresponded to 1.172MHz i.e. 150MHz/128samples. The measurable frequencies were limited by the analogue filter at the acquisition stage, which has a 3dB cut off of 50MHz, and so integer multiples greater than that were not considered.

6.2.2 Experimental results

Pathlengths were calculated for each measurement; the results for distances D3. D4 and D6 are plotted below in Figure 6.9.

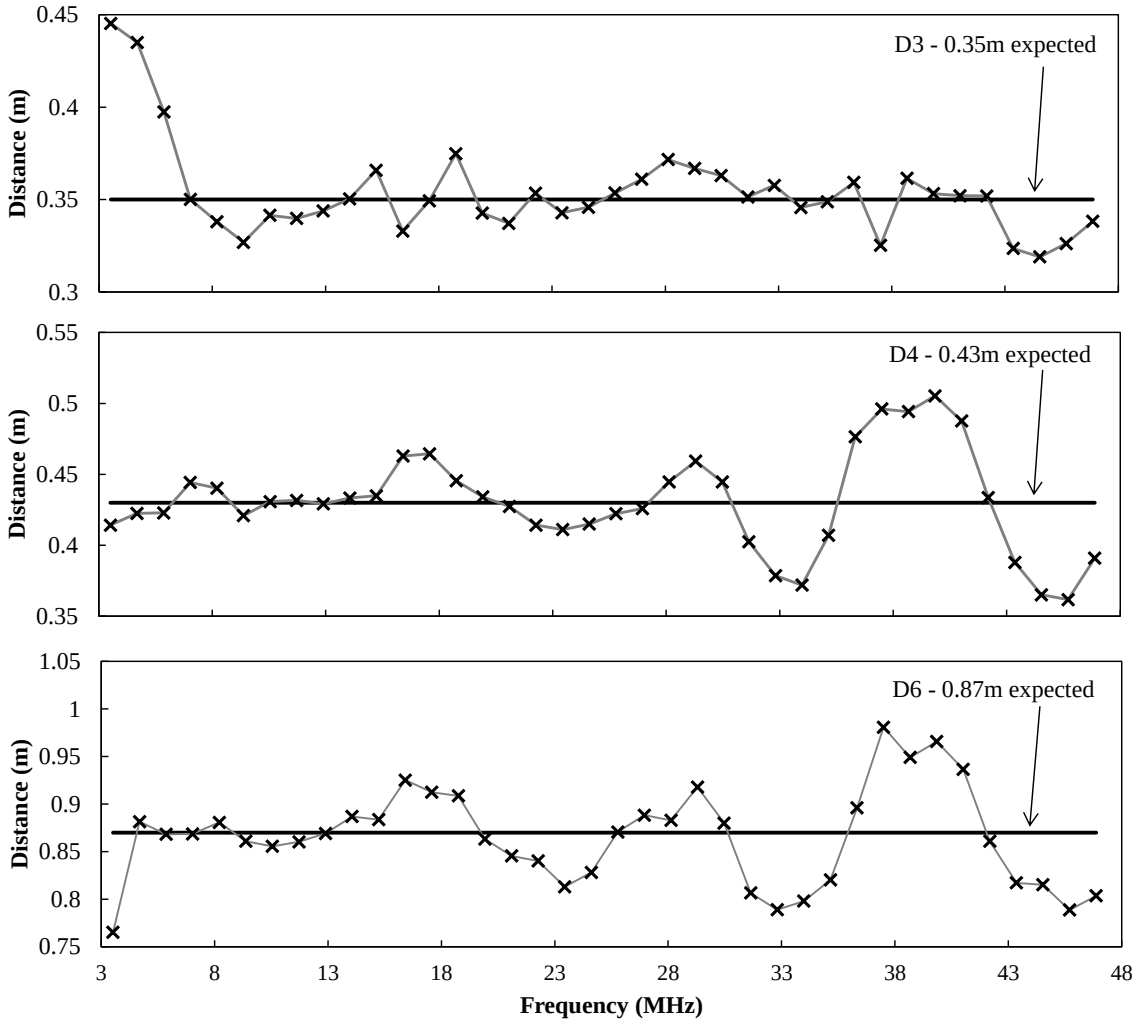

Figure 6.9: Single pass setup, showing variation in pathlength measurements over a range of frequencies using the sinusoidal modulation technique

Taking the average and standard deviation of the measurements over all frequencies for each distance, as in Table 6.1, gave distance measurements that corresponded to their expected distances respectively.

Table 6.1: Average and standard deviation of distance measurements made for three lengths over the frequency range 3-48MHz.

	Measured distances	
Expected (±0.001m)	Average (m)	Stdev. (m)
0.35m (D3)	0.35±0.005	0.03
0.43m (D4)	0.43±0.005	0.03
0.87m (D6)	0.87±0.008	0.05

A standard deviation of up to 5cm occurs because of, it is thought, the additional structure as a result of a lack of polarisation control at the source fibre, which is single mode. This contributed to the systematic semi-periodic nature of the deviation from the true value, as seen in Figure 6.9. Additional investigation, which is discussed in section 6.3.4, found that the source of this interference could be attributed to polarisation effects in the fibre lead connecting the laser (the fibre pigtailed to the laser was found to be single mode fibre) and the EOM. Due to time constraints it was not possible to repeat experiments using the sinusoidal modulation to confirm this but measurements shown in section 6.3.4 confirmed that the interference was reduced by use of a laser pigtailed with polarisation maintaining fibre.

Following this, it was decided to test the technique using both the 5cm and 13cm diameter spheres. In the case of the 13cm sphere, with 1cm thick port adaptors, the detector was recessed by over 1cm and so the throughput was below the baseline detector noise. As a result one of the ports had to be replaced with a shallow port so that the detector was less recessed. This resulted in an area of $5cm^2$ where the surface was less than 3mm thick and thus the reflectivity at this point would not correspond to the manufacturer quoted 0.987. It would be expected that as a result the resultant pathlength would be reduced. Nevertheless, as a comparison, an effective pathlength was calculated for both spheres based on the analytical model as detailed in Section 6.1.2. The sphere wall reflectivity was chosen based on the best fit with the experimentally

determined data and a port fraction was calculated from measurement of the port areas. The results for the 5cm and 13cm sphere are plotted in Figure 6.10.

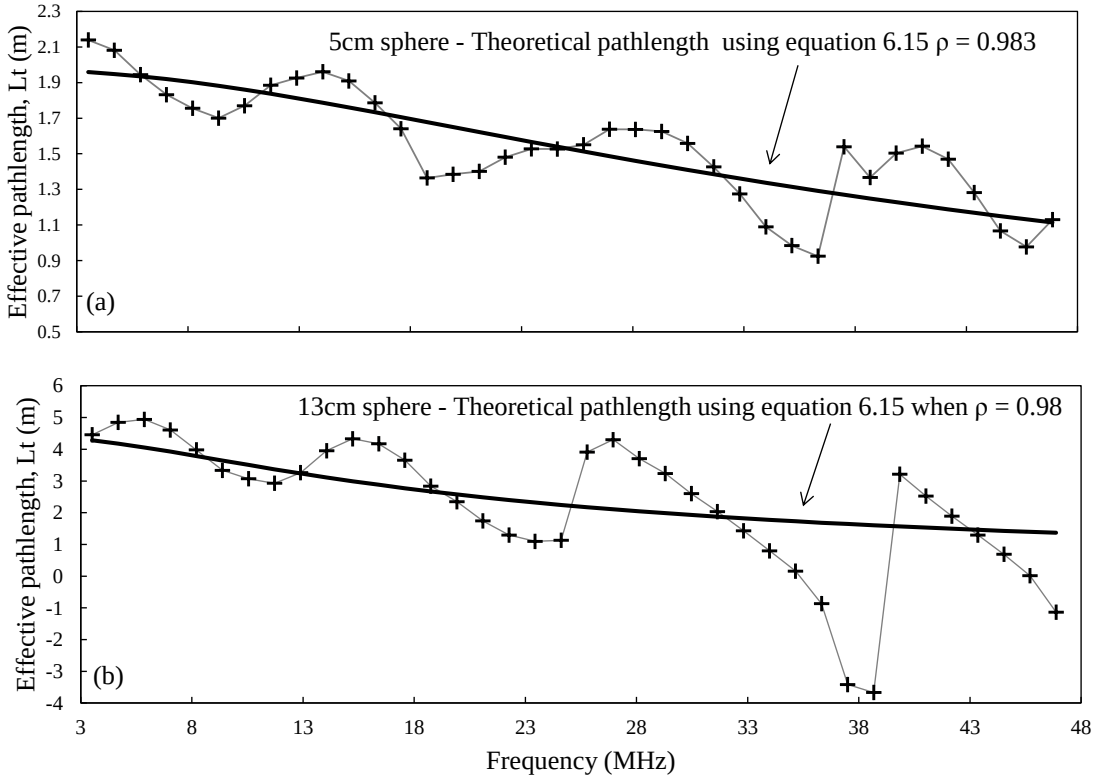

Figure 6.10: (a) Measured effective pathlength for (a) 5cm sphere and (b) 13cm sphere over frequency range 3-48MHz.

Due to the nature of how the light is diffused, i.e. a larger proportion of the light penetrates the wall up to 1cm, the sphere output signals are two orders of magnitude weaker than the input signal, unlike for a single pass. As a result the relative magnitude of the artefacts from the polarisation mismatch effects is considerable, especially for the 13cm sphere. However it can be seen that the measured pathlength trends with the theoretical derived pathlength, i.e. the phase shift due to the light distribution within the sphere varies as an arctangent function with frequency. An average of the theoretically calculated pathlengths over all frequencies is compared with an average of the measured pathlengths in Table 6.2.

Table 6.2: Average and summed standard deviation of pathlength measurements made for the 5cm and 13cm spheres over all frequencies

	Measured distances	
Derived average (m) (Eq. 6.15)	Average (m)	Stdev. (m)
1.54 (5cm sphere)	1.54±0.02	0.13
2.45 (13cm sphere)	2.23±0.02	0.12

As seen in Table 6.2, the average measured pathlength closely matches the theoretically derived pathlength for the 5cm integrating sphere. The pathlength for the 13cm deviates considerably, the reason for which is possibly due to low signal to noise ratio or more appreciable polarisation related artefacts obscuring the desired signal. Additionally the actual sphere wall reflectivity for both spheres is not known, e.g. a shallow port was used in the 13cm sphere and so the estimated theoretical value may be inaccurate.

The setup was then tested in the presence of both an absorbing gas and sphere wall contamination. It was expected that the presence of sphere wall contamination would have a much greater effect on the effective pathlength due to the heavy dependence of the achievable pathlength on sphere wall reflectivity. In terms of the absorbing gas, it was expected that the effective pathlength reduction would vary proportionally with gas concentration, e.g. the largest concentration would give the greatest effective pathlength reduction. The pathlength measurement was repeated with different concentrations of methane, both with and without contamination. Contamination was induced as in Chapter 5, by placing a fouling tab of low reflectivity insulating tape into the sphere. Only one level of contamination was tested, using one tab of size 12x5.3mm approx., corresponding to 0.81% coverage of the sphere wall for the 5cm sphere and 0.11% for the 13cm sphere. The emitted wavelength was monitored using the optical spectrum analyser (OSA) to ensure that the laser remained at the gas absorption peak line centre. Different methane gas concentrations, namely 493ppm, 1235ppm and 2475ppm, were achieved by controlled downstream mixing of air and methane using a bank of mass flow controllers. For practical application of this technique, the intended conditions for initial pathlength calculation, i.e. the calibrated setup, would be the sphere without any

contamination or absorbing sample so that the pathlength is derived from the sphere parameters only, i.e. sphere wall reflectivity, port fraction and sphere dimensions. For these experiments, the measured changes in effective pathlength due to sphere wall contamination and/or presence of an absorbing gas were expressed in terms of their percentage difference from the empty uncontaminated sphere at each frequency. The results for the 5cm sphere are plotted below in Figure 6.11.

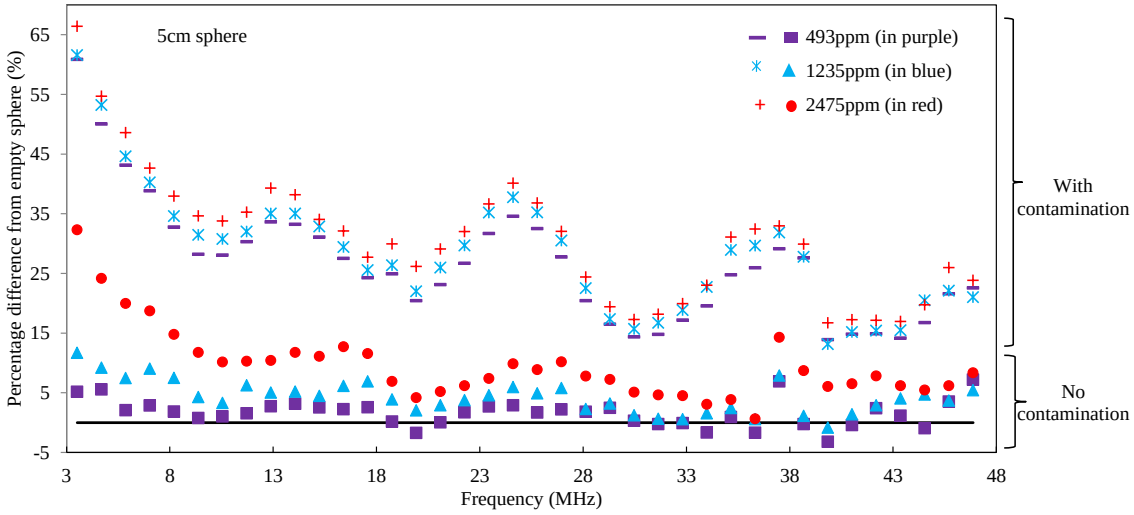

Figure 6.11: The percentage change in effective pathlength due to sphere wall contamination (using a fouling tab of ≈12x5.3mm) and/or varying gas concentrations for the 5cm sphere

As seen in Figure 6.11, contamination of the sphere wall has the largest effect on the effective pathlength as expected, differing by an average of 50% at lower frequencies. The presence of an absorbing gas as expected caused an effective pathlength reduction, with the percentage difference increasing for higher concentration. Using experimentally determined data from Chapter 5, i.e. measured absorbance when in the presence of known levels of contamination, an extrapolation could be used to make an estimate as to what the expected % difference in pathlength due to contamination would be in this case. For contamination covering 0.81% of the sphere wall surface, and neglecting the additional effect of the presence of gas, it is expected that the percentage difference in pathlength would be approximately 30%.

In terms of each set of measurements, i.e. the frequency range for each induced change, the percentage difference decreases with increasing frequency of detection. It is

supposed that this comes about due to a reduction in sensitivity caused by a reducing overall phase shift at higher frequency.

With the 13cm sphere, as the throughput was so low already, the additional loss of throughput caused by the contamination reduced the signal to below the baseline noise and so it was not possible to observe a trend, as shown in Figure 6.12. In terms of the gas input, concentrations of 475ppm and 2475ppm were used. Though there did appear to be some pathlength changes due to gas absorption, the measurements were obscured by the polarisation related artefacts.

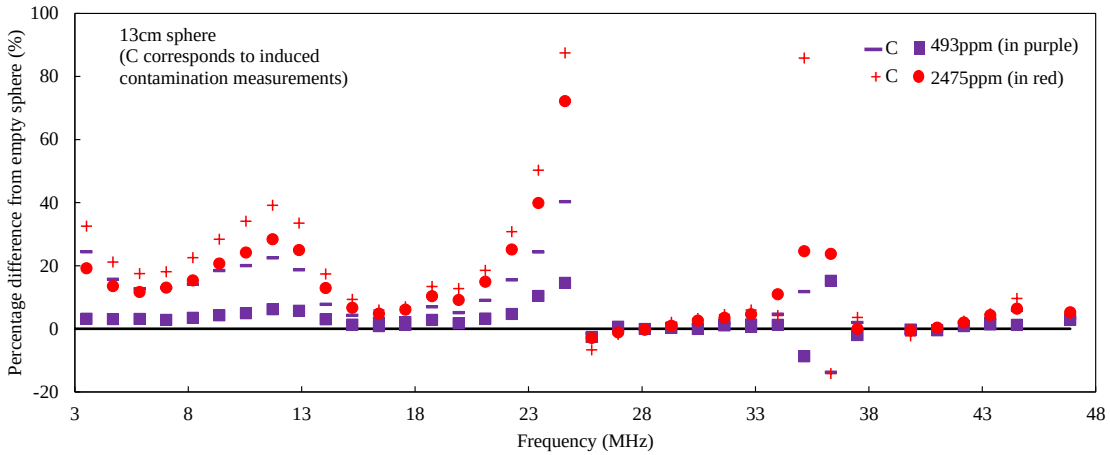

Figure 6.12: The percentage change in pathlength due to sphere wall contamination (using a fouling tab of ≈12x5.3mm) and/or varying gas concentrations for the 13cm sphere

It was not possible to draw any strong conclusions from the measurements with the 13cm sphere, as seen in Figure 6.12, however it is expected that with increased light throughput the output values will be above the detector baseline noise and the results will trend in the same way as the 5cm sphere. Furthermore the removal of the additional artefacts will provide a more accurate measurement. One strategy to achieve a greater signal to noise ratio is to directly modulate the laser thus removing the effect of the electro-optic modulator. This and other conclusions are discussed further in the final section of this Chapter.

6.3 Pulsed modulation

As mentioned in Section 4.4, Cone *et. al.*[70] introduced a cavity ring down based approach using an integrating cavity, termed integrating cavity ringdown spectroscopy

(ICRDS). Here a longer pathlength or "rate of decay" was quoted, as a result of using a material that exhibits higher reflectivity (0.99919 at 532nm) than the commercial spectralon material. This body of research aimed to showcase a coating that would allow for a more sensitive ringdown system in a sphere setup. My own research differs in that the aim was to create a more effective ringdown system technique using a type of signal processing which aims to improves the signal to noise ratio, rather than enhancing the performance of the cell itself. The improvement is achieved by employing a pulse repetition approach through use of a digital code called a maximum length sequence, MLS.

6.3.1 Maximum length sequence (MLS) theory

A narrow pulse with a delta function, i.e. an impulse signal, is an attractive measurement stimulus for a number of reasons. It contains a wide frequency spectrum, where the phase and magnitude is flat across all frequencies, as illustrated in Figure 6.13.

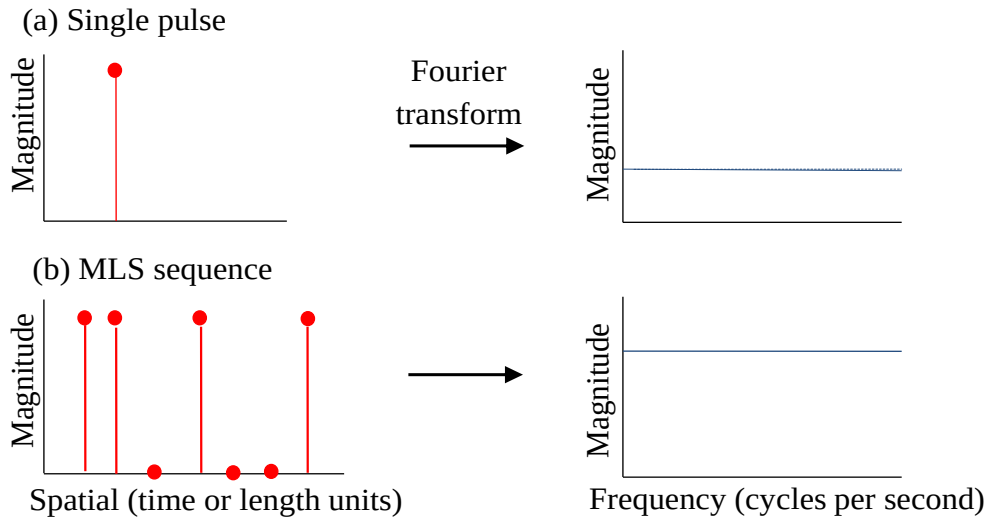

Figure 6.13: (a) Single pulse vs (b) Maximum length sequence (MLS): The phase and magnitude are flat over all frequencies for both, but the MLS, due to interrogating the system with a series of pulses, gives a greater signal to noise ratio.

Applying an impulse to a system and measuring the impulse response provides simultaneous measurement of the characteristics of the system over the whole range. This information can be Fourier transformed into the frequency domain thus allowing phase and magnitude information to be extracted both for the input signal and the time

delayed output signal. However a big disadvantage of using the narrow pulse is the signal to noise ratio, SNR. The signal duration is very short, while the data response time must be long so that all frequency components down to the low frequencies are captured. Averaging over a number of impulse responses can reduce the effect of background noise however this can slow down the overall data acquisition time as each pulse has to decay completely before the next measurement can be made.

Application of a maximum length sequence, MLS[180], [181], can alleviate some of these disadvantages. An MLS is a pseudo-random sequence, in which, like a single pulse, the magnitude is flat but unlike single pulses, the phases are coded. Though seemingly random, the phases of the spectral component are in fact deterministic and repeatable and so an MLS can be used in the same way as a single pulse. Because the signal is repeatable, measurements can be made without the need for a second reference channel, which would be the case if the sequence was truly random.

The excitation signal for an MLS is a series of pulses that repeats itself, thus producing a higher average signal level as well as a greater signal to noise ratio. One of the properties of an MLS is that, when the binary sequence is generated, there is an almost equal number of 1s and 0s which gives a duty cycle of 50%. The length of the sequence has a periodicity, P, of the form.

$$P = 2^N - 1 \qquad 6.16$$

Where the N is an integer and corresponds to the number of simple logic circuits, known as shift registers, used. So for example a sequence generated using a shift register of length 7 would be 2^7-1 samples long i.e. the sequence will repeat every 127 clock cycles. The use of shift registers ensures that the MLS can be generated rapidly, without additional computing time on each clock cycle.

In practical application, the FPGA produces a series of pulses by varying the signal voltage based on the binary sequence that has been input. The use of a series of pulses improves the signal to noise ratio without sacrificing acquisition time as, due to the deterministic nature of the sequence, a pulse does not have to fully decay before the next pulse can be introduced. For accuracy, it is important that the entire sequence

length is longer than the impulse response of the system or else the impulse responses will overlap (leading to time aliasing).

6.3.2 Implementation

For this particular implementation, as the FPGA had been previously configured thus, a sequence length of 127 was used, which gives a sequence length in time of 0.85μs (1/Base frequency). Despite averaging over 10 seconds, the low throughput of the sphere still proved challenging and it was found that the signal was somewhat obscured by electronic noise, created due to the "start-up" effects when generating the pulse. The electronic noise decayed rapidly with time and so a reel of single mode fibre could be inset into the measurement arm as seen in Figure 6.15, which introduced a physical delay and thus moved the measured signal to a region where this electronic noise would be considerably less. The measured impulse response could then be cut off before the main rise period of the impulse response of interest. A typical signal is illustrated in Figure 6.14.

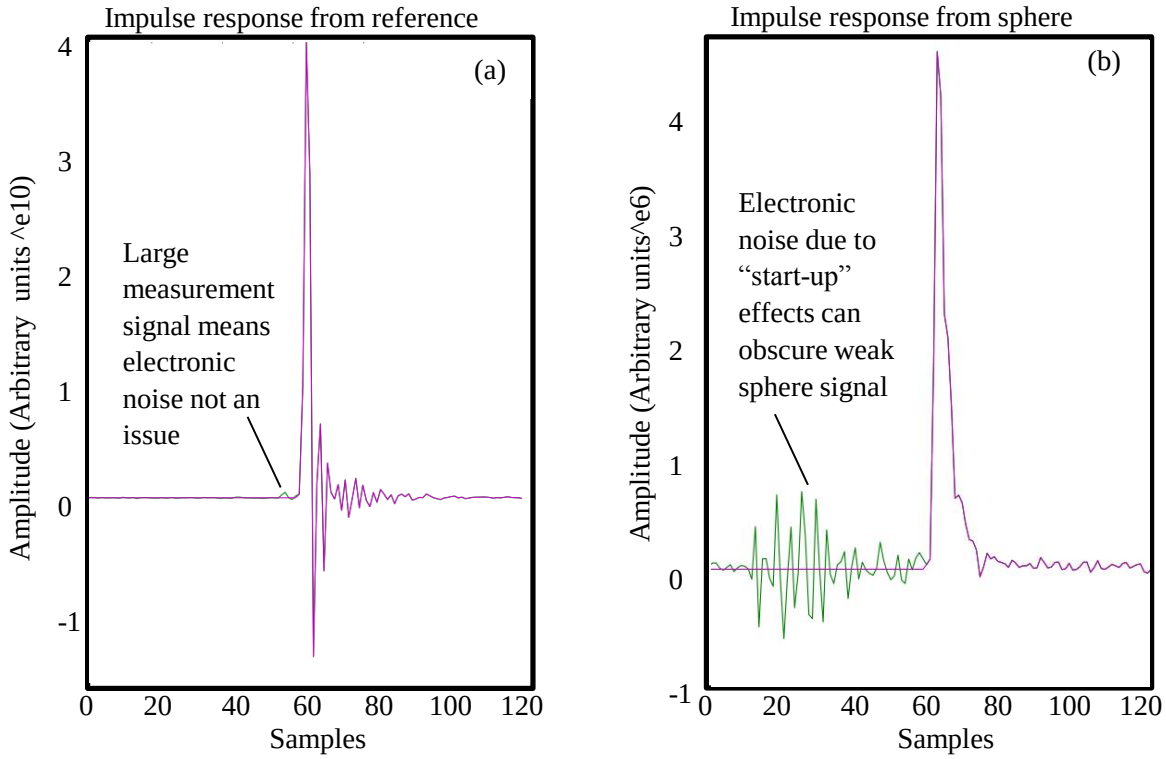

Figure 6.14: A typical impulse response for (a) a strong reference signal and (b) a weaker sphere signal, where the electronic noise due to "start-up" effects can obscure the signal if not removed. Note: different scales on y-axis.

For a strong signal the electronic noise is not an issue as seen in Figure 6.14(a) for the reference signal, or a single pass setup. In the case of the integrating sphere, the signal is so weak that it can become obscured by the electronic noise if not removed, as seen in Figure 6.14(b), the impulse response for a 5cm integrating sphere. The magnitude of electronic noise (in green) as a result of the initial pulse generation is reduced by taking a baseline average of the samples before the noise, e.g. from 0-15 then substituting this baseline average value for the region where the electronic noise is largest. Once the signal has been recorded, the amplitude and phase information can then be obtained and the pathlength calculated as described in Section 6.1.2.

In the case of the pulsed technique, the pulsed modulation is achieved by directly outputting a digital code from the FPGA. An amplifier was not required for the pulsed modulating signal.

A schematic of the experimental setup is shown below in Figure 6.15. It can be seen that the setup is almost identical as for the modulation technique described in section 6.2.1, with the exception of addition of a reel of single mode fibre of length 43m, and direct output from the FPGA to the EOM. The same components as listed in Section 6.2.1 were used.

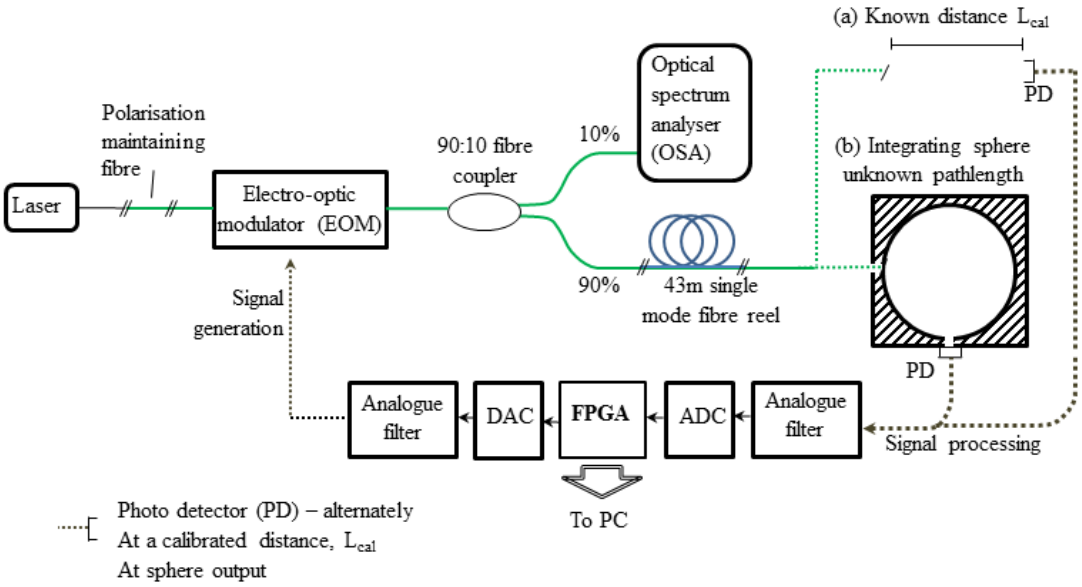

Figure 6.15: Setup for pulsed modulation; Signal processing as described earlier, wavelength monitoring with optical spectrum analyser (OSA). A physical delay was added using a reel of single mode fibre (SMF) to move the desired impulse response signal away from the electronic noise created during laser pulse "build-up".

6.3.3 Experimental results

As before the scheme was tested using the linear setup as described in Figure 6.8. Phase shift measurements were made three times at each distance to check the repeatability. These single pass measurements would not be subject to the same throughput penalty as that of the multiple pass effective pathlength of the integrating sphere. And so to simulate a weaker signal, imitative of that in an integrating sphere, all measurements were repeated with a number of bends introduced into the fibre measurement arm to attenuate the light by approximately 75%. This, as for the modulation technique described previously, was repeated for a number of harmonic frequencies. Results for seven measured distances vs. expected distances are plotted below in Figure 6.16, showing the effect of a weakened signal on the pathlength measurement.

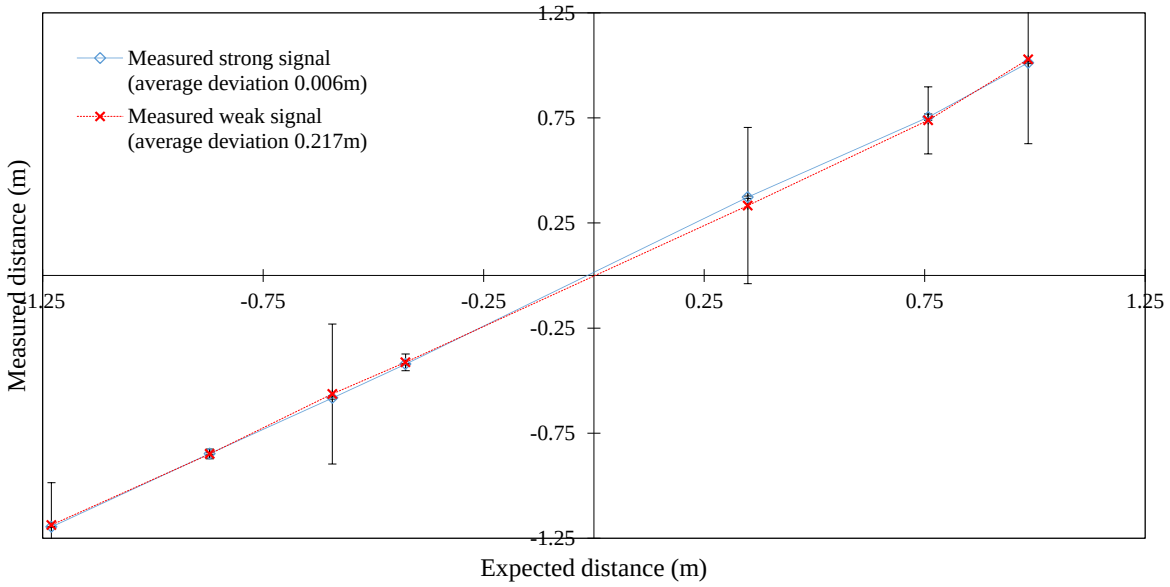

Figure 6.16: Linear setup; measurement at seven distances, both with a strong and weak signal. The error bars correspond to the maximum deviation that was measured at a given frequency and was found to be greater for the weaker signals. The error bars for the strong signal are not visible.

As seen in Figure 6.16, with a weakened signal, the distance values deviate from the true values by more than those for the stronger signal in terms of repeatability of the same measurement, i.e. the standard deviations. The standard deviations do not fully account for divergences from accuracy as there may be some systematic error from the electronics that has not been thoroughly investigated. The magnitude of the weakened signal is similar in strength to that after passing through the integrating sphere i.e. on the

order of a few µW, which could suggest that the low flux throughput experienced in integrating spheres setup may also reduce the repeatability of the measurement even if the signal is above the baseline noise. It is possible to observe the same artefacts here as when using the sinusoidal modulation technique however it is unknown what contribution this additional structure made to the measurement variation in the weaker signals. The experiment was repeated with the 5cm sphere, as seen in Figure 6.17.

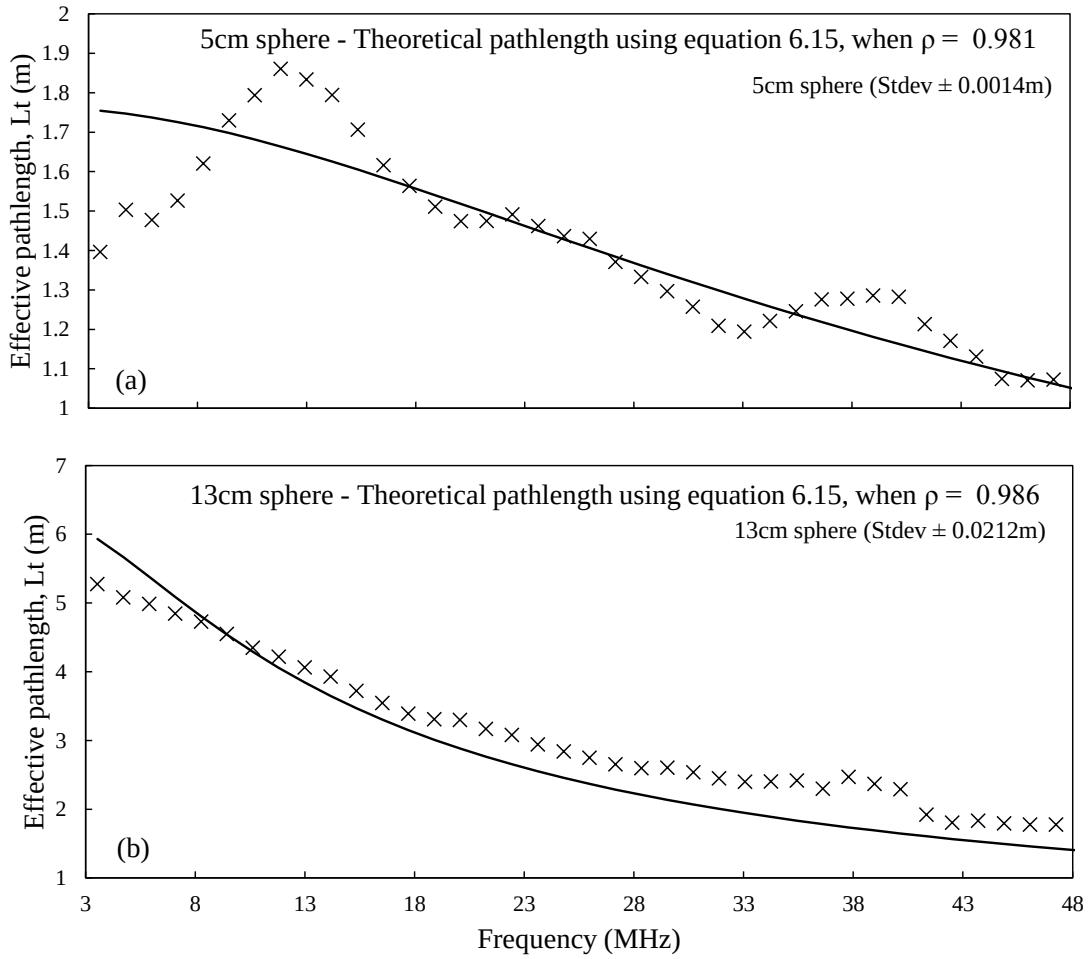

Figure 6.17: Sphere setup: Measured effective pathlengths for (a)5cm sphere and (b) 13cm sphere when MLS code is implemented. The standard deviation for each comes from the variation between three repeat measurements.

As with the sinusoidal modulation technique, the phase shift varied as an arctangent function with increasing frequency for this technique. Though still subjected to some interference, the MLS technique appears to preferentially enhance the signal of interest over background or transient noise. The reason for this is not fully understood though

may be due to the nature of how the MLS output signal is correlated with the input signal.

The system was then tested using the same gas concentrations and fouling tab as described in Section 6.2.2. The results using this technique are plotted, as for the sinusoidal modulation, in terms of the percentage difference from the empty, uncontaminated sphere, as seen in Figure 6.18.

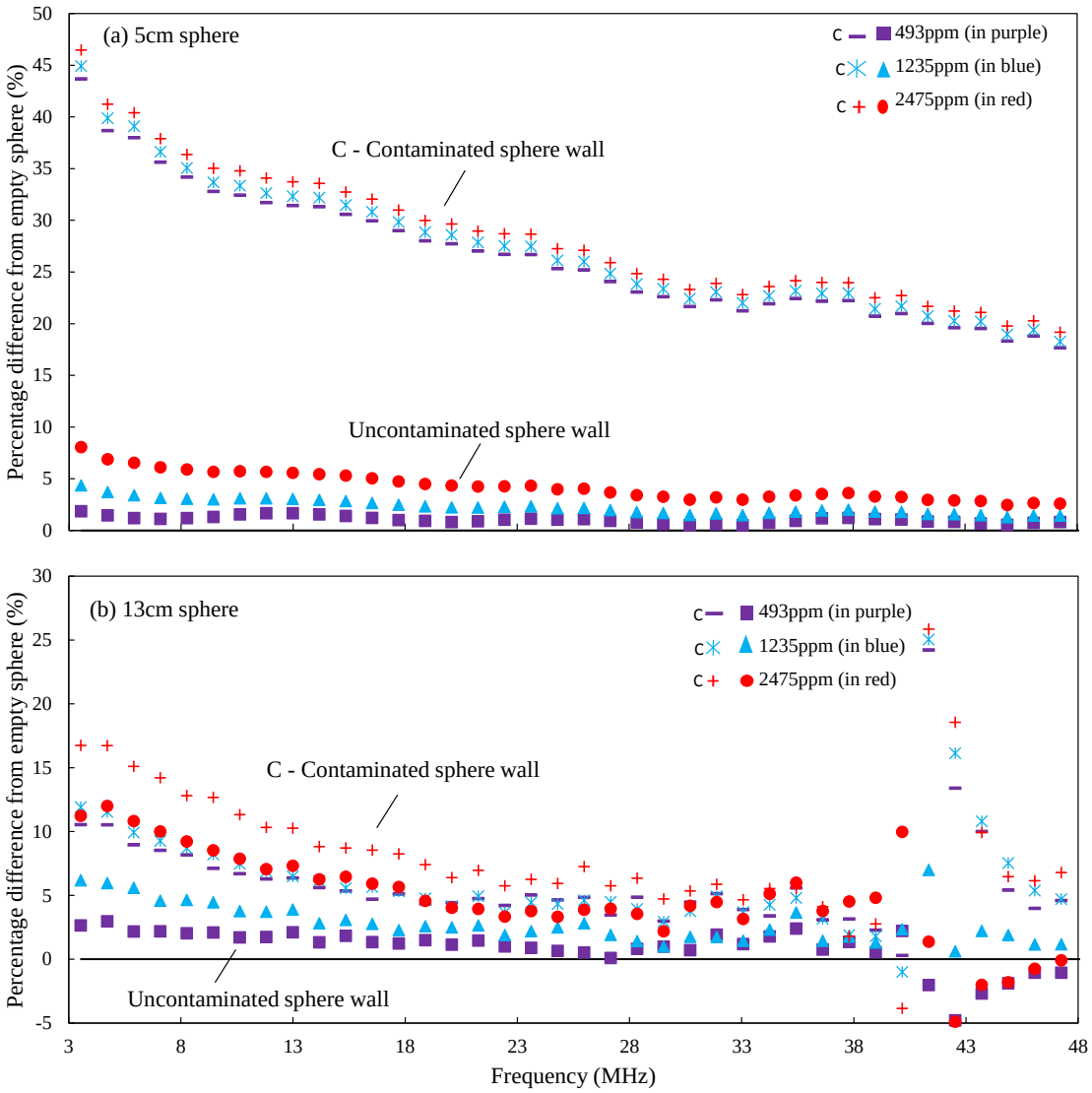

Figure 6.18: The percentage change in pathlength due to sphere wall contamination (using a fouling tab of ≈12x5.3mm) and/or varying gas concentrations for (a) 5cm and (b) 13cm sphere.

As with the sinusoidal modulation technique the resultant pathlength percentage difference decreases due to the arctangent phase relationship to frequency.

6.3.4 Interference fringing investigation

It can be seen that in both techniques, structural artefacts persist throughout all measurements, which can be observed as an approximately periodic variation on the signal magnitude as a function of frequency. After various potential electrical sources of interference were ruled out it was concluded that the effect was optical. By measuring the output at each optical component, e.g. coupler output, fibre connection points etc., the source of the interference was narrowed to the fibre coupled to the DFB laser. It is proposed that as the fibre coupled to the laser is standard single mode fibre rather than polarisation maintaining, an undefined polarisation state is input to the intensity modulator. The lithium niobate modulator has an inherent polarisation sensitivity, leading to different modulation depths for the different principal polarisation axes. The intensity modulator has an inbuilt polariser to force the use of one axis, however, this only offers an isolation level of 19 dB (see appendix B). The presence of the light from these different modulation depths states could lead to unforeseen effects in the measurements. As a result polarisation control is required to stabilise the intensity modulator output, which was seen to fluctuate with movement of the non-polarisation maintaining fibre. To further confirm if indeed the fringing came from the fibre coupled laser, the setup was tested with a similar butterfly packaged DFB laser fibre coupled with polarisation maintaining fibre (Agere M-D2547 PG54). Unfortunately this laser is tuned to 1540nm and so could not be used for methane detection.

The pathlength measurement was tested first with a single pass at a distance of 0.44m as seen in Figure 6.19(a). The average distance measured using the polarisation maintaining (PM) fibre coupled laser was 0.442±0.003m. As seen in Figure 6.19(a), there is no obvious structure throughout the measurements and as a result the standard deviation over all frequencies is much smaller than if PM fibre is not used.

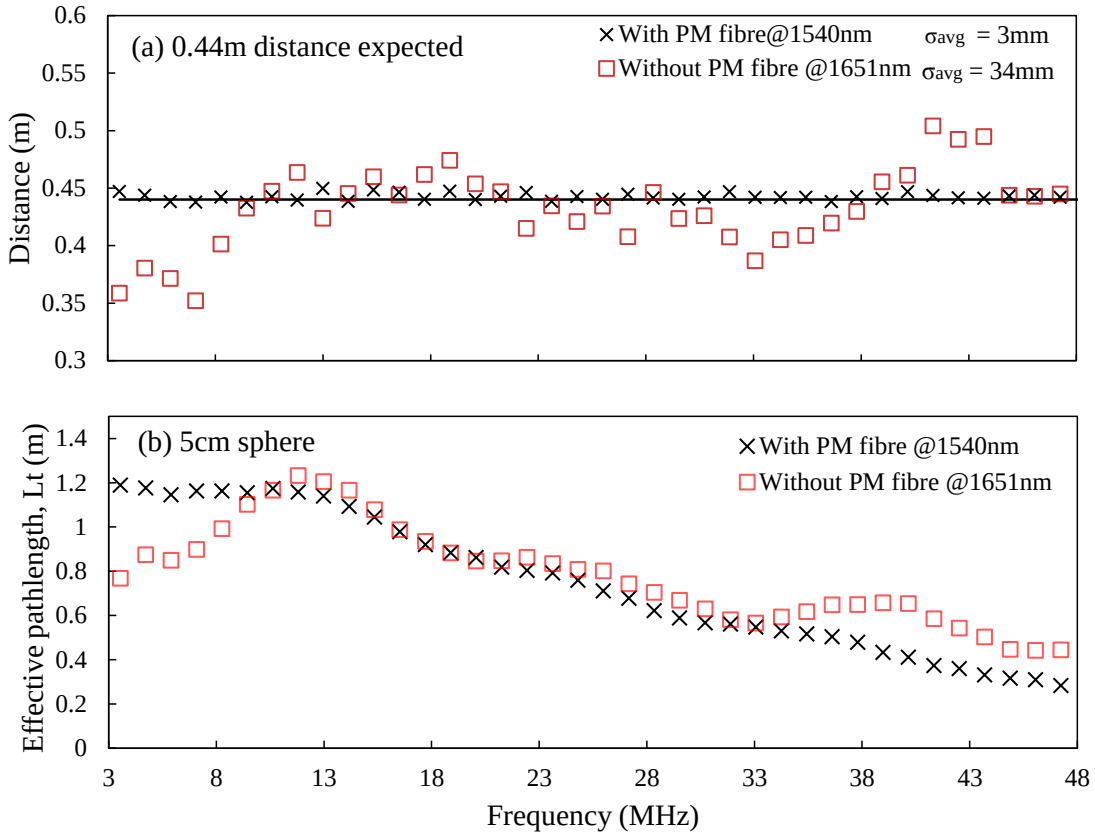

Figure 6.19: Distance and pathlength measurement for single pass and 5cm sphere when 1540nm polarisation maintaining (PM) fibre coupled DFB laser is used (black crosses) and when 1651nm single mode fibre coupled DFB laser is used (red squares).The extent of the artefact type structure is greatly reduced when PM fibre is used.

In the case of the 5cm integrating sphere, as seen in Figure 6.19(b), there did appear to be some additional structure persisting, however to a much lesser extent than the previous measurement for the 5cm sphere, i.e. Figure 6.17(a). Ultimately though the aim is to return to using the 1650nm DFB laser and so the setup would be optimised for this, as discussed in the next section. Overall this supports the hypothesis that the source of the periodic variation in the original results was the use of non-polarisation maintaining fibre for the laser pigtail.

6.4 Discussion and future work

As stated in the introduction the motivation for pursuing this technique was to be able to measure the pathlength of an integrating sphere without the requirement for a reference gas cell at the calibration stage.

In fact, using this type of processing has a number of advantages, including improved signal to noise ratio, ease of use, compactness and of course cost-effectiveness. The major challenges encountered when implementing this processing scheme were low sphere throughput and polarisation related interference fringes. These advantages and challenges are discussed in the following section in terms of what has been achieved so far and aims for improvement in the future.

6.4.1 Benefits of and improvements to work to date

Improved signal to noise ratio: With the FPGA based signal generation it is possible to employ high modulation frequencies which, with less background noise to contend with, allows for improved signal to noise ratio than if a lower frequency range was used. This is particularly useful for an integrating sphere setup where the throughput is reduced (e.g. considering the power output for one source in the four beam setup, where approximately 0.7mW input flux encountered the sphere walls to form the diffuse long path; the measured output flux for this path was approximately 1.3μW) and the sphere wall reflectivity is low relative to other techniques that measure rate of decay, such as cavity ring down.

In this body of research, due to the availability of analogue filters, measurements were limited to frequencies below 50MHz; and so if higher bandwidth filters were obtained there may be potential for detection of higher frequency harmonics. A major cause of low power output, as mentioned in section 6.2.1, was through use of the electro-optic modulator (EOM) which reduced the output power from the laser by nearly 95%, from 20mW to just over 1mW. Furthermore the EOM imposed a polarisation state dependence which resulted in the polarisation related artefacts that have persisted through the experiments. Despite this the EOM was used because the electronic configuration of the laser meant that it was unsuitable for direct modulation with the bias-T adaptors that were available for the butterfly package mounts used. It is intended in the future to custom build an adaptor to allow for direct modulation thus avoiding the use of an EOM. Furthermore the generated signal will not be limited to a specific operating wavelength range as with the EOM (see Appendix B for datasheet) which could cause the non-linear phase modulation effects that were discussed in Chapter 3.2.4 if operating outside the correct range. To facilitate easier detection it is also

intended to use surface mount detectors so that the detector is not as far recessed as it was, particularly in the case of the 13cm sphere where the port adaptors were over a centimetre thick. This would both improve the detector's numerical aperture and reduce the port fraction.

In the case of the pulsed modulation, the use of the maximum length sequence, as seen in Section 6.3.1, should provide an improved signal to noise ratio due to the increased amplitude provided by the series of pulses as opposed to a single pulse. A sequence length of 127 was used as dictated by the sample window of the FPGA configuration. An even longer sequence could be implemented easily enough by reconfiguring the FPGA. This would allow for use of a longer reel of fibre, which would result in the impulse response coming at a later sampling time, and thus further from the noise effects that occur at the pulse initiation stage.

As stated in Section 6.3.4, it was found that the polarisation related structure observed on the experimental results originated from the fibre coupled to the laser source. It is intended to use polarisation controllers so that the light can be aligned to a preferential polarisation axis to ensure maximum and more stable power output.

Ease of use: Because both techniques employ a time based approach, fluctuations in output flux from the laser are not an issue as they would have been with the four beam technique described in Chapter 5. There is no specific optical alignment requirement, only that, as recommended in all sphere based literature, there is not a direct line of sight between the laser source, first strike spot, and the detector. We would expect the system to work well in the event of window (Section 5.4.3) or first strike spot (Section 5.4.4) contamination. In terms of the electronics, once the FPGA has been configured, the required functions, i.e. signal generation and processing, can run concurrently and as a result without loss of processing efficiency. The combined use of FPGA and PC processing allows considerable flexibility in selecting measurement parameters required, i.e. frequency of detection, sampling time etc. However one consideration that has not yet been investigated is the system's long term performance, whether the system drifts in terms of amplitude and phase measurements relative to the calibration. It was also found during initial implementation designs that the measurement could be subject to crosstalk if another channel on the FPGA was being used simultaneously, and the

magnitude of this crosstalk was proportional to the magnitude of the signal causing it. So for example, one idea of using a second channel on the FPGA for a simultaneous reference phase measurement may itself introduce an error that becomes appreciable when the magnitude of the desired signal is low due to the crosstalk caused by the reference channel.

Compactness and cost efficiency: As seen in Figure 6.1, the setup does not have many components, with the laser and the integrating sphere accounting for the biggest components. Future implementations could include the direct modulation of the laser, thus removing the requirement for an EOM and potential undesirable effects that accompany it. The required waveforms can be generated by the electronics, the optical paths are in fibre and so can be coiled without any need for a particular configuration. The consequence of having no tight tolerances on alignment allows for a very compact setup that is easily transportable. The system can accommodate changes in alignment that might alter the pathlength, unlike the four beam setup. The system has minimal additional requirements over a standard TDLS system. In terms of cost, the optical and electronic components amount to less than £5000 in total and are commercially available, providing the potential for a cost effective gas detection system.

Future work: As well as implementing the systematic changes as discussed in the previous section, the next consideration for this technique is how to interpret and use the data. As seen in the experimental results in both Section 6.2.2 and 6.3.3, the measurements decreased over a range of frequencies with what was modelled as an arctangent function and were unique to each condition, i.e. contamination and/or vary gas concentrations. It is possible therefore that the gradient of this change with frequency could itself provide information concerning the pathlength and/or pathlength distribution.

Further investigation is needed to ascertain if/how these functions could be used to identify pathlength deviations due to contamination or presence of an absorbing gas. As mentioned in the introduction to this chapter, it was also envisaged that a lower frequency current ramp could be applied simultaneously so as to sweep the laser wavelength. This would allow an off and on gas line measurement to be made so that

phase shift due to contamination could be isolated from the phase shift due to absorbing gas.

As a complementary technique it would be useful to apply this pathlength measurement to the four beam technique as described in Chapter 5, where the calibration measurement could be made at the relevant short path, i.e. first strike spot position. This would allow for the light pathlength, i.e. including the multiple reflections in the wall material, and the gas pathlength to be measured, something that hasn't been calculated at this time. It is important to measure this as it would ascertain whether the gas pathlength varies proportionally with the light pathlength. The implication if this is the case is that the light pathlength can be used as a means of pathlength calibration for the gas pathlength.

6.4.2 Summary

In this chapter, two intensity modulation techniques have been implemented for pathlength calibration of an integrating sphere. The first technique used a high frequency sinusoidal modulation, while the second employed a pulsed modulation, created by superimposition of a digital code sequence. A field programmable gate array (FPGA) processor was used in both techniques to simultaneously generate the modulation signal and process the resultant measurement.

The theory of operation was described for both techniques, with particular emphasis on the strategies employed to improve the signal to noise ratio. Experimental pathlength measurements have been shown for a linear single pass configuration and two integrating sphere multiple pass configurations. The single pass results showed that the pathlength could be determined to, at worst, an accuracy of ±9% for the sinusoidal modulation technique and ±11% for the pulsed modulation technique using this type of signal processing. It was shown through use of an alternative laser that these large deviations occurred because of polarisation related structural artefacts, attributed to an induced sensitivity to polarisation state by the EOM. In the case of the integrating sphere setups, introduction of one level of contamination both in the presence and absence of an absorbing gas measurement showed that the pathlength measurement changed as expected i.e. contamination caused the greatest reduction in pathlength and

the presence of an absorbing gas caused pathlength reductions relative to the concentration present.

It was affirmed that the structural artefacts represented a major limitation for accurate pathlength measurements (e.g. the 5cm sphere pathlength deviated from the expected by up to 20cm) and so future work would first seek to control the polarisation of the source at the input to the EOM or employ direct modulation. Future work has been proposed for system improvement, both in terms of the setup optimisation i.e. improving signal to noise ratio and throughput, and data processing i.e. measurements to discriminate between pathlength reduction due to gas absorption and/or sphere wall contamination. The benefits of the scheme have been summarised in terms of measurement and cost efficiency. To conclude, though at an initial stage, the use of an FPGA based signal processing scheme has the potential to provide in-situ pathlength calculation of an integrating sphere without the need for a reference cell.

7

Conclusions and outlook

7.1 Conclusions

During the course of this PhD project, two different approaches to pathlength calculation of an integrating sphere based multipass cell were proposed and experimentally tested. Integrating spheres differ from typical multipass cells in that the optically rough surface of the inner wall produces multiple diffuse reflections simultaneously rather than consecutive specular reflections. The effective pathlength is thus an integration of beam passes of differing lengths and phases. This eliminates the periodicity of beams, a common reason for formation of performance limiting optical interference fringes in typical multipass cells. Additionally the diffusive light distribution eases alignment tolerance and renders the effect of scattering samples negligible. However, as the effective pathlength is dependent on the sphere wall reflectivity, surface contamination can affect the calibration, leading to erroneous gas absorption measurements when in the field. The two techniques proposed in this thesis aimed to provide ongoing pathlength calibration even in the event of surface contamination. Both were tested using methane gas at various concentrations to demonstrate the efficacy of the integrating sphere as a multipass gas cell, as well as the whole setup as an optical gas sensor.

The first approach comprised a four beam setup where two sources and two detectors were positioned orthogonally to each other at sphere port openings and four independent flux measurements were made by alternately turning on the sources. Two of these flux measurements corresponded to direct single passes across the sphere whereas the other two measured the multiple diffusive passes, the effective pathlength as described in the previous paragraph. By using this configuration, it was possible to formulate a ratiometric algorithm of these four paths, which allowed for component

variation e.g. laser fluctuations, to be factored out. This was demonstrated by varying a source output power by 5% which resulted in an error of <1%. An achievement of this work was thought to be the creation of a mathematical derivation that accounted for certain levels of contamination on the inner cavity wall. In this way, if contamination on the wall caused a reduction in the overall pathlength, this effect could be corrected for, allowing gas measurements to continue to be made. A number of different locations, in the sphere i.e. the sphere wall and port windows, were deliberately contaminated and tested, and resultant absorption measurements were compared to results from an uncontaminated setup to ascertain the percentage error in the gas absorption measurement as a result of the contamination. It could be seen in section 5.4.2 that the mathematical correction greatly reduced errors due to sphere wall contamination e.g. at a gas concentration of 1500ppm, with no pathlength adjustment, contamination representing 1.2% sphere wall coverage gave a reduced absorption coefficient which had a percentage error of 41% compared with the calibrated value. With the ratiometric scheme, this error was reduced to 1%.

With increased sphere wall contamination e.g. >3% sphere wall coverage, it was suspected that the sphere property of uniform diffusion began to break down thus violating the assumption of pathlength symmetry when using the mathematical derivation. However even with this violation, a <10% error was achieved. Contamination at the other locations resulted in much more unpredictable and severe errors, in particular heterogeneous particulate contamination on the port windows. For this, it was found that the size of the particulate contamination dictated the extent of the error, with larger particulate sizes giving severe errors in measurement. It was not possible to correct for this using the mathematical derivation as the assumption that the direct, single pass would be unaffected by contamination was violated. It was thought however that by monitoring the flux of this beam pass, it could in itself serve as a warning that a window had been contaminated. As the alignment of the system is not complex it was thus felt that, in the event of this type of contamination, that the window could be removed, cleaned and replaced by the operator in situ without needing to be realigned at the laboratory.

An advantage of this type of setup is that it allows for a large dynamic measurement range as the direct single pass could be used in isolation for measuring high

concentrations of gas which ordinarily would saturate the diffusive long pathlength. In terms of system design, if component variation is not thought of as a major source of error, it is possible to remove one of the sources or detectors from the setup whilst still applying the mathematical derivation for pathlength correction. To conclude, as the overall reflectivity (and thus effective pathlength) of the sphere is heavily affected by contamination, being able to correct for this is a major advantage for realising an integrating sphere as a feasible option.

Changes to the optical pathlength of the instrument would affect both its calibration accuracy, as investigated here, and its sensitivity. We would expect that 50% reduction in instrument pathlength would result in a two-fold worsening of instrument sensitivity. Clearly, having a correction for pathlength changes provides information about both calibration accuracy and the instrument's limit of detection, and it is for instrument designers to decide how to use this information in different applications, which may impose different demands on these two aspects of instrument performance. The advantages and disadvantages of different aspects of this technique, as well as the experimental justification that motivated these comments are listed below in Table 7.1.

Table 7.1: Advantages and disadvantages of different aspects of the four beam technique, including experimental justification

Advantages (+) and disadvantages (-)	**Experimental justification**
Four beam configuration	
(+) Compensation for component variation, such as source fluctuation due to use of four beam passes	<1% error in absorption measurement at various gas concentrations when source output power was reduced by ≈5%
(-) Decreased sensitivity due to requirement for extra port openings	For a sphere diameter 5.08cm and reflectivity ≈ 0.975 the addition of two extra ports had the effect of reducing the pathlength by 12.4cm

Mathematical derivation	
(+) Ability to adjust pathlength in the event of sphere wall contamination, thus allowing for gas absorption measurements to continue to be made	At 1500ppm, and contamination of 1.2% sphere wall coverage Absorption error Uncompensated ≈41% Compensated ≈1%
(-) Introduced some alignment stringency in terms of beam divergence and position as pathlength adjustment relies on relating back to original calibration	30-40% of input beam directed into short path so long and short paths operated independently
Presence of a direct short path	
(+) Allows for high concentration measurements to be made without saturation of detector signal	
(-) High concentrations introduce proportional errors in pathlength correction	For contamination of 0.61% sphere wall coverage Compensated error 1500ppm ≈0.16% 3125ppm ≈ 2.63% 6250 ppm ≈ 3.09%

The second approach employed phase shift detection to calculate the pathlength of the integrating sphere. Two different experiments were investigated where two types of modulation were implemented, a high frequency sinusoidal modulation and a special digital code, an m-sequence, that resulted in pulsed modulation. A further innovation of these techniques was the use of an integrated circuit board, which allowed for generation of high modulation frequencies, as well as synchronised modulation and demodulation of the signals. The use of high modulation frequencies is desirable as it makes the system more sensitive to phases changes due to for example a reduction of pathlength caused by contamination or absorption by the sample. Interrogation using a pulsed modulation is similar to cavity ring-down techniques in that the phase shift being measured corresponds to a temporal decay. However unlike cavity ring-down, the

reflectivity of the sphere is lower e.g. 98.9% vs. 99.999%, and so the resultant "ring-down" is much shorter for an integrating sphere i.e. a few metres (on the nanosecond scale) as opposed to a few kms (on the micron scale). Thus having synchronised modulation and demodulation was invaluable to facilitate resolution of changes in phase and thus temporal response. The technique was applied to a single pass setup with known pathlength so that its accuracy could be tested.

A number of modulation frequencies were used to investigate how the sensitivity changed with modulation frequency. In this way it was discovered that the resultant measured phase shift for the integrating sphere had a non-linear dependency on the modulation frequency and in fact varied as an arctangent function. This function did continue to trend as would be expected with changing gas concentration and sphere wall contamination i.e. the pathlengths reduced with increasing gas concentration and/or sphere wall contamination. In a similar manner as the four beam technique the sphere wall contamination had a much greater effect on the resultant pathlength as opposed to the absorbing gas e.g. as seen in Figure 6.18, at approximately 8MHz and with a gas concentration of 1235ppm, sphere wall contamination and presence of absorbing gas gave a ≈35% deviation from the calibrated pathlength whereas with absorbing gas only the resultant deviation corresponded to ≈5%

Further investigation is required as the results from this body of research were somewhat limited by the components used. For example a major limiting factor was the creation of polarisation related structure due to the use of a laser diode pigtailed with single mode fibre. Polarisation states could not be maintained or aligned to the axes of the electro-optic modulator and so optical artefacts resulted that caused deviations in the measured pathlength. Furthermore the low power throughput meant that it was not possible to test the effect of contamination and gas absorption to the same extent as for the four beam approach. However, the results carried out so far have demonstrated a system that has real potential to offer a sensitive and easy to use technique for pathlength calibration. The advantages and disadvantages of different aspects of this technique, as well as the experimental justification that motivated these comments are listed below in Table 7.2.

Table 7.2: Advantages and disadvantages of different aspects of the phase detection technique, including experimental justification

Advantages (+) and disadvantages (-)	Experimental justification
High frequency modulation	
(+) Phase shift is larger at higher frequencies, thus giving greater sensitivity towards pathlength changes.	Even with weak output flux (Figure 6.9) it was possible to discern changes due to an absorbing gas or contamination.
(-) Requires high bandwidth detection components and filters for electronics.	There was less opportunity for amplification due to the requirement for high bandwidth. e.g. a fixed gain Thorlabs detector was used as it had 150MHz bandwidth. The frequencies of detection were limited by the availability (in the lab) of electronic filters which was 50MHz.
(+) Easy alignment through use of optical fibre components such as couplers and electro optic modulator (EOM).	Configurations were easily interchanged.
(-) EOM greatly reduced output power and use of fibre introduced polarisation considerations.	After passage through the EOM the output power was reduced by 95% from approximately 20mW to 1mW. The lack of polarisation maintaining (PM) fibre pigtailed to the laser (as evidenced from tests in section 6.3.4) resulted in performance limiting artefacts in pathlength measurements.
(+) More efficient data acquisition through the use of synchronous signal generation and detection, i.e. using an FPGA which is	Even though the output signals were weak, referencing to the FPGA internal clock meant that phase shifts could still be

capable of performing multiple tasks simultaneously.	identified.
(-) Potential for crosstalk between FPGA channels, low throughput may deviate further.	Initial conceptual experiments (not detailed in this thesis) suggested that the use of an adjacent logic block on the FPGA for a reference channel may introduce cross talk between the channels.
(+) No reference gas cell needed to quantify the pathlength (-) Need a calibration distance and so source and detector have to be removed from the sphere each time a calibration is made.	As the techniques are temporal based can reference to some known distance. This introduces design considerations; it may be possible to have an alternative reference channel but cross-talk (as mentioned in the previous comment) may be an issue.

For testing the effect of contamination, creation of the tabs in the way that they were was useful as it was a methodology that could be applied to both techniques. The tabs were easily created using tweezers to affix the loop to tab. Placement of the tabs was somewhat more challenging as the opening through which the tabs were to be inserted was not very large, as seen in Figure 7.1.

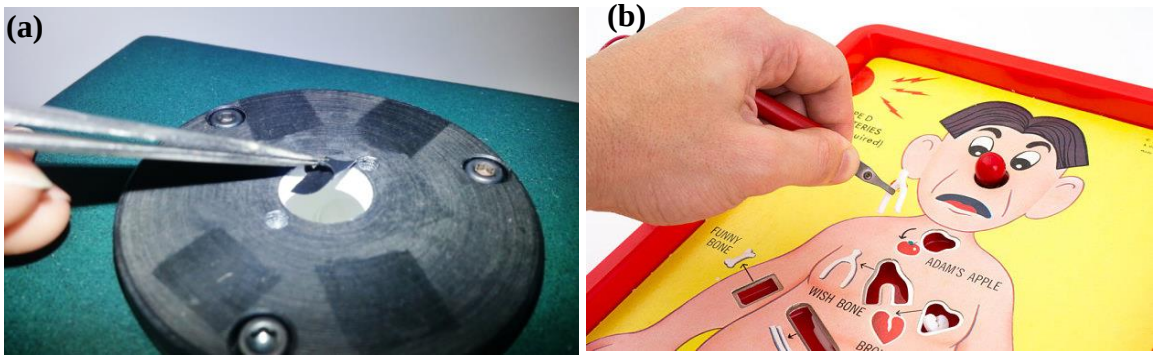

Figure 7.1: (a) Example of how contamination tabs were placed into the sphere (Not actual sphere used). (b) Suggested preparatory training for use of this technique.

On a more general note inducing contamination in this way, due to its ease of creation i.e. no specialist equipment it provides a useful tool for comparison of techniques within different sensors systems or across different research groups.

In terms of the usefulness of these two pathlength calibration techniques, it is the opinion of the author that if only one technique were to be pursued, the phase detection technique in Chapter 6 has more promise commercially. From a design point of view, all of the complexity is in the electronics that are used and so this allows for more flexibility at the detection end of the system, unlike the ratiometric technique where alignment must be maintained in a certain configuration to work. From a measurement point of view, a longer pathlength is achievable due to the presence of less port openings, coupled with increased sensitivity due to the use of high frequency modulation. Table 7.3 revisits the specific performance targets that were mentioned in section 3.3 and provides a summary of how these targets have been/could be achieved for both techniques. In some cases, the performances are common to both techniques and so the comments are merged.

Table 7.3: Summary of performance targets, as outlined in Chapter 3 and how they translated for the two techniques i.e. ratiometric and phase detection.

Ratiometric technique	**Phase detection technique**
Achievable pathlength (1-2m with a 5cm sphere)	
6 port openings – ≈1m effective pathlength. The necessity for two additional ports for this scheme reduces the effective pathlength	4 port openings – ≈1.5m effective pathlength. Effective pathlength has a dependency on modulation frequency
Limit of detection (ideally low ppm 1-10ppm)	
≈60ppm. It is expected that the low ppm level could be achieved with the additional use of wavelength modulation	
Selectivity	
In the lab environment, no cross-interferents were present at 1650nm wavelength.	
Response time (ideally 30-40sec max)	
This was achievable using active pumping. However at lower concentrations it may be necessary to introduce more averaging to increase the SNR	

Accuracy and precision – (Ideally ±5%). Long term repeatability was not tested.	
It is expected that there is potential for greater error in this technique as the algorithm incorporates four beam path measurements. That being said, for minimal contamination, an accuracy of ±5% should be achievable.	It is envisaged that once the polarisation interference has been solved that the main source of error will come from electronic pick-up e.g. from the mains or cross talk within the FPGA itself.
Pathlength calculation	
Initial pathlength was calculated in the lab using a reference gas cell	All pathlength measurements could be made in real time and independent of a reference gas cell.
Cost (currently both techniques are comparable ≈£3-4k)	
Two laser sources and two detectors are the major cost, could be replaced by one laser and a circulator	Electronics are very cost effective, the modulator contributes the largest cost but could be removed by using direct modulation
Maintenance - alignment and cleaning.	
Once beam divergence is set, the alignment is trivial, However the alignment needs to be maintained throughout use, as results are related to initial calibration. As port openings are threaded it is envisaged that, in the event of cleaning, a non-technical operator would be acceptable.	As all light propagation is through fibre and source is attached using a port adaptor, alignment is trivial, and any deviation in beam alignment is not an issue as a corresponding pathlength measurement can be made for each gas measurement.
Material is PTFE based and can be cleaned with water and sanding.	
Ease of use – calibration and operation	
Once acceptable contamination limits are established it is intended that, in the event of excessive contamination, the system would alarm to notify the user. For the ratiometric scheme the contamination location e.g. window or sphere wall could also be identified. Both systems can be controlled and activated by computer and so technical expertise would not be required.	

7.2 Outlook

The aim of this thesis was to investigate possible methods for pathlength calibration of an integrating sphere. Though the principles of the two techniques have been demonstrated here there has been limited work into how this translates in practise i.e. what contamination would the system actually be subjected to and for how long the systems would operate accurately.

Both techniques have a number of challenges that need to be overcome before testing a prototype in a more representative and challenging environment. For the four beam technique, it was found that there were a number of locations where contamination seriously degrades the problem. However the dataset for each of these contamination tests was quite small with severe contamination implemented and so the tested scenarios may be exaggerated. Further testing is needed to gain an idea of the extent of the potential error contribution at these locations in terms of factors such as magnitude of particulate contamination that could be tolerated. The contribution made here allows for those locations to be targeted in testing. From a detection capability point of view, it would be useful to employ modulation techniques to enhance the sensitivity of the system. Additionally the use of fibre input/outputs would allow for smaller port openings thus somewhat compensating for the loss of pathlength that has been seen as a result of 6 port openings. These challenges and potential test strategies are listed below in Table 7.4

Table 7.4: A list of some of the challenges for the four beam technique for the future and potential strategies to address these

Future challenges	Suggested experimental tests
Sphere window contamination cannot be corrected for (Table 5.3 highlights the severity of errors due to particulate contamination. Absorption error Smaller particles ≈13% error Larger particles (mm) ≈70% error	Introduce a number of varying size particulate contamination to sphere window(s) to ascertain to what extent contamination can be tolerated For field test: Introduce a particulate filter to the gas line, monitor short paths as indicators of contamination

First strike spot (FSS) contamination cannot be corrected for (Table 5.5 highlights how FSS contamination affects each diffuse path) % drop in output power due to FSS 2 contamination Long path 1 ≈12% Long path 2 ≈63%	Ascertain to what extent FSS contamination can be tolerated. In field test: monitor comparative change in long paths as means of ascertaining whether FSS contamination specifically has occurred.
Enhancing sensitivity for lower concentration measurements	Employment of modulation techniques e.g. in combination with phase detection system in Chapter 6 Reduction of port sizes (using fibre input and outputs) Reduction of ports (use a two beam setup if component variation is not an issue)

Regarding the phase detection techniques, the immediate considerations relate to the systematic errors. These include polarisation related artefacts and low power throughput and so initial work would aim to alleviate these through use of polarisation maintaining fibre and direct modulation respectively. In terms of its application as a method for calculating the pathlength a next step would look at how to utilise the modulation frequency dependency of the phase shift to calibrate the sphere e.g. potentially a unique calibration curve may result for each gas concentration. Regarding sensitivity enhancement there are a number of modulation strategies that could be implemented. Whilst the high frequency modulation can provide a quantitative measure of the pathlength, a lower frequency modulation could allow for wavelength modulation spectroscopy to be implemented providing quantitative measurement of the gas absorption concentration. The combination of this with an even lower frequency ramp waveform would facilitate scanning over the whole gas absorption line (as was done in

Chapter 5) thus achieving a reference off gas line measurement. Some of the challenges for the future as well as potential experimental strategies are listed below in Table 7.5.

Table 7.5: A list of some of the challenges for the phase detection technique for the future and potential strategies to address these

Future challenges	Suggested experimental tests
Performance limiting polarisation related artefacts due to the use of a laser with pigtailed single mode fibre	Replace the single mode fibre with polarisation maintaining fibre and align to EOM eigen-axes
Severe reduction in output power due to the use of the EOM	Directly modulate the laser, this would also eliminate any polarisation dependency
Potential cross talk from other FPGA channels	Investigate the relationship between two signals acquired on the same FPGA, such as at what power output additional channels become an issue
Enhancing sensitivity for lower concentration measurements	Use of other filters would allow for higher frequencies of detection. Addition of other modulation at lower frequencies simultaneously could facilitate independent measurement strategies for each aspect of the system i.e. off-gas line measurement accounting for external ambient effects, lower frequency 2f-WMS to measure gas line properties including broadening etc

In summary, the ultimate objective would be to realise two techniques for pathlength calibration that culminate in an optical gas sensor that meets some of the criteria mentioned in Chapter 1; selectivity to the gas of interest, achieving desired sensitivity for the application, ease of operation, relatively low cost and robustness. The work to date has made progress in achieving enhanced sensitivity and investigating steps to make the optical system more reliable and robust. Future work would focus on overcoming the systematic limitations that have been encountered and then validating the principles of the techniques in a more representative environment.

List of publications and outcomes

The following publications and other outcomes have resulted from the work presented in this thesis:

Journal papers

- S. Bergin, J. Hodgkinson, D. Francis, and R. P. Tatam, "Integrating cavity based gas cells: a multibeam compensation scheme for pathlength variation," Opt. Express, **24**, 13647-13664 (2016)

Conference papers

- S. Bergin, J. Hodgkinson, D. Francis, R. P. Tatam, "A method for continuous in-situ pathlength calibration of integrating sphere based gas cells," . Proc. SPIE 9486, Advanced Environmental, Chemical, and Biological Sensing Technologies XII, 94860G (May 13, 2015); doi:10.1117/12.2176225.

Further conference participation

- S. Bergin, J. Hodgkinson, D. Francis, R. P. Tatam, "Integrating spheres as gas cells: continuous in-situ pathlength calibration for methane monitoring". Poster presentation at *Photon14*, London, UK, 2014
- S. Bergin, J. Hodgkinson, D. Francis, R. P. Tatam, "In-situ pathlength calibration of integrating sphere based gas cells in industrial environments". Poster presentation at Female Researcher Network (FeRN) Annual Lecture at Cranfield, UK, 2015 (received *highly recommended* award)

- S. Bergin, T Kissinger, J. Hodgkinson, R. P. Tatam, “High frequency modulation techniques for pathlength calibration of an integrating sphere used in TDLS”, Presentation accepted for Flair16, Aix les Bains, France, 2016
- S. Bergin, T Kissinger, J. Hodgkinson, R. P. Tatam “Integrating cavity absorption spectroscopy system using FPGA based detection”, Presentation accepted for Photon16, Leeds, UK, 2016

Patent application

- S. Bergin, J. Hodgkinson, D. Francis, R. P. Tatam, “In-situ pathlength calibration for integrating cavities”, *Patent application,* GB1506609.5, 2015

Research Grants

- J. Hodgkinson, S. Bergin, R.P. Tatam, “Novel approaches to optical gas detection for environmental measurements in challenging locations”, Impact Acceleration Account Early Stage Support Funding, 6 months, 2016.

Further Achievements

- Awarded 1st place for for a Dragons’ Den style pitch at an entrepreneur Startup weekend at the Bettany Centre, Cranfield University, 2015

Appendix A: FPGA based processing

An FPGA is a silicon chip that has reprogrammable circuitry, giving the user the ability to reconfigure functionality in the field after manufacture. The device contains a number of configurable logic blocks, with electrically programmable interconnects between these blocks. This allows the logic blocks to be programmed in any configuration to achieve the desired functionality. Dedicated hardware logic will be assigned to each task and so multiple tasks can be performed in parallel by assigning different parts of the chip to different tasks. This differs from a central processor unit (CPU) based system, such as those in a regular computer, where the operating system instructs the processor to execute the functions sequentially. Due to this sequential method, increasing the number of functions can decrease their respective performance speed due to the increased number of operations to be processed by the CPU. By contrast, concurrently running functions in an FPGA operate independently of each other and so do not share processing resources. In FPGA the circuitry is synchronous and so all tasks occur at the same time, dependent on the chosen clock frequency.

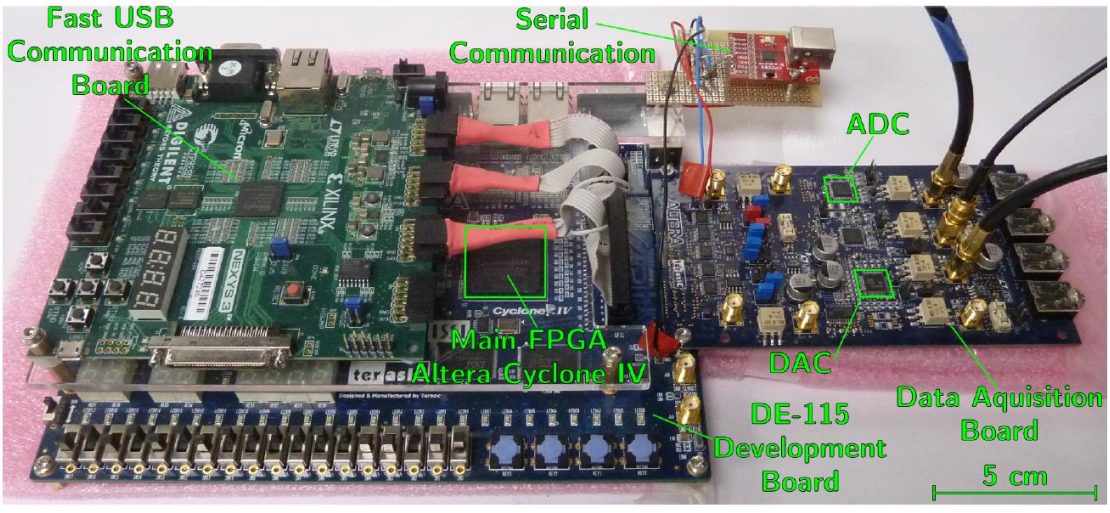

Figure A.1: Picture of the FPGA system used in this work. Picture from [182]

Appendix B: Electro optic modulator datasheet

Description

The 10 Gbits/s Electro-Optic Modulator is designed for long-wavelength, single-mode external amplitude modulation applications. It uses an integrated Mach-Zehnder configuration to convert single polarization CW light from a semiconductor (DFB) laser into a time-varying optical output signal. Agere Systems Inc. also offers a 10 mW CW laser with polarization-maintaining fiber (D2525P) to use as a source for the modulator.

The Ti-diffusion process is a standard feature on all modulator devices. The 2623N, 2623Y, and 2623CS are single-drive, 10 Gbits/s modulators; the 2623CSA is a single-drive, 10 Gbits/s modulator with an attenuating section. Variable attenuation to >19 dB is achieved through a dc bias voltage.

The package is hermetic to protect the $LiNbO_3$ die from the environment. Novel processing techniques now make it possible to achieve 20-year operation with little drift in the dc bias point. The modulator is tested to, and meets the intent of TR-NWT-00468.

Other standard features include PANDA-type polarization-maintaining fiber (PMF) for the optical input (all codes) and output (2623N, 2623Y, and 2623C) fiber with FC-type connectors that are keyed to the axis of polarization. Custom designs are available.

Absolute Maximum Ratings

Stresses in excess of the absolute maximum ratings can cause permanent damage to the device. These are absolute stress ratings only. Functional operation of the device is not implied at these or any other conditions in excess of those given in the operational sections of the data sheet. Exposure to absolute maximum ratings for extended periods can adversely affect device reliability.

Parameter	Symbol	Min	Max	Unit
Storage Temperature	T_{stg}	–40	85	°C
Optical Input Power @ 1.5 μm	P_{IN}	—	30	mW
RF Voltage (peak to peak)	V_{RF}	—	10	V
dc Voltage (RF input)	V_{dcRF}	–20	20	V
dc Voltage (Attenuator input)	V_{dcATT}	–25	25	V
Operating Temperature	T_{OP}	0	70	°C

Optical/Electrical Characteristics

Table 1. Optical/Electrical Characteristics

Parameter	Min	Typ	Max	Unit
Operating Wavelength:				
C-band	1525	—	1565	nm
L-band	1565	—	1620	nm
Insertion Loss:				
2623N, 2623Y, 2623CS	3	3.7	5.5	dB
2623CSA	3.5	4.5	6.5	dB
Extinction Ratio @ dc	20	27	—	dB
Extinction Ratio @ RF	—	13	—	dB
S11 Optical Return Loss	—	—	–35	dB
Bandwidth*	8	10	—	GHz
Drive Voltage ($V\pi$) @ dc	2.8	3.1	4.0	V
Drive Voltage ($V\pi$) @ 1 GHz	3.5	4.1	5.0	V
Attenuation Voltage @ –19 dB	15	19	22	V
Electrode Impedance	—	43	—	Ω
S11 Electrical Return Loss (0.13 GHz—5 GHz)	—	–15	–13	dB
S11 Electrical Return Loss (5 GHz—10 GHz)	–	–14	–12	dB
S11 Electrical Return Loss (10 GHz—18 GHz)	—	–8	–6	dB

* Bandwidth stated is electrical-optical-electrical as determined by the ratio of the received RF electrical power (at a photodiode) relative to the RF electrical power used to drive the modulator. This response is referenced to the value at 130 MHz.

Optical/Electrical Characteristics (continued)

Electrical Signal Input

Electrical signal input is made through SMA coaxial connectors. The standard device includes an internal termination network. Care must be taken not to exceed the recommended 8 in./lb. of torque when making connections to these inputs. High-frequency coaxial cable is recommended.

Characteristic Curves

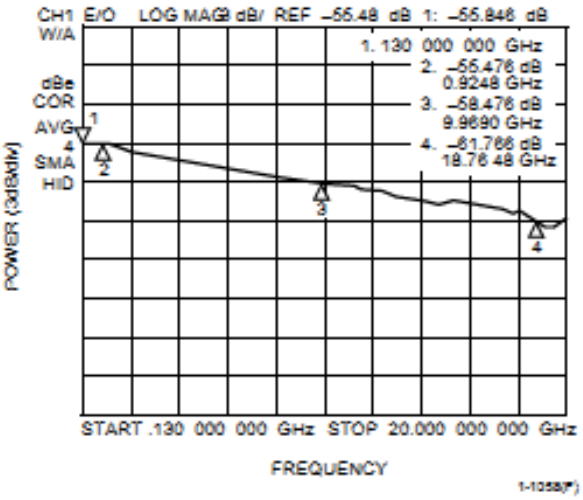

Figure 3. Magnitude of Electro-Optic Response, 0.130 GHz—20 GHz.

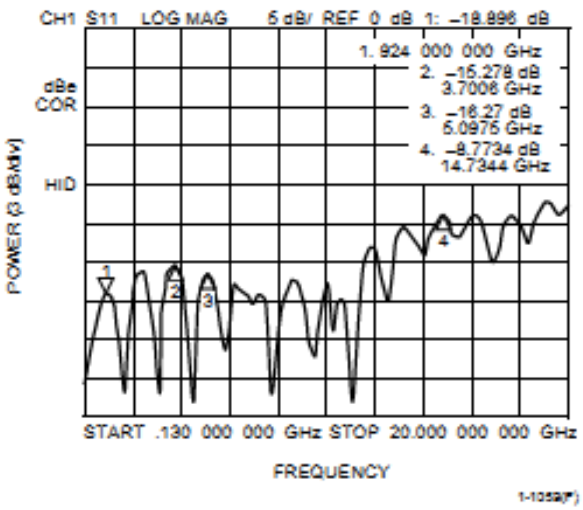

Figure 4. S11, 0.130 GHz—20 GHz

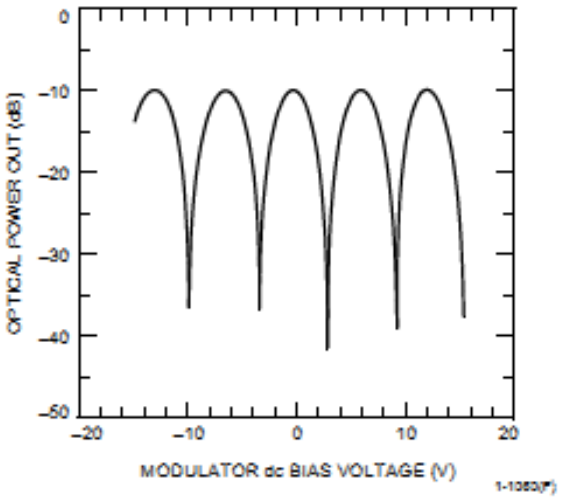

Figure 5. Output Power vs. Bias Voltage

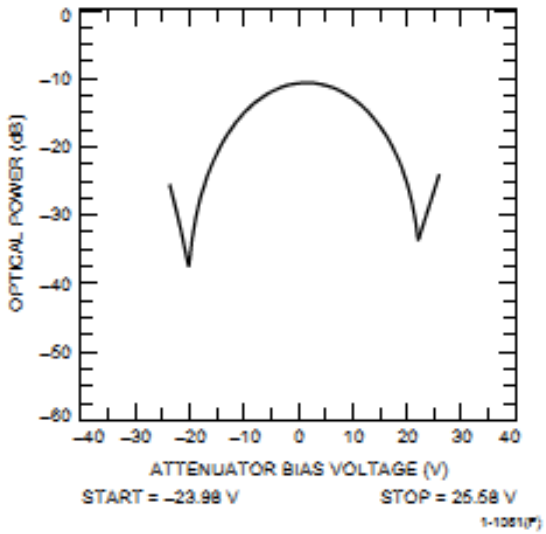

Figure 6. Optical Power vs. Attenuator Bias Voltage

References

[1] R. Pachauri and L. Meyer, "Summary Chapter for Policymakers," IPCC, 2014: Climate Change 2014: Synthesis Report. Contribution of Working Groups I, II and III to the Fifth Assessment Report of the Intergovernmental Panel on Climate Change, 2014.

[2] Transparency Market Research, "Gas Sensors Market - Global Industry Size, Share, Trends, Analysis and Forecast, 2012 - 2018," U.S.A, 2013.

[3] European Parliament, "Directive 2009/29/EC of the European Parliament and of the council of 23 April 2009 amending Directive 2003/87/EC so as to improve and extend the greenhouse gas emission allowance trading scheme of the community," Office Journal of the European Union, Report No. OJ L 129, 2009.

[4] E. J. Dlugokencky, L. M. P. Bruhwiler, J. W. C. White, L. K. Emmons, P. C. Novelli, S. A. Montzka, K. A. Masarie, P. M. Lang, A. M. Crotwell, J. B. Miller, and L. V Gatti, "Observational constraints on recent increases in the atmospheric CH4 burden ," *Geophys. Res. Lett.*, vol. 36, no. 18, p. L18803, 2009.

[5] P. Bousquet, B. Ringeval, I. Pison, E. J. Dlugokencky, E.-G. Brunke, C. Carouge, F. Chevallier, A. Fortems-Cheiney, C. Frankenberg, D. A. Hauglustaine, P. B. Krummel, R. L. Langenfelds, M. Ramonet, M. Schmidt, L. P. Steele, S. Szopa, C. Yver, N. Viovy, and P. Ciais, "Source attribution of the changes in atmospheric methane for 2006–2008," *Atmos. Chem. Phys.*, no. 11, p. 3689, 2011.

[6] R. W. Bogue, "Technology roadmap: Optoelectronic gas sensors in the petrochemicals, gas and water industries," *Optocem.net*, 2006. [Online]. Available: http://userweb.eng.gla.ac.uk/charles.ironside/QCSENSEPrivate/GasSensinRoadmap.pdf. [Accessed: 01-Dec-2015].

[7] A. Morrow, "2016 Arctic Sea Ice Wintertime Extent Hits Another Record Low," *http://www.nasa.gov/*, Mar-2016. [Online]. Available:

http://www.nasa.gov/feature/goddard/2016/2016-arctic-sea-ice-wintertime-extent-hits-another-record-low#.V08CEqFznbI.mendeley. [Accessed: 01-Jun-2016].

[8] UNFCCC. Secretariat, "Report of the Conference of the Parties on its twenty-first session, held in Paris from 30 November to 13 December 2015. Part one: Proceedings.," 2016.

[9] Getty images, "Storm Desmond: New group to examine flood protection," *BBC*, 2015. [Online]. Available: http://ichef-1.bbci.co.uk/news/660/cpsprodpb/422A/production/_87183961_87183960.jpg. [Accessed: 15-Feb-2016].

[10] S. J. O'Shea, G. Allen, Z. L. Fleming, S. J.-B. Bauguitte, C. J. Percival, M. W. Gallagher, J. Lee, C. Helfter, and E. Nemitz, "Area fluxes of carbon dioxide, methane, and carbon monoxide derived from airborne measurements around Greater London: A case study during summer 2012," *J. Geophys. Res. Atmos.*, vol. 119, no. 8, pp. 4940–4952, Apr. 2014.

[11] Crowcon, "Hydrogen Sulphide: toxic and deadly – Chris explains more about this dangerous gas," *Blog article*, 2014. [Online]. Available: http://www.crowcon.com/blog/hydrogen-sulphide-toxic-and-deadly-chris-explains-more-about-this-dangerous-gas/. [Accessed: 01-May-2016].

[12] D. J. Wuebbles and K. Hayhoe, "Atmospheric methane and global change," *Earth-Science Rev.*, vol. 57, no. 3–4, pp. 177–210, 2002.

[13] O. Edenhofer, R. Pichs-Madruga, Y. Sokona, E. Farahani, S. Kadner, K. Seyboth, A. Adler, I. Baum, S. Brunner, P. Eickemeier, B. Kriemann, J. Savolainen, S. Schlömer, C. von Stechow, T. Zwickel, and J. C. Minx, *Contribution of Working Group III to the Fifth Assessment Report of the Intergovernmental Panel on Climate Change*, vol. AR5. Cambridge: Cambridge University Press, 2014.

[14] DVGW German Technical and Scientific Association for Gas and Water, "Mastering future challenges with gas innovations Intelligent technologies for the energy transition," Gas brochure, 2014.

[15] R. T. Watson, “Climate Change 2001: Synthesis Report. A Contribution of Working Group 1, 2 and 3 to the Third Assessment Report of the Intergovernmental Panel on Climate Change,” Cambridge University Press, New York, 2001.

[16] H. F. Coward and G. W. Jones, “Limits of Flammability of Gases and Vapors,” U.S. Government Printing Office, Washington D.C., Bulletin 5, 1952.

[17] D. J. Zimmerle, L. L. Williams, T. L. Vaughn, C. Quinn, R. Subramanian, G. P. Duggan, B. Willson, J. D. Opsomer, A. J. Marchese, D. M. Martinez, and A. L. Robinson, “Methane Emissions from the Natural Gas Transmission and Storage System in the United States.,” *Environ. Sci. Technol.*, vol. 49, no. 15, pp. 9374–83, Aug. 2015.

[18] U. S. E. Information, “Henry Hub natural gas spot price,” *http://www.eia.gov/*, 2015. [Online]. Available: http://www.eia.gov/dnav/ng/hist/rngwhhdd.htm. [Accessed: 18-Aug-2015].

[19] Energy Information Administration, “About U.S. Natural Gas Pipelines – Transporting Natural Gas,” *Natural gas*, 2007. [Online]. Available: http://www.eia.gov/pub/oil_gas/natural_gas/analysis_publications/ngpipeline/fullversion.pdf. [Accessed: 01-Aug-2015].

[20] J. Hodgkinson and R. P. Tatam, “Optical gas sensing: a review,” *Meas. Sci. Technol.*, vol. 24, no. 1, p. 12004, 2013.

[21] J. B. McManus, J. H. Shorter, D. D. Nelson, and M. S. Zahniser, “Compact Quantum Cascade Laser Instrument for Rapid, High Sensitivity Measurements of Trace Gases in Air,” *Sensors, 2007 IEEE*. pp. 1341–1344, 2007.

[22] D. S. Baer, J. B. Paul, M. Gupta, and A. O’Keefe, “Sensitive absorption measurements in the near-infrared region using off-axis integrated-cavity-output spectroscopy,” *Appl. Phys. B*, vol. 75, no. 2, p. 261, 2002.

[23] H. Nasim and Y. Jamil, “Recent advancements in spectroscopy using tunable diode lasers,” *Laser Phys. Lett.*, vol. 10, p. 43001, 2013.

[24] S. Tranchart, I. H. Bachir, and J. L. Destombes, “Sensitive trace gas detection

with near-infrared laser diodes and an integrating sphere," *Appl. Opt.*, vol. 35, no. 36, p. 7070, 1996.

[25] Toptica Photonics AG, "Product Specification. Compact Herriott cell for absorption spectroscopy: CMP-30," *Toptica*, 2009. [Online]. Available: www.toptica.com.

[26] P. Elterman, "Integrating Cavity Spectroscopy," *Appl. Opt.*, vol. 9, no. 9, p. 2140, Jan. 1970.

[27] Transparency Market Research, "Gas Detection Equipment Market (Fixed Gas Detection Equipment and Portable Gas Detection Equipment) - Global Industry Analysis, Size, Share, Growth, Trends, and Forecast 2014 - 2022," 2015.

[28] Z. Yunusa, M. N. Hamidon, A. Kaiser, and Z. Awang, "Gas Sensors: A Review," *Sensors and Transducers*, vol. 168, p. 61, 2014.

[29] S. T. Hussain, "Getting Sensitised to Sensors," *Climate control Middle East-perspectives*, 2014. [Online]. Available: http://climatecontrolme.com/2014/08/getting-sensitised-to-sensors/. [Accessed: 26-Jul-2016].

[30] J. R. Saffell, M. L. Hitchman, and D. H. Dawson, "Electrochemical sensor for determining analyte in the presence of interferent and method of using the sensor." Google Patents, 2003.

[31] Z. Wang, M. Guo, G. A. Baker, J. R. Stetter, L. Lin, A. J. Mason, and X. Zeng, "Methane-oxygen electrochemical coupling in an ionic liquid: a robust sensor for simultaneous quantification," *Analyst*, vol. 139, no. 20, pp. 5140–5147, 2014.

[32] Alphasense Ltd., "NO2-A43F Nitrogen Dioxide Sensor 4-Electrode," *Technical specification*, 2016. [Online]. Available: http://www.alphasense.com/WEB1213/wp-content/uploads/2016/04/NO2-A43F.pdf. [Accessed: 20-Mar-2016].

[33] R. Rajaram, F. Z. Siddiqui, and M. E. Khan, *From Landfill Gas to Energy: Technologies and Challenges*. CRC Press, 2011.

[34] J. Sharaf, “Exhaust emissions and its control technology for an internal combustion engines,” *Int. J. Eng. Res. Appl.*, vol. 3, no. 5, 2013.

[35] I. G. McWilliam and R. A. Dewar, “Flame Ionization Detector for Gas Chromatography,” *Nature*, vol. 181, no. 4611, p. 760, Mar. 1958.

[36] UCDavis ChemWiki, “Gas Chromatography,” *UCDavis ChemWiki*, 2016. [Online]. Available: http://chemwiki.ucdavis.edu/Textbook_Maps/Analytical_Chemistry_Textbook_Maps/Map:_Analytical_Chemistry_2.0_(Harvey)/12_Chromatographic_and_Electrophoretic_Methods/12.4:_Gas_Chromatography. [Accessed: 26-Jul-2016].

[37] RAE systems, “COMPARISON OF PHOTOIONIZATION DETECTORS (PIDS) AND FLAME IONIZATION DETECTORS (FIDS),” *Application note*. [Online]. Available: http://www.raesystems.com/sites/default/files/content/resources/Application-Note-226_Comparison-Of-Photoionization-Detectors-%5BPIDs%5D-And-Flame-Ionization-Detectors-(FIDs)_01-04.pdf. [Accessed: 01-Feb-2016].

[38] G. Korotcenkov, “Metal oxides for solid-state gas sensors: What determines our choice?,” *Mater. Sci. Eng. B*, vol. 139, no. 1, p. 1, 2007.

[39] P. Bhattacharyya, K. P. Basu, N. Mukherjee, A. Mondal, H. Saha, and S. Basu, “Deposition of nanocrystalline ZnO thin films on p-Si by novel galvanic method and application of the heterojunction as methane sensor,” *J. Mater. Sci. Mater. Electron.*, vol. 18, no. 8, p. 823, 2007.

[40] G. K. Flingelli, M. M. Fleischer, and H. Meixner, “Selective detection of methane in domestic environments using a catalyst sensor system based on Ga2O3,” *Sensors Actuators B Chem.*, vol. 48, no. 1–3, p. 258, May 1998.

[41] F. Quaranta, R. Rella, P. Siciliano, S. Capone, M. Epifani, L. Vasanelli, A. Licciulli, and A. Zocco, “A novel gas sensor based on SnO2/Os thin film for the detection of methane at low temperature,” *Sensors Actuators B Chem.*, vol. 58, no. 1–3, pp. 350–355, Sep. 1999.

[42] C. N. Banwell and E. M. McCash, *Fundamentals of molecular spectroscopy*, 4th

ed. London: The McGraw-Hill Companies, 1994.

[43] J. J. Davenport, J. Hodgkinson, J. R. Saffell, and R. P. Tatam, “Formaldehyde sensor using non-dispersive UV spectroscopy at 340nm,” in *Proc. of SPIE*, 2014, vol. 9141, p. 91410K.

[44] G. Stewart, “Fiber optic sensors in environmental monitoring,” in *Optical Fiber Sensor Technology: Volume 4: Chemical and Environmental Sensing*, K. T. V Grattan, L. S. Grattan, and B. T. Meggitt, Eds. The Netherlands: Kluwer Academic Publishers, 1999, pp. 87–111.

[45] J. S. Margolis, “Measured line positions and strengths of methane between 5500 and 6180 cm-1,” *Appl. Opt.*, vol. 27, no. 19, p. 4038, 1988.

[46] R. R. Gamache and J. Lamouroux, “The vibrational dependence of half-widths of CO2 transitions broadened by N2, O2, air, and CO2,” *J. Quant. Spectrosc. Radiat. Transf.*, vol. 117, p. 93, Mar. 2013.

[47] C. J. Wallace, C. Jeon, C. N. Anderson, and D. K. Havey, “H2O Broadening of a CO2 Line and Its Nearest Neighbors Near 6360 cm–1,” *J. Phys. Chem. A*, vol. 115, no. 47, pp. 13804–13810, Dec. 2011.

[48] I. Sieber and U. Gengenbach, “Design and optimization of optical gas sensor systems,” in *Chemical Sensors: Simulation and Modeling Volume 4: Optical Sensors, Volume 4*, G. . Korotcenkov, Ed. New York: Momentum Press, 2013, pp. 418–427.

[49] M. Peach, “Mid-IR laser sales growing 4x faster than total laser market,” *Optics.org: The business of Photonics*, 2014.

[50] Nato Science for peace and security, *Mid-Infrared Coherent Sources and Applications*. The Netherlands: Springer Science & Business Media, 2008.

[51] L. R. Brown, K. Sung, D. C. Benner, V. M. Devi, V. Boudon, T. Gabard, C. Wenger, A. Campargue, O. Leshchishina, S. Kassi, D. Mondelain, L. Wang, L. Daumont, L. Régalia, M. Rey, X. Thomas, V. G. Tyuterev, O. M. Lyulin, A. V. Nikitin, H. M. Niederer, S. Albert, S. Bauerecker, M. Quack, J. J. O’Brien, I. E. Gordon, L. S. Rothman, H. Sasada, A. Coustenis, M. A. H. Smith, T. Carrington,

X.-G. Wang, A. W. Mantz, and P. T. Spickler, “Methane line parameters in the HITRAN2012 database,” *J. Quant. Spectrosc. Radiat. Transf.*, vol. 130, p. 201, Nov. 2013.

[52] A. Thorne, U. Litzén, and S. Johansson, “The width and shape of spectral lines,” in *Spectrophysics: Principles and Applications*, Springer Berlin Heidelberg, 1999, pp. 189–195.

[53] H. I. Schiff, G. I. Mackay, J. Bechara, and J. and Bechara, “The use of tunable diode laser absorption spectroscopy for atmospheric measurements,” in *Air monitoring by spectroscopic techniques*, M. W. Sigrist, Ed. New York: John Wiley and sons, 1994, pp. 239–333.

[54] J. D. Ingle Jr and S. R. Crouch, *Spectrochemical analysis*. Englewood Cliffs, N.J: Prentice Hall, 1988.

[55] X. Huang and Y. L. Yung, “A common misunderstanding about the Voigt line profile,” *J. Atmos. Sci.*, vol. 61, no. 13, p. 1630, 2003.

[56] A. D. McNaught and A. Wilkinson, *IUPAC. Compendium of chemical terminology*, vol. 2nd. Oxford: Blackwell Scientific Publications, 2006.

[57] P. Matejka, B. Vlckova, L. Bednarova, and P. Malon, “Introduction to principles and analytical aspects of optical spectroscopy,” in *Natural Products Analysis: Instrumentation, Methods, and Applications*, V. Havlicek and S. Jaroslav, Eds. U.S.A: John Wiley & Sons, Ltd, 2014, p. 163.

[58] C. Massie, G. Stewart, G. McGregor, and J. R. Gilchrist, “Design of a portable optical sensor for methane gas detection,” *Sensors Actuators B Chem.*, vol. 113, no. 2, p. 830, 2006.

[59] S. E. Alexandrov, G. A. Gavrilov, A. A. Kapralov, S. A. Karandashev, B. A. Matveev, G. Y. Sotnikova, and N. M. Stus’, “Portable optoelectronic gas sensors operating in the mid-IR spectral range (λ=3 5 μm),” in *Proc. SPIE 4680*, 2002, vol. 4680, p. 188.

[60] S. B. Reddy, “Infrared non dispersive CO2 analyser working princple,” *Instrumentation tools*, 2015. [Online]. Available:

http://instrumentationtools.com/infrared-non-dispersive-co2-analyzer-working-principle/. [Accessed: 26-Jul-2016].

[61] J. Hodgkinson, R. Smith, W. O. Ho, J. R. Saffell, and R. P. Tatam, "Non-dispersive infra-red (NDIR) measurement of carbon dioxide at 4.2 μm in a compact and optically efficient sensor," *Sensors Actuators B Chem.*, vol. 186, p. 580, 2013.

[62] J. Hodgkinson and R. P. Tatam, "Optical gas sensing: a review," *Meas. Sci. Technol.*, vol. 24, no. 1, p. 012004, 2013.

[63] K. Ruxton, A. L. Chakraborty, W. Johnstone, M. Lengden, G. Stewart, and K. Duffin, "Tunable diode laser spectroscopy with wavelength modulation: Elimination of residual amplitude modulation in a phasor decomposition approach," *Sensors Actuators B Chem.*, vol. 150, no. 1, pp. 367–375, 2010.

[64] D. R. Herriott and H. J. Schulte, "Folded optical delay lines," *Appl. Opt.*, vol. 4, no. 8, p. 883, 1965.

[65] J. B. McManus, M. S. Zahniser, and D. D. Nelson, "Dual quantum cascade laser trace gas instrument with astigmatic Herriott cell at high pass number," *Appl. Opt.*, vol. 50, no. 4, pp. 74–75, 2011.

[66] E. C. Richard, K. K. Kelly, R. H. Winkler, R. Wilson, T. L. Thompson, R. J. McLaughlin, A. L. Schmeltekopf, and A. F. Tuck, "A fast-response near-infrared tunable diode laser absorption spectrometer for in situ measurements of CH4 in the upper troposphere and lower stratosphere," *Appl. Phys. B*, vol. 75, no. 2, pp. 183–194.

[67] M. D. Wheeler, S. M. Newman, A. J. Orr-Ewing, and M. N. R. Ashfold, "Cavity ring-down spectroscopy ," *J. Chem. Soc. - Faraday Trans.*, vol. 94, no. 3, pp. 337–351, 1988.

[68] Picarro, "Cavity Ring-Down Spectroscopy (CRDS)," *Technical note*, 2016. [Online]. Available: http://www.picarro.com/technology/cavity_ring_down_spectroscopy. [Accessed: 26-Jul-2016].

[69] E. Crosson, “WS--CRDS: Precision Trace Gas Analysis and Simplified Stable Isotope Measurements,” *American Laboratory*, 2008.

[70] M. T. Cone, J. A. Musser, E. Figueroa, J. D. Mason, and E. S. Fry, “Diffuse reflecting material for integrating cavity spectroscopy, including ring-down spectroscopy,” *Appl. Opt.*, vol. 54, no. 2, p. 334, 2015.

[71] J. Mason and E. S. Fry, “Integrating cavity ring-down spectroscopy (ICRDS) and the direct measurement of absorption coefficients,” *Phys. Scr.*, vol. 91, no. 4, p. 43004, 2016.

[72] G. S. Engel, W. S. Drisdell, F. N. Keutsch, E. J. Moyer, and J. G. Anderson, “Ultrasensitive near-infrared integrated cavity output spectroscopy technique for detection of CO at 1.57 μm: new sensitivity limits for absorption measurements in passive optical cavities,” *Appl. Opt.*, vol. 45, no. 36, p. 9221, 2006.

[73] D. Baer, M. Gupta, J. B. Leen, and E. Berman, “Environmental and atmospheric monitoring using off-axis integrated cavity output spectroscopy (OA-ICOS).”

[74] J. M. Herbelin, J. A. McKay, M. A. Kwok, R. H. Ueunten, D. S. Urevig, D. J. Spencer, and D. J. Benard, “Sensitive measurement of photon lifetime and true reflectances in an optical cavity by a phase-shift method,” *Appl. Opt.*, vol. 19, no. 1, p. 144, 1980.

[75] V. L. K. and P. A. M. and R. J. Holdsworth, “Phase-shift off-axis cavity-enhanced absorption detector of nitrogen dioxide,” *Meas. Sci. Technol.*, vol. 17, no. 4, p. 923, 2006.

[76] T. Laurila, I. S. Burns, J. Hult, J. H. Miller, and C. F. Kaminski, “A calibration method for broad-bandwidth cavity enhanced absorption spectroscopy performed with supercontinuum radiation,” *Appl. Phys. B*, vol. 102, no. 2, p. 271, 2011.

[77] V. L. Kasyutich, P. A. Martin, and R. J. Holdsworth, “Effect of broadband amplified spontaneous emission on absorption measurements in phase-shift off-axis cavity enhanced absorption spectroscopy,” *Chem. Phys. Lett.*, vol. 430, no. 4–6, p. 429, 2006.

[78] E. Hawe, C. Fitzpatrick, P. Chambers, G. Dooly, and E. Lewis, “Hazardous gas

detection using an integrating sphere as a multipass gas absorption cell," *Sensors Actuators, A Phys.*, vol. 141, no. 2, p. 414, 2008.

[79] J. Hodgkinson, D. Masiyano, R. P. Tatam, J. Hodgkinson, and R. P. Tatam, "Gas cells for tunable diode laser absorption spectroscopy employing optical diffusers. Part 2: Integrating spheres," *Appl. Phys. B Lasers Opt.*, vol. 100, no. 2, p. 291, 2010.

[80] S. Brown, "Analysis of the State of the Art: Infrared Spectroscopy," *Spectrocopy*, 2015.

[81] J. U. White, "Long optical paths of large aperture," *J. Opt. Soc. Am.*, vol. 32, pp. 285–288, 1942.

[82] J. C. M. Antón and M. Silva-López, "Optical cavity for auto-referenced gas detection," *Opt. Express*, vol. 19, no. 27, pp. 26079–26087, 2011.

[83] T. A. Hu, E. L. Chappell, J. T. Munley, and S. W. Sharpe, "Improved multipass optics for diode laser spectroscopy," *Rev. Sci. Instrum.*, vol. 64, no. 12, p. 3380, 1993.

[84] Toptica Photonics, "Multipass cell: Herriott cell for absorption spectroscopy," 2010. [Online]. Available: http://www.toptica.com/uploads/media/toptica_BR_product_catalog_07.pdf.

[85] P. Technologies, "Herriott type cell standard," 2012. [Online]. Available: http://www.photonicstechnologies.com/index.php/gas-cells/herriott-type-cell/cmp-30-st.html.

[86] J. B. McManus, P. L. Kebabian, and M. S. Zahniser, "Astigmatic mirror multipass absorption cells for long-path-length spectroscopy," *Appl. Opt.*, vol. 34, no. 18, p. 3336, 1995.

[87] D. Das and A. C. Wilson, "Very long optical path-length from a compact multi-pass cell," *Appl. Phys. B Lasers Opt.*, no. 103, p. 749, 2011.

[88] W. Gurlit, R. Zimmermann, C. Giesemann, T. Fernholz, V. Ebert, J. Wolfrum, U. Platt, and J. P. Burrows, "Lightweight diode laser spectrometer CHILD

(Compact High-altitude In-situ Laser Diode) for balloon borne measurements of water vapor and methane," *Appl. Opt.*, vol. 44, no. 1, p. 91, 2005.

[89] P. Werle, "Tunable diode laser absorption spectroscopy: recent findings and novel approaches," *Infrared Phys. Technol.*, vol. 37, no. 1, pp. 59–66, Feb. 1996.

[90] J. Ofner, H.-U. Krüger, and C. Zetzsch, "Circular multireflection cell for optical spectroscopy," *Appl. Opt.*, vol. 49, no. 26, pp. 5001–5004, 2010.

[91] D. A. Knox, A. K. King, E. D. McNaghten, S. J. Brooks, P. A. Martin, and S. M. Pimblott, "Novel utilisation of a circular multi-reflection cell applied to materials ageing experiments," *Appl. Phys. B*, vol. 119, no. 1, p. 55, 2015.

[92] R. M. Wynne, K. Creedon, B. Barabadi, S. Vedururu, J. Merritt, and A. Ortega, "Simultaneously sensing multiple gases using a single length of hollow-core photonic bandgap fiber with sub-minute response times," in *Proc. SPIE 7056, Photonic Fiber and Crystal Devices: Advances in Materials and Innovations in Device Applications II*, 2008, vol. 7056, p. 70560W–70560W–11.

[93] C. A. W. and N. A. Gallen, "Trace-level detection of gases and vapours with mid-infra-red hollow waveguides," *J. Phys. D. Appl. Phys.*, vol. 30, no. 14, p. 1984, 1997.

[94] J. Bösenberg and D. J. Brassington, *Instrument Development for Atmospheric Research and Monitoring: Lidar Profiling, DOAS and Tunable Diode Laser Spectroscopy*. Berlin: Springer-Verlag Berlin Heidelberg, 1997.

[95] J. M. Supplee, E. A. Whittaker, and W. Lenth, "Theoretical description of frequency modulation and wavelengthmodulation spectroscopy," *Appl. Opt.*, vol. 33, no. 27, pp. 6294–6302, 1994.

[96] D. S. Bomse, A. C. Stanton, and J. A. Silver, "Frequency modulation and wavelength modulation spectroscopies: comparison of experimental methods using a lead salt laser," *Appl. Opt.*, vol. 31, no. 6, p. 718, 1992.

[97] D. Masiyano, "Use of diffuse reflections in tunable diode laser spectroscopy," Cranfield University, 2008.

[98] R. Arndt, “Analytical Line Shapes for Lorentzian Signals Broadened by Modulation,” *J. Appl. Phys.*, vol. 36, no. 8, p. 2522, 1965.

[99] S. Schilt, L. Thevenaz, and P. Robert, “Wavelength modulation spectroscopy: combined frequency and intensity laser modulation,” *Appl. Opt.*, vol. 42, no. 33, pp. 6728–6738, 2003.

[100] T. Fernholz, H. Teichert, and V. Ebert, “Digital, phase-sensitive detection for in situ diode-laser spectroscopy under rapidly changing transmission conditions,” *Appl. Phys. B*, vol. 75, no. 2, p. 229, 2002.

[101] D. T. Cassidy and J. Reid, “Atmospheric pressure monitoring of trace gases using tunable diode lasers,” *Appl. Opt.*, vol. 21, no. 7, p. 1185, 1982.

[102] P. Werle and F. Slemr, “Signal-to-noise ratio analysis in laser absorption spectrometers using optical multipass cells,” *Appl. Opt.*, vol. 30, no. 4, p. 430, 1991.

[103] P. Werle, F. Slemr, M. Gehrtz, and C. Bräuchle, “Wideband noise characteristics of a lead-salt diode laser: possibility of quantum noise limited TDLAS performance,” *Appl. Opt.*, vol. 28, no. 9, pp. 1638–1642, 1989.

[104] P. W. Werle, P. Mazzinghi, F. D’Amato, M. De Rosa, K. Maurer, and F. Slemr, “Signal processing and calibration procedures for in situ diode-laser absorption spectroscopy,” *Spectrochim. Acta Part A Mol. Biomol. Spectrosc.*, vol. 60, no. 8–9, pp. 1685–1705, Jul. 2004.

[105] I. Sergachev, R. Maulini, A. Bismuto, S. Blaser, T. Gresch, Y. Bidaux, A. Müller, S. Schilt, and T. Südmeyer, “All-electrical frequency noise reduction and linewidth narrowing in quantum cascade lasers,” *Opt. Lett.*, vol. 39, no. 22, pp. 6411–6414, 2014.

[106] P. P. Sotiriadis and K. Galanopoulos, “Direct all-digital frequency synthesis techniques, spurs suppression, and deterministic jitter correction,” *IEEE Trans. Circuits Syst. I Regul. Pap.*, vol. 59, no. 5, pp. 958–968, 2012.

[107] W. F. Egan, *Frequency Synthesis by Phase Lock*, 2nd ed. New York: Wiley & Sons Ltd., 1999.

[108] K. Hosseini and M. P. Kennedy, “Maximum Sequence Length MASH Digital Delta Sigma Modulators,” *IEEE Trans. Circuits Syst. I Regul. Pap.*, vol. 54, no. 12, p. 2628, 2007.

[109] T. L. Gradishar and R. E. Stengel, “System and method for introducing dither for reducing spurs in digital-to-time converter direct digital synthesis,” US WO 2006039099 A1, 2006.

[110] I. R. Walker, “Some EMI issues involving cables, including crosstalk between cables,” in *Reliability in Scientific Research Improving the Dependability of Measurements, Calculations, Equipment, and Software*, Cambridge: Cambridge University Press, 2011, pp. 381–382.

[111] E. D. Black, “An introduction to Pound–Drever–Hall laser frequency stabilization,” *Am. J. Phys.*, vol. 69, no. 1, p. 79, 2001.

[112] I. S. Burns, J. Hult, and C. F. Kaminski, “Use of 130Te2 for frequency referencing and active stabilisation of a violet extended cavity diode laser,” *Spectrochim. Acta Part A Mol. Biomol. Spectrosc.*, vol. 63, no. 5, p. 905, 2006.

[113] J. Reid, M. El-Sherbiny, B. K. Garside, and E. A. Ballik, “Sensitivity limits of a tunable diode laser spectrometer, with application to the detection of NO2 at the 100-ppt level,” *Appl. Opt.*, vol. 19, no. 19, pp. 3349–3354, 1980.

[114] C. B. Carlisle, D. E. Cooper, and H. Preier, “Quantum noise-limited FM spectroscopy with a lead-salt diode laser,” *Appl. Opt.*, vol. 28, no. 13, pp. 2567–2576, 1989.

[115] E.-G. Neumann, “Signal transmission through single mode fibers,” in *Single-Mode Fibers: Fundamentals*, H. K. V. Lotsch, Ed. Heidelberg: Springer Berlin Heidelberg, 2013, p. 276.

[116] G. E. Betts, “LiNbO3 external modulators and high performance analog links,” in *RF photonic technology in optical fiber links*, W. S. C. Chang, Ed. UK: Cambridge University Press, 2002, p. 102.

[117] W. Kohsiek, “Water vapor cross-sensitivity of open path H2O/CO2 sensors,” *J. Atmos. Ocean. Technol.*, vol. 17, no. 3, p. 299, 2000.

[118] L. K. Amekudzi, K. Bramstedt, A. Rozanov, H. Bovensmann, and J. P. Burrows, "Retrieval of trace gas concentrations from lunar occultation measurements with SCIAMACHY on ENVISAT," in *New Horizons in Occultation Research: Studies in Atmosphere and Climate*, Berlin, Germany: Springer Berlin Heidelberg, 2009, pp. 87–96.

[119] W. E. Sumpner, "The Diffusion of Light," *Proc. Phys. Soc. London*, vol. 12, no. 1, pp. 10–29, 1892.

[120] R. Ulbricht, "Die Bestimmung der mittleren, raumlichen Lichtintensitat durch nur eine Messung," *Elektrotech. Zeit.*, vol. 29, pp. 595–597, 1900.

[121] "A quick method of measuring light," *Popular Science Monthly*, New York, pp. 848–849, 1916.

[122] Y. Ohno, "Optical metrology for LEDs and solid state lighting," in *Proceedings of SPIE*, 2006, vol. 6046, p. 604625.

[123] Raymax, "Bulb measurement: metering lamps." [Online]. Available: http://www.raymax.nl/en/onderdelen/light-measurements/metering-lamps-and-reflectors/. [Accessed: 06-Jun-2014].

[124] A. H. Taylor, "Measurement of diffuse reflection factors: and a new absolute reflectometer ," *J. Opt. Soc. Am.*, vol. 4, no. 1, p. 9, 1920.

[125] A. C. Hardy and F. H. Perrin, "Photometry," in *The principles of optics*, vol. 1, L. A. DuBridge, Ed. New York, US: McGraw-Hill Book Company Inc., 1932, p. 264.

[126] W. Erb and W. Budde, "Properties of standard materials for reflection," *Color Res. Appl.*, vol. 4, no. 3, p. 113, 1979.

[127] F. Grum and G. W. Luckey, "Optical sphere paint and a working standard of reflectance," *Appl. Opt.*, vol. 7, no. 11, p. 2289, 1968.

[128] F. Grum and T. E. Wightman, "Absolute reflectance of Eastman White Reflectance Standard," *Appl. Opt.*, vol. 16, no. 11, p. 2775, 1977.

[129] D. Wyble, "I need it white! What do I do???," *Avian Technologies LLC*, 2012.

[Online]. Available: http://spectroscopyfaq.blogspot.co.uk/2012/09/i-need-it-white-what-do-i-do.html. [Accessed: 08-Jan-2013].

[130] A. W. Springsteen, "Laser cavity material," US 4912720 A, 1990.

[131] A. Springsteen, "Standards for the measurement of diffuse reflectance – an overview of available materials and measurement laboratories," *Anal. Chim. Acta*, vol. 380, no. 2–3, pp. 379–390, Feb. 1999.

[132] U-Times, "BLANC FIXE -Ultra Fine Grade 298-BT," 2012. [Online]. Available: http://www.u-times.com/en/. [Accessed: 01-Apr-2016].

[133] G. L. McGregor and R. B. Minor, "Thin light reflectant surface and method for making and using same," US5982548 A, 1999.

[134] Labsphere, "A guide to reflectance coatings and materials," *Technical note*, 2012. [Online]. Available: http://www.pro-lite.co.uk/File/Tech_Guide_-_Coatings_&_Materials.pdf. [Accessed: 10-Oct-2015].

[135] Labsphere, "Technical guide: Integrating sphere radiometry and photometry," New Hampshire, 2012.

[136] E. S. Fry, J. Musser, G. W. Kattawar, and P.-W. Zhai, "Integrating cavities: temporal response," *Appl. Opt.*, vol. 45, no. 36, p. 9053, 2006.

[137] I. Fecht and M. Johnson, "Non-contact, scattering-independent water absorption measurement using a falling stream and integrating sphere," *Meas. Sci. Technol.*, vol. 10, p. 612, 1999.

[138] R. M. Pope, E. S. Fry, R. L. Montgomery, and F. M. Sogandares, "Integrating cavity absorption meter: measurement results," in *Ocean Optics X*, 1990, vol. 1302, pp. 165–175.

[139] E. S. Fry, G. W. Kattawar, and R. M. Pope, "Integrating cavity absorption meter," *Appl. Opt.*, vol. 31, no. 12, p. 2055, 1992.

[140] A. G. Mignani, L. Ciaccheri, N. Daz-Herrera, A. A. Mencaglia, H. Ottevaere, H. Thienpont, S. Francalanci, and A. P. F. S. Pavone, "Optical fiber spectroscopy for measuring quality indicators of lubricant oils," *Meas. Sci. Technol.*, vol. 20,

no. 3, p. 34011, 2009.

[141] A. Mignani, L. Ciaccheri, H. Ottevaere, H. Thienpont, L. Conte, M. Marega, A. Cichelli, C. Attilio, and A. Cimato, "Visible and near-infrared absorption spectroscopy by an integrating sphere and optical fibers for quantifying and discriminating the adulteration of extra virgin olive oil from Tuscany," *Anal. Bioanal. Chem.*, vol. 399, no. 3, pp. 1315–1324, 2011.

[142] P. Wiśniewska, T. Dymerski, W. Wardencki, and J. Namieśnik, "Chemical composition analysis and authentication of whisky," *J. Sci. Food Agric.*, vol. 95, no. 11, pp. 2159–2166, Aug. 2015.

[143] C. G. Venkatesh, R. S. Eng, and A. W. Mantz, "Tunable diode laser - Integrating sphere systems: A study of their output intensity characteristics.," *Appl. Opt.*, vol. 19, no. 10, pp. 1704–1710, 1980.

[144] E. Berger, D. W. T. Griffith, G. Schuster, and S. R. Wilson, "Spectroscopy of Matrices and Thin Films with an Integrating Sphere," *Appl. Spectrosc.*, vol. 43, no. 2, p. 320, 1989.

[145] M. Lassen, D. Balslev-Clausen, A. Brusch, and J. C. Petersen, "A versatile integrating sphere based photoacoustic sensor for trace gas monitoring," *Opt. Express*, vol. 22, no. 10, p. 11660, 2014.

[146] J. T. O. Kirk, "Modeling the performance of an integrating-cavity absorption meter: theory and calculations for a spherical cavity," *Appl. Opt.*, vol. 34, no. 21, p. 4397, 1995.

[147] R. A. Leathers, T. V. Downes, and C. O. Davis, "Analysis of a point-source integrating-cavity absorption meter," *Appl. Opt.*, vol. 39, no. 33, p. 6118, 2000.

[148] D. Masiyano, J. Hodgkinson, S. Schilt, and R. P. Tatam, "Self mixing interference effects in tunable diode laser spectroscopy," *Appl. Phys. B Lasers Opt.*, vol. 96, no. 4, p. 863, 2009.

[149] E. S. Fry, G. S. Kattawar, D. J. Gray, X. Zhao, and Z. Lu, "Apparatus and method for direct measurement of absorption and scattering coefficients in situ," US patent RE41682 E1, 2010.

[150] Hobi Labs Inc, “a-Sphere In-situ Spectrophotometer,” *Product datasheet*, 2006. [Online]. Available: http://www.hobilabs.com/cms/index.cfm/37/152/1253/1895/index.html. [Accessed: 01-Sep-2015].

[151] R. M. Abdullin and A. V Lebedev, “Use of an integrating sphere as a multiple pass optical cell,” *Sov. J. Opt. Technol.*, vol. 55, p. 139, 1988.

[152] E. S. Fry, G. W. Kattawar, B. D. Strycker, and P.-W. Zhai, “Equivalent path lengths in an integrating cavity: Comment,” *Appl. Opt.*, vol. 49, no. 4, p. 575, 2010.

[153] T. Jávorfi, J. Erostyák, J. Gál, A. Buzády, L. Menczel, G. Garab, and K. Razi Naqvi, “Quantitative spectrophotometry using integrating cavities,” *J. Photochem. Photobiol. B.*, vol. 82, no. 2, p. 127, 2006.

[154] J. Hodgkinson, D. Masiyano, and R. P. Tatam, “Using integrating spheres as absorption cells: path-length distribution and application of Beer’s law,” *Appl. Opt.*, vol. 48, no. 30, p. 5748, 2009.

[155] J. Hodgkinson, D. Masiyano, and R. P. Tatam, “Using integrating spheres with wavelength modulation spectroscopy: effect of pathlength distribution on 2nd harmonic signals,” *Appl. Phys. B Lasers Opt.*, vol. 110, no. 2, p. 223, 2012.

[156] J. Yu, Y. G. Zhang, Q. Gao, G. Hu, Z. G. Zhang, and S. H. Wu, “Diffuse reflectivity measurement using cubic cavity,” *Opt. Lett.*, vol. 39, no. 7, pp. 1941–1944, 2014.

[157] J. Yu, F. Zheng, Q. Gao, Y. Li, Y. Zhang, Z. Zhang, and S. Wu, “Effective optical path length investigation for cubic diffuse cavity as gas absorption cell,” *Appl. Phys. B Lasers Opt.*, vol. 116, p. 135, 2013.

[158] J. Yu, Q. Gao, Y. G. Zhang, Z. G. Zhang, and S. H. Wu, “Effective optical path length for tandem diffuse cubic cavities as gas absorption cell,” *J. Opt.*, vol. 16, no. 12, p. 125708, 2014.

[159] L. M. Manojlović and A. S. Marinić, “On the integrating cavity transfer function and decay time,” *Meas. Sci. Technol.*, vol. 22, no. 7, p. 75303, 2011.

[160] E. Hawe and E. Lewis, “An Investigation into the feasibility of adapting an integrating sphere for use as a gas absorption cell.,” in *IOP Proc. Photon*, 2006, vol. 16.

[161] E. Hawe, P. Chambers, C. Fitzpatrick, and E. Lewis, “CO2 monitoring and detection using an integrating sphere as a multipass absorption cell,” *Meas. Sci. Technol.*, vol. 18, no. 10, p. 3187, 2007.

[162] P. Chambers, W. B. Lyons, T. Sun, and K. T. V Grattan, “Analysis of the optical power loss arising from a fibre coupled integrating sphere used as a compact gas sensor,” *Sensors Actuators, A Phys.*, vol. 162, no. 1, p. 20, 2010.

[163] E. S. Fry and G. W. Kattawar, “Measurement Of The Absorption Coefficient Of Ocean Water Using Isotropic Illumination,” in *Proc of SPIE Ocean Optics IX*, 1988, vol. 925, p. 142.

[164] J. Hodgkinson, D. Masiyano, and R. P. Tatam, “Gas cells for tunable diode laser absorption spectroscopy employing optical diffusers. Part 1: Single and dual pass cells,” *Appl. Phys. B Lasers Opt.*, vol. 100, no. 2, pp. 291–302, 2010.

[165] J. N. Bixler, C. A. Winkler, J. D. Mason, and V. V Yakovlev, “Low cost integrating cavity for monitoring of environmental toxins,” in *SPIE 9314, Optics and Biophotonics in Low-Resource Settings*, 2015, vol. 9314, p. 93140T.

[166] J. Yu, Q. Gao, and Z. Zhang, “ High reflected cubic cavity as long path absorption cell for infrared gas sensing ,” 2014, vol. 9220, p. 92200I–92200I–12.

[167] Instrument Systems Konica Minolta Group, “ISP Series - Integrating Spheres,” Instrument Systems GmbH, Product brochure, 2014.

[168] D. R. Dana and R. A. Maffione, “A new hyperspectral spherical-cavity absorption meter,” in *Proc. Ocean Sciences Meeting*, 2006.

[169] USEPA, “Analytical Methods Approved for Compliance Monitoring under the Long Term 2 Enhanced Surface Water Treatment Rule,” 2008.

[170] F. D. Wilde and D. B. Radtke, “Section A6. National Field Manual for the Collection of Water-Quality Data,” in *Handbooks for Water-Resources*

Investigations, no. 2, U.S. Geological Survey, Ed. U.S. Geological Survey, 2005.

[171] K. L. King, "Turbidimeter signal processing circuit using alternating light sources," US patent 5140168, 1992.

[172] Hydrolab, "4-Beam Turbidity," *Technical white paper*, 2014. [Online]. Available: http://www.esonetyellowpages.com/datasheets/4beam_1254491289.pdf. [Accessed: 01-Jun-2016].

[173] M. Johnson, "Contamination and Industrial Systems," in *Photodetection and Measurement: maximizing performance in optical systems*, vol. 1st, New York: McGraw-Hill, 2003, p. 183.

[174] Y. Lin, "Using FPGAs to solve challenges in industrial applications," *EE times*, 2011. [Online]. Available: http://www.eetimes.com/document.asp?doc_id=1279239. [Accessed: 20-Nov-2015].

[175] T. Kissinger, T. O. H. Charrett, and R. P. Tatam, "Range-resolved interferometric signal processing using sinusoidal optical frequency modulation," *Opt. Express*, vol. 23, no. 7, p. 9415, 2015.

[176] T. Kissinger, T. O. H. Charrett, and R. P. Tatam, "Fibre segment interferometry using code-division multiplexed optical signal processing for strain sensing applications," *Meas. Sci. Technol.*, vol. 24, no. 9, p. 94011, 2013.

[177] G. C. Bjorklund, "Frequency-modulation spectroscopy: a new method for measuring weak absorptions and dispersions," *Opt. Lett.*, vol. 5, no. 1, p. 15, 1980.

[178] T. Iseki, H. Tai, and K. Kimura, "A portable remote methane sensor using a tunable diode laser," *Meas. Sci. Technol.*, vol. 11, no. 6, p. 594, 2000.

[179] K. Uehara and H. Tai, "Remote detection of methane with a 1.66-μm diode laser," *Appl. Opt.*, vol. 31, no. 6, pp. 809–814, 1992.

[180] D. V Sarwate and M. B. Pursley, "Crosscorrelation properties of pseudorandom

and related sequences," *Proceedings of the IEEE*, vol. 68, no. 5. pp. 593–619, 1980.

[181] D. D. Rife and J. Vanderkooy, "Transfer-Function Measurement with Maximum-Length Sequences," *J. Audio Eng. Soc*, vol. 37, no. 6, pp. 419–444, 1989.

[182] T. Kissinger, "Range-resolved optical interferometric signal processing," Cranfield University, 2015.